UNIVERSITY
OF TRENTO - Italy
DEPARTMENT OF INDUSTRIAL ENGINEERING

XXVIII cycle

Doctoral School in Materials Science and Engineering

Mechanism of anisotropic shrinkage during sintering of metallic powders

Elisa Torresani

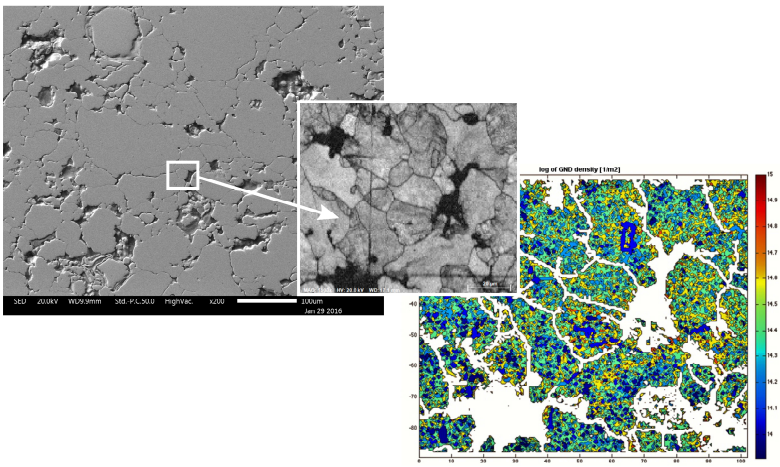

April 2016

MECHANISM OF ANISOTROPIC SHRINKAGE DURING SINTERING OF METALLIC POWDERS

Elisa Torresani
E-mail: elisa.torresani@unitn.it

Approved by:

Prof. Alberto Molinari, Advisor
Department of Industrial Engineering
University of Trento, Italy.

Ph.D. Commission:

Prof. Vigilio Fontanari,
Department of Industrial Engineering
University of Trento, Italy.

Prof. Eugene A. Olevsky,
Department of Mechanical Engineering
San Diego State Univerity, Usa.

Prof. Gino Mariotto,
Department of Computer Science
University of Verona, Italy.

University of Trento,
Department of Industrial Engineering

April 2016

University of Trento - Department of Industrial Engineering

Doctoral Thesis

Elisa Torresani - 2016
Published in Trento (Italy) – by University of Trento

ISBN: - - - - - - - - -

To my Family

Abstract

The anisotropic dimensional change on sintering of a prior cold compacted iron was investigated by dilatometry. Shrinkage is larger along the compaction direction than in the compaction plane. This phenomenon is very pronounced during the heating ramp in alpha phase and in particular below the Curie temperature, while in austenitic field is quite poor. The results of dilatometry tests were elaborated according to the shrinkage kinetics model of classical sintering theory, to calculate an effective diffusion coefficient along the two directions, which resulted higher for direction parallel to the compaction direction than perpendicular to it. In both directions, the effective diffusion coefficient is larger than that reported in the literature for pure iron, corresponding to an equilibrium density of structural defects. It also varies during the isothermal holding time. This discrepancy is attributed to the defectiveness introduced by cold compaction, that increases diffusivity through the activation of dislocation pipe mechanism, which is particularly intense below the Curie. This interpretation may also justify anisotropy of shrinkage due to the inhomogeneous deformation of interparticle contact regions that was measured with ISE method and EBSD analysis.

The anisotropic shrinkage was also described through a modified micromechanical model proposed by the continuum mechanics approach, where the porous body is composed by aligned, elongated particles and elliptic pores, whose geometrical parameters were obtained through image analysis of SEM microhgraphs. The dislocation density calculated for different sintering temperatures was comparable to that measured experimentally.

The effect of green density on anisotropy of shrinkage was investigated, too. Anisotropy tends to increase with green density, because of the larger plastic deformation introduced in the interparticle regions by the compaction pressure.

Contents:

Chapter I

Introduction

Powder metallurgy (PM) is recognized from decades as one of the principal manufacturing processes for producing several industrial products. The capability of this net shape technology to obtain components with a high dimensional and geometrical precision has promoted its large diffusion in the manufacturing of structural components for many industrial sectors.

The PM process, avoiding most the machining operations, is highly competitive compared to other production technologies, as casting, machining or stamping.

In the conventional PM process the powders are uniaxially compacted in rigid dies obtaining the so called green compacts, which are sintered to promote the formation of metallic bonding between the particles. The geometrical feature and the dimensions of the green compacts obtained through the compaction differ from the final product only by the dimensional changes that occur during sintering. Therefore, the critical aspect of this technology is the proper management of the different production steps in order to obtain most of dimensional and geometrical features required in the various applications without the use post-sintering machining. Sometimes post-sintering machining are necessary to obtain some geometrical details and any strict tolerances required by specific applications; in these cases the competitiveness of this technology is not compromised provided that machining is limited to details and tolerances that cannot be obtained directly during compaction and sintering.

Dimensional change during sintering, either shrinkage or swelling, must be predicted to properly design the cold compaction tooling and strategy. Dimensional change of uniaxially cold compacted parts is anisotropic. Nowadays, designers do not have a rational designing tool accounting for such an anisotropy; design of the process is still based on experience and empirical methodologies, often based on the trial-and-error approach.

The international literature is focused on studying the anisotropy of the dimensional changes of the uniaxially cold compacted components which is a very complex aspect. The main causes of anisotropy are still uncertain. The principal approach used for developing a model of anisotropy of dimensional changes during sintering is based on the continuum mechanics, and considers the geometry of pores and particles obtained by compaction as its principal cause.

Since a few years the Metallurgy Group of the University of Trento has started a research program focused on this field with the aim of studying the dimensional change on sintering and its anisotropy form a Physical metallurgy point of view, starting from the analysis of the shrinkage kinetics as affected by cold compaction and sintering.

The present PhD work is part of this research program as a first step in the understanding of the principal mechanisms that cause the anisotropic dimensional change in metal powder sintering.

The peculiar characteristic of PM is represented by the microstructure resulting from the compaction step, that affect the transformations responsible for the formation of the sintering neck, and significantly influence the dimensional variations.

Therefore this work is principally focused on investigating the influence of the structure and geometry of the powder particles deformed by cold compaction on the sintering shrinkage kinetics and on its anisotropy.

The work is mainly based on the use of dilatometry to investigate sintering shrinkage of specimens cut from the green parts along the compaction direction and in the compaction plane. The shrinkage kinetic equations from the classical theory of sintering was used, introducing an effective diffusion coefficient accounting for the effect of the structural defects introduced by cold compaction in the interparticle regions on the mass transport mechanism responsible for the sintering and shrinkage. Accordingly, experimental procedures to measure the dislocations density in the different directions of samples were utilized, while the geometrical parameters of real compacted particles were deeply investigated with a measurement procedure based on Image Analysis of the microstructure, defined and implemented during this work. These structural and geometrical parameters are implemented in the existing model based on the continuum mechanics, to propose an original matching between the two approaches to study the subject.

Chapter II

State of the art

Powder Metallurgy (PM) is a technology well suitable to components with excellent proprieties and dimensional and geometrical precision starting from a mixture composed by metallic powders. The main PM process is based on two main steps: uniaxial cold compaction of the powder mix and sintering.

During compaction, a powder mixture with the desired composition and a lubricant is inserted into a rigid die in order to obtain, through the application of an uniaxial pressure, the green compact. It has the geometry (a part from some geometrical details that cannot be obtained) and the dimensions (a part from the dimensional change occurring on sintering) of the final component but very poor mechanical proprieties because its consistency derives only from the packing and the deformation of powders. Sintering is a heat treatment where thermal activated processes promote the formation of the metallic bonding between the powder particles. After this step the components possess mechanical proprieties depending on the residual porosity, but sometimes comparable to those attainable with the classical methods of production as forging and turning. During sintering not only the physical, mechanical and chemical properties but also the dimensions of the component are obtained. The dimensional change during sintering of uniaxially cold compacted green parts is anisotropic, being different between the directions parallel and perpendicular to the compaction one. Sintering mechanisms and kinetics, and their effect on dimensional changes are widely investigated in literature. Two main approaches have been developed. The former approach that was developed and that we can consider as the “classical theory of sintering” describes sintering through an investigation of phenomena occurring in the interparticle contact region. It focuses on the consequences of the thermally activated bonding mechanisms that promote the formation and the growth of the necks, i.e. the contacts between the particles. The latter approach was developed most recently; it is based on the continuum mechanics and observes sintering from a rheological point of view. The behaviour of the porous body is described using the nonlinear-viscous correlation. Thanks to the widespread availability of simulations software and to the increasing computing capability, with such an approach they were developed models with the purpose of predict the final dimension of the sintered components and the possible presence of distortions.

2.1 Classical theory of sintering

The classical theory of sintering groups all of the works that study the mass transport mechanisms that promote the formation and the growth of the neck, using a local point of view. The driving force of sintering [1–8] was identified in the reduction of the total interfacial energy (Δ(γA)) that can be expressed with the following Equation (2.1):

$$\Delta(\gamma A) = \Delta\gamma \cdot A + \gamma \cdot \Delta A \qquad (2.1)$$

Where γ and A are the interfacial energy and the total surface area. A scheme of the basic phenomena occurring on sintering related to the driving force is reported in Figure (2.1). Densification causes an interfacial energy change (Δγ), coarsening causes a change in the total surface area (ΔA).

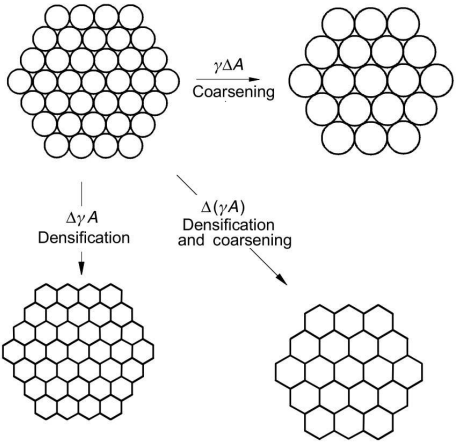

Figure 2.1. Basic phenomena occurring on sintering due to the driving force (adapted from "*Sintering: densification, grain growth & microstructure*" Suk-Joong L. Kang, Elsevier 2005).

In the case of the solid state sintering Δγ derives from the replacement of solid/vapour surface with solid/solid interface.

The kinetic relationships that describe sintering in terms of shrinkage and densifications were derived using a two-sphere model (Figure(2.2(a))) [9].

It assumes that at the beginning of sintering particles are in a point contact, thus neglecting prior cold compaction.

The difference in the surface curvature at the contact area between the two spherical particles allows representing the driving
force as difference in stress, vacancy concentration and vapour pressure that induce the flow of the material. These are expressed by the Equations (2.2), (2.3) and (2.4) considering the geometry in Figure (2.2(a)):

$$\Delta\sigma = \gamma_S\left(\frac{2}{a}+\frac{1}{r}-\frac{1}{x}\right)\cong\frac{\gamma_S}{r} \qquad (a >> x >> r) \tag{2.2}$$

$$\Delta C_V = C_{V\infty}\frac{\Omega_V}{RT}\frac{\gamma_S}{r} \tag{2.3}$$

$$\Delta p = p_\infty\frac{\Omega}{RT}\frac{\gamma_S}{r} \tag{2.4}$$

Where σ is the stress due a curved surface, γ_s is the surface tension, ΔC_V is the vacancy concentration difference, $C_{V\infty}$ is the vacancy concentration at the equilibrium, Ω_v is the molar volume of the vacancies, R is the universal constant of gas, T the absolute temperature, Δp is the difference in vapour pressure and Ω is the molar volume of the material.

The material transport can occur due to different mechanisms and paths (Figure (2b)) that can be divided into two groups: the bulk transport and the surface transport. The bulk transport contributes to the densification (Δγ), while the surface transport contributes only to the neck formation without changing the distance between the particles (ΔA).

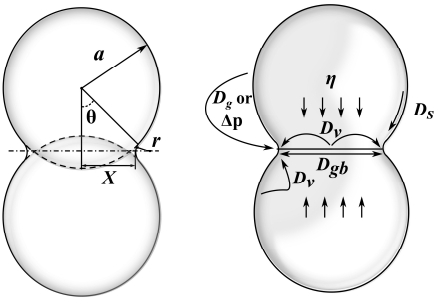

Figure 2.2. a) two sphere model; b) material transport during sintering, where D_g, D_v, D_s, D_{gb}, are respectively gas, volume, surface and grain boundary diffusivity and η is the viscosity.

Starting from the 1950s after the model proposed in the Alexander-Baluffi work's [10] most of the studies on the pressure-less sintering recognize in the grain boundary diffusion the principal diffusion mechanism involved in the densification and shrinkage [11,12]. The dominance of the grain boundary diffusion is due to its value of diffusion coefficient that is higher than the bulk one.

Others authors in the 1980s recognized the influence of the lattice defects like dislocations on diffusion and introduced the concept of dislocation-activated sintering. Shatt and Friedrich [13–15], observing the sintering of a sphere-plate model made from copper, demonstrated experimentally how at the contact area the dislocation density changes during the sintering. They explained the initial increase in the dislocation density at the contact area and the formation of the dislocation rosette as the effect of the capillary force presents between the particles. They described the self-activation of the process as the result of the increase in the dislocation density in the neck area that creates an entire layer of dislocations surrounding the particles. In these studies the dislocation controlled diffusional flow was considered as the sintering mechanism, enhanced by the presence of the dislocations and cause the relative movement of the powder particles under the influence of the capillary forces.

In all these works a fundamental aspect for a cold compacted component was not considered: the material has already a high dislocation density due to the plastic deformation of the powder particles during the compaction stage. Moreover another mass transport mechanism that is affected by the presence structural defects and it is enhanced by high values of dislocations density should be considered: the volume diffusion mechanism of dislocation pipe diffusion.

The mass flow can occur through different mechanisms that are distinguished on the base of the material source and sink and on the controlling parameter, as shown in Table (2.1).

Material transport mechanism	Material source	Material target	Diffusion coefficient
Lattice diffusion:			
a) from grain boundary	**Grain boundary**	Neck	Volume diffusivity: D_v
b) from grain surface	**Grain surface**	Neck	
Grain boundary diffusion	**Grain boundary**	Neck	Grain boundary diffusivity: D_{gb}
Viscous flow	**Lattice grain**	Neck	Viscosity η
Surface diffusion	**Grain surface**	Neck	Surface diffusivity: D_s
Gas phase transport			
a) Evaporation/condensation	**Grain surface**	Neck	Vapour pressure difference: Δp
b) Gas diffusion	**Grain surface**	Neck	Gas diffusivity: D_g

Table 2.1. mechanisms of material transport during sintering.

The motion of atoms can be observed from two points of view, in the first the atoms are moving as the result of a diffusion of vacancies due a difference in their concentration, in the second the atoms are moving due to a stress gradient. The bulk mechanisms are responsible for the densification of the components and consequently for the shrinkage due to the movement of the material from inside of the particles to the growing neck. Different mathematical relationships are present in the classical theory of sintering that describe the neck growth kinetic as a function of the different mass transport mechanisms [16]. These relations express the neck size ratio X/D as a function of isothermal sintering time:

$$\left(\frac{X}{D}\right)^n = \frac{Bt}{D^m} \tag{2.5}$$

Where X is the neck diameter, D is the particle diameter, t is the isothermal sintering time, n and m are exponents and B contains material and geometrical constants and parameters; n, m and B depend on the mechanisms, as shown in Table (2.2).

Mechanism	*n*	*m*	B
Viscous Flow	2	1	$3\gamma_s/\eta$
Plastic Flow	2	1	$9\pi\gamma b D_v/kT$
Evaporation-Condensation	3	2	$(3P\gamma_s/\rho^2)(\pi/2)^{1/2}(M/kT)^{3/2}$
Volume Diffusion	5	3	$80D_v\gamma_s\Omega/kT$
Grain Boundary Diffusion	6	4	$20\delta D_b\gamma_s\Omega/kT$
Surface Diffusion	7	4	$56D_s\gamma_s\Omega^{4/3}/kT$

Table 2.2. Parameters for the Equation (2.5).

Where:

γ_s = surface energy
η = viscosity
b = Burgers vector
k = Boltzmann's constant
T = absolute temperature
ρ = theoretical density
δ = grain boundary width
D_s = volume diffusivity
D_v = surface diffusivity
D_b = grain boundary diffusivity
M = molecular weight
Ω = atomic volume

The parameters n, m and B are time dependent but usually they were considered constant. This relationship is based on the two-sphere model where the effects due to the compaction are not considered. The initial contact between the particle in this model is represented by a point (X=0) and the diffusion mechanisms are independent from the presence of the defects in the material, in fact the diffusion coefficient is referring to an equilibrium density of structural defects, as that of an annealed material.

There is another mass transport mechanism introduced previously: the dislocation pipe diffusion that is influenced directly by the presence of the structural defects in the material and can explain the phenomenon of the self activation of sintering that was proposed by Freidrich and Shatt in their works [13–15]. It is explained in the next paragraph.

3.1.1.1 *Dislocation pipe diffusion*

The dislocation pipe diffusion is a particular volume diffusion mechanism in which the atoms are moving near the dislocations where the diffusivity is higher than through the lattice. Usually at lower dislocation densities especially for diffusion at high temperature the contribution of this mechanism is negligible. Its importance becomes greater with the deformation of the material and the consequent increase in dislocation density and, due to its lower activation energy, is dominant over volume and grain boundary diffusion at lower temperatures. In literature different models were created to describe the dislocation pipe diffusion, the simplest is that developed by Smoluchowski [17] that shows similarities with the Fisher model of the grain boundary diffusion (Figure(2.3)).

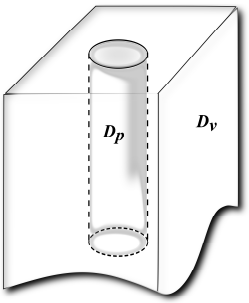

Figure 2.3. Smoluchowsky representation of dislocation pipe diffusion.

In this model the dislocations are assumed occupying a cylindrical pipe with a diffusivity D_p larger than in the lattice D_v.

The diffusion coefficients increase with temperature, with discontinuities in correspondence of structural and physical transformations. Especially for the ferromagnetic materials and near the Curie temperature (T_c) a quick variation in the pipe diffusion coefficient is present. This phenomenon is clearly shown in the studies conducted by Shima on high-purity iron [18] (Figure (2.4)).

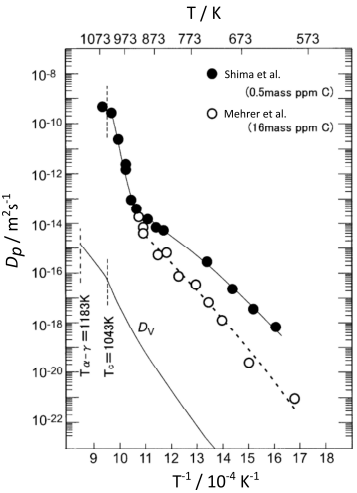

Figure 2.4. Comparison of diffusivity of lattice and dislocation pipe diffusion in α-iron at equilibrium. (adapted from [18]).

In the graph of Figure (2.4) it can be noticed how on increasing temperature the coefficient increases for both the volume and the pipe diffusion, but on approaching the Curie temperature, when iron assumes a paramagnetic behaviour, the increase in enhanced for Dp. This phenomenon seems to be "… caused by the disappearance of the magnetic moment of Fe atoms located at the dislocation core near the T_c. The magnetic moment is sensitive to the atomic distance. Then, the influence of a magnetic transformation on diffusion along dislocations and grain boundaries is larger than that on diffusion through the crystal lattice" [19].
The values shown in Figure (2.4) are referring to equilibrium conditions that means for a low dislocation density and, how it was mentioned above, a strong correlation exists between the dislocation pipe diffusion and the density of structural defects. On the base of the lattice diffusion length and the average distance between the dislocations (Λ), that depend on their density, using the classification proposed by Harrison [20] three kinetic regimes can be distinguished. The average distance can be express by the Equation (2.6):

$$\Lambda = \frac{K}{\sqrt{\rho_d}} \tag{2.6}$$

Where K is a parameter that depends on how the dislocations are disposed in the volume (array of parallel dislocation K=1, hexagonal array K = $\sqrt{3}/2$); related to this, the type A kinetic occurs for:

$$D\sqrt{Dt} > \Lambda \tag{2.7}$$

It means that the diffusion fields is composed by heavily overlapped dislocations.
The type B is observed for:

$$r_p << \sqrt{Dt} << \Lambda \tag{2.8}$$

In this case the overlap of the dislocations in the diffusion fields can be considered negligible, where r_p is the dislocation pipe radius.
The last kinetic type (C) prevails for:

$$r_p > \sqrt{Dt} \tag{2.9}$$

when the diffusion can be limited at the dislocation core.
The density of the structural defects in the dislocation pipe influences not only the type of the kinetic but it is also related to the diffusivity itself with the introduction of the effective diffusion coefficient D_{eff}.
This diffusivity results linearly proportional to the dislocation density and can be expresses by the following Equation (2.10) [21]:

$$D_{eff} = D_v\left(1 + g\frac{D_p}{D_v}\right) \qquad g = \pi r_p^2 \rho_d \tag{2.10}$$

where D_v and D_p are respectively the volume and pipe diffusion coefficient at equilibrium that is for an annealed material (Figure (2.4)), r_p is the radius of the pipe, ρ_d is the dislocations density.

2.2 Continuum mechanics approach for sintering modelling

The mathematical apparatus of continuum mechanics represents the base of this approach that analyzes sintering using a continuum description of the problem. Sintering and especially the flow of the material are studied as a rheological problem and for this purpose the mechanics of the continuum is used. The mechanics of the continuum is based on the theories of plastic deformation of porous bodies [22–24] and the nonlinear-viscous (creep) deformation of porous bodies [25–27]. In literature the first work that uses the rheological point of view to describe the sintering was carried out by Frenkel [28] that considered the coalescence of two viscous particles driven by surface tension, but this model not still represents a continuum mechanics approach:

$$-\frac{\partial \gamma_S}{\partial t} = 2\eta\dot{\varepsilon}V \tag{2.11}$$

Where t is the time, γ_S is the surface tension, η is the viscosity, $\dot{\varepsilon}$ is the shrinkage rate and V is the volume.
The ideas proposed with this model were developed by other authors that described the densifications of a porous material containing isolated spherical pores [29].
A phenomenological model of sintering based on the concept of thermodynamics of irreversible processes can be found in Olevsky work [30]. The constitutive relationship of this model is defined by Equation (2.12):

$$\sigma_{ij} = \frac{\sigma(W)}{W}\left[\dot{e}_{ij} + \left(\psi - \frac{1}{3}\right)\dot{e}\delta_{ij}\right] + P_L\delta_{ij} \tag{2.12}$$

Where:

- ✓ σ_{ij} are the external stresses tensor components;
- ✓ $\sigma(W)/W$ represents the generalized viscosity, a constitutive characteristic of the fully dense material;
- ✓ $\sigma(W)$ is the effective stress;
- ✓ W is the equivalent effective strain rate;
- ✓ $\dot{e}_{ij}$ are the strain rate tensor components,

- ✓ ψ is the bulk modulus and represents the resistance of the volume change;
- ✓ φ is the shear modus that corresponds to the resistance of shape changes,
- ✓ $\dot{e}$ is the volume strain rate.
- ✓ $P_L\delta_{ij}$ represents the sintering contribution (due to the thermodynamics driving force), where P_L is the Laplace pressure or effective sintering stress and δ_{ij} is the Kronecker delta.

The effective stress and strain rate, together with bulk and shear moduli and sintering stress, are dependent on porosity (θ), a dimensionless parameter indicating the volume fraction of pores present in the study domain:

$$\theta = \frac{V_{pores}}{V_{total}} \tag{2.13}$$

$$W = \sqrt{\frac{\dot{\gamma} + \psi\dot{e}}{1-\theta}} \tag{2.14}$$

$$\psi = \frac{2}{3}\frac{(1-3)^3}{\theta} \tag{2.15}$$

$$\varphi = (1-\theta)^2 \tag{2.16}$$

$$P_L = \frac{3}{2}\frac{\gamma_s}{a}(1-\theta)^2 \tag{2.17}$$

Where γ_s is the surface tension and a the particles radius.
Pores are considered homogeneously distributed, such that the overall porous material can be considered isotropic. The sintering constitutive equation needs to be accompanied by the densification equation (conservation of mass), expressed as follows:

$$\dot{\varepsilon} = \frac{\dot{\theta}}{(1-\theta)} \tag{2.18}$$

Where the $\dot{\varepsilon}$ is the trace of the strain rate tensor.

Observing the Equation (2.12) it is clear how this approach describes the behaviour of the material during sintering using a model that considers the material parameters as viscosity, shear stress modulus and porosity. The sintering driving force is represented by a sintering stress (Laplace pressure) that corresponds to the overall effect of local capillary stresses in the component. The strong correlation between many parameters of the model and the porosity shows how the microstructural characteristics assume a fundamental role in the construction of the equation of the sintering kinetic, which permits to describe the macroscopic evolution starting from the microscopic structure. The description and evolution of different microstructure characteristics as the geometry of porosity and of grains considered in some models based on the continuum mechanics [30], assumes an important role to understand the origins of the anisotropic dimensional changes during the sintering. Different methods as analytical models in two dimension [31–34], three dimensions [35,36], Monte Carlo simulation [37], and discrete element method [38] has been used in order to study the effect of the microstructure on the anisotropic shrinkage. In these studies the most important microstructural feature that cause anisotropic shrinkage was identify as the pores and grains morphology.

For that concerns the pore geometry, in most of these model it was described using an elliptical shape that has an influence on the sintering stress; it cannot be considered constant along the different directions, but results inversely proportional to the pore surface curvature. A similar elongated geometry is used to describe the powder particles and grains in order to consider the different extension of the contacts that represents the source of the material involved in the sintering flow. With this approach, differently from the classical theory, factors that have a considerable influence at macro-scale can be analyzed: the in-homogeneities of different characteristics (density or others physical-mechanics proprieties), the application of external forces and the interaction of the sinter body with the "external environmental" (friction with the sole of the furnace). Considering the influence of all these factors during sintering mean solve the corresponding boundary problems that results impossible using only a local approach. Based on these considerations continuum mechanics offers the possibility to describe the behaviour of the sinter body as the results not only by the interaction of the powder particles but also by macroscopic factors.

2.3 Anisotropy of dimensional change during sintering

Almost all the studies in literature founded the origin of the anisotropic dimensional change of sintering on the effect that the prior compaction has on the porous body, especially on the initial distribution of the density, the rearrangement of the particles, their geometry, the orientation and size distribution of the porosity.

The studies based on the continuum mechanics focused mostly on the geometry of the pore that is described through an elliptical shape with the major axis perpendicular to the direction of the compaction [39–43]. Regarding the powder particles, in some works their geometry is described with elongated shapes as ellipses and parallelepipeds [33,34,44]. Considering these geometrical aspects, the anisotropic behaviour is imputed, for that concerns the effects of porosity, to an anisotropic driving force: the sintering stress changes along the different directions due a different curvature of the neck. The geometry of the particles influences the kinetic of sintering due the different extension of the contact area between the particles, to which corresponds a different material flow to the growing neck. The initial extension of the contacts which is not punctual and depends on the direction; such features are a boundary condition that the classical theory of sintering based on the two-sphere model did not take into account. Other external factors were considered responsible for the anisotropic dimensional changes during sintering, as the effect of creep due to gravity [45] especially in the case of liquid phase sintering [46] and the friction between the surface of the component and the sole of the furnace; they were modelled using the continuum mechanics and calculated through finite elements.

For the studies based on the classical approach, the first work that describes and investigates the causes of the anisotropic dimensional changes can be found in the work conducted during my master thesis [47]. We analyzed the influence of the deformation due to cold compaction that produces an anisotropy of diffusion and, in turn, of the dimensional changes. In order to obtain a mathematical and physical correlation that can model this phenomenon we used the Equation (2.5) that represents an approximate correlation between the neck size ratio and the shrinkage (Equation (2.19)):

$$\frac{\Delta l}{l_0} = \left(\frac{X}{2D}\right) \rightarrow \left(\frac{\Delta l}{l_0}\right)^{n/2} = \frac{Bt}{2^n D^m} \tag{2.19}$$

where n, m and B are the parameter shown in Table (2.2).

As it is possible to notice the shrinkage depends on the diffusion mechanism and diffusivity. This equation derives from the classical theory of sintering where using the two sphere-model the effects due to the deformation of the powder are not taken into account. We found how the diffusion coefficient is influenced by the deformation of the material due to compaction, that promotes the activation of a particular volume diffusion mechanism (the dislocation pipe diffusion) which becomes more important and intense than the grain boundary diffusion. The dislocation pipe diffusion is time-depending due to its proportionality to the dislocation density that changes during sintering, due to the effects of different mechanisms as self-activation and recovery/recrystallization. Inserting the Equation (2.10) into the shrinkage kinetic for a volume diffusion mechanism the Equation (2.20) is obtained:

$$\left(\frac{\Delta l}{l_0}\right)^{5/2} = \frac{80\left[D_v\left(1+\pi r_p^2 \rho_d(t)\frac{D_p}{D_v}\right)\right]\gamma_s \Omega t}{2^5 D^3 kT} \qquad (2.20)$$

Where shrinkage is a function of time and its evolution is strictly liked to the dislocation density evolution in the material. Using this correlation was possible to obtain first the measurement of the effective diffusion coefficient during the isothermal holding as shown in Figure (2.5).

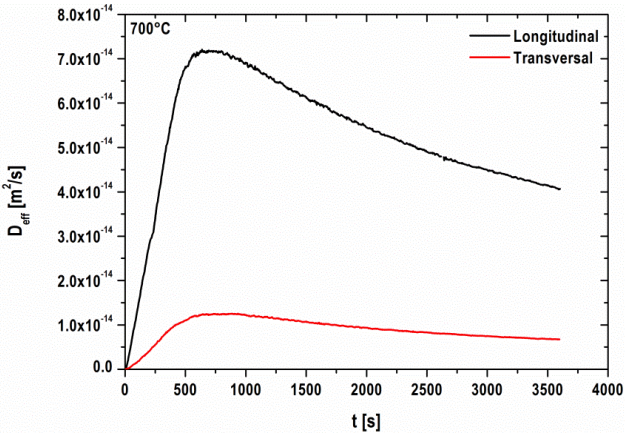

Figure 2.5 . Example of effective diffusion coefficient calculated using Equation (2.20) for the dislocation pipe diffusion mechanisms plotted versus the time of isothermal holding.

Considering the direct proportionality between the effective diffusion coefficient and the dislocation density its evolution in the isothermal holding can be measured through the Equation (2.10) and in order to obtain a validation of those results experimental methods were used: Indentation Size Effect (ISE) and EBSD analysis.

2.3.1 Indentation Size Effect (ISE)

With Indentation Size Effect is indicated the scale-dependent behaviour of indentation testing when the size of the hardness imprint is small, as in the cases of micro- and nano-indentation measurements. The classical continuum concepts of the plasticity considers the hardness H independent from the depth of the indentation (h), because it is defined as the load on the indenter (P) normalized on the projected contact area of the hardness imprint:

$$H = \frac{P}{A} \tag{2.21}$$

Where A is the projected contact area as shown in Figure (2.6).

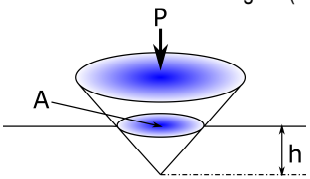

Figure 2.6. Schematic representation of conical indenters (Vikers and Berkovic tips) and the projected contact area.

The international literature [7–13] reports how the hardness significantly changes with the depth, especially when h is less than a few micrometers. The focus was pointed mostly on the crystalline metals where the plastic proprieties as yield stress, hardness, strain hardening coefficient and toughness are determined by the dislocations and their interactions. In the literature numerous mechanistic models of ISE can be found but the first that was proposed and the most used to explain the experimental data is the one developed by Nix and Gao [7]. This model introduces the concept of geometrically necessary dislocations ρ_G (GNDs) as the dislocations that are produced in the indentation area to accommodate the plastic deformation, as shown in the scheme of Figure (2.7).

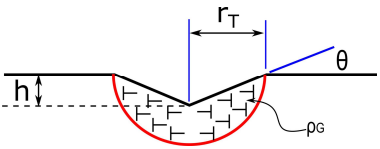

Figure 2.7. Schematic representation of the Nix and Gao model for conical indenters (Vikers and Berkovic tips).

These dislocations exist in addition to the statistically stored dislocations ρ_S (SSDs) produced during uniform straining, but their contribute become greater as the size of indentation decreases.
The mathematical relation that correlates the flow stress during the indentation (σ) and the total dislocation density ρ_T is based on the Taylor relation:

$$\sigma = \sqrt{3}\alpha_T G b \sqrt{\rho_T} \tag{2.22}$$

Where α_T is the Taylor factor, G is the shear modulus, and b the Burger's vector. The hardness can be determined combining the Equation (2.22) with the Tabor relation:

$$H = 3\sigma \tag{2.23}$$

In this model two hypothesis are made:

- ✓ The total dislocation density represents the simple sum of GNDs and SSDs contribute:

$$\rho_T = \rho_G + \rho_S \tag{2.24}$$

- ✓ The GNDs are concentrated in a hemispherical volume with a radius equal to the radius of contact area of the indenter with the surface (Figure(3.7)).

Starting from the second hypothesis and using simple geometrical correlations it is possible to determine the density of the geometrically necessary dislocations:

$$\rho_G = (3\tan^2\theta)/(2bh) \tag{2.25}$$

where θ is the angle between the surface of a rigid cone that represents the indenter and the undeformed material surface.

The Equation (2.25) represents the physical base of the ISE: the hardness increases at small depth due to the inverse proportionality between the GNDs density and the depth of the indentation (h).
Using both Equation (2.23) and (2.25) the relation that links hardness and indentation depth can be obtained:

$$H = H_0\sqrt{1+\frac{h^*}{h}} \tag{2.26}$$

where H_0 is the macroscopic hardness, the hardness at "large" depths that do not depend on the GNDs, but only from the SSDs:

$$H_0 = 3\sqrt{3}\alpha G b\sqrt{\rho_S} \tag{2.27}$$

The parameter h* is the characteristic depth that represents the limit below which the effect of the indentation size effect (due the GNDs) become appreciable:

$$h^* = \frac{3\tan^2\theta}{2b\rho_S} \tag{2.28}$$

The characteristic depth is not strictly a material constant because as can be noticed it depends both on the material parameters (b and ρ_S) and θ a geometrical parameter.
Subsequent works [14] modified the relation of total dislocations density (Equation(3.8)) introducing the Nye factor $\bar{r}$ to consider the crystallographic constraints on the GNDs and SSDs densities and the relations (2.24) and (2.28) can be rewritten as:

$$\rho_T = \bar{r}\rho_G + \rho_S \tag{2.29}$$

$$h^* = \frac{3\bar{r}\tan^2\theta}{2b\rho_S} \tag{2.30}$$

In the case of metals characterized by a FCC crystal structure $\bar{r}$ assumes approximately the value of 1.9 [15].

From the Equation (2.26) a linear correlation between the experimental data obtained with the micro- and nano-indentation (H^2 vs 1/h) can be obtain.

$$H^2 = H_0^2\left(1+\frac{h^*}{h}\right) \tag{2.31}$$

where the parameter h* is related to the slope of the Equation (2.31) and the intercept represent H_0^2. Considering the Equation (2.28) ρ_S corresponds to the dislocation density presents in the powder after compaction in the case of the green specimen or the density that is obtained through the mechanisms of the self activation and recovery/recrystallization for the sintering samples. The Indentation Size Effect can be used to estimate the SSDs density in the different areas of the powder particles through the Equation (2.32):

$$\rho_S = \frac{3}{2}\frac{\bar{r}\tan^2\theta}{bh^*} \tag{2.32}$$

2.4 The objective of the present work

This work follows the results obtained in previous studies conducted by the Metallurgy group of the University of Trento in order to investigate the dimensional changes in the metal powders compact during sintering [47–49].
The principal aim of the present work is the creation of a model that can describe the shrinkage along the different directions (parallel and perpendicular to the compaction direction) using the kinetic description of the diffusion mechanisms that are activated during sintering.
In order to reduce the number of factors that can influence the final dimension of the sintered parts as the production of liquid phase or the interaction between different components of the material we focused our research on the simplest case constituted by samples of iron powder.
The focus was pointed on the deformation due to the uniaxial cold compaction of the powder particles that compose the components as reported in Figure (2.5) and how this can influence the sintering behaviour of the material along the different directions.

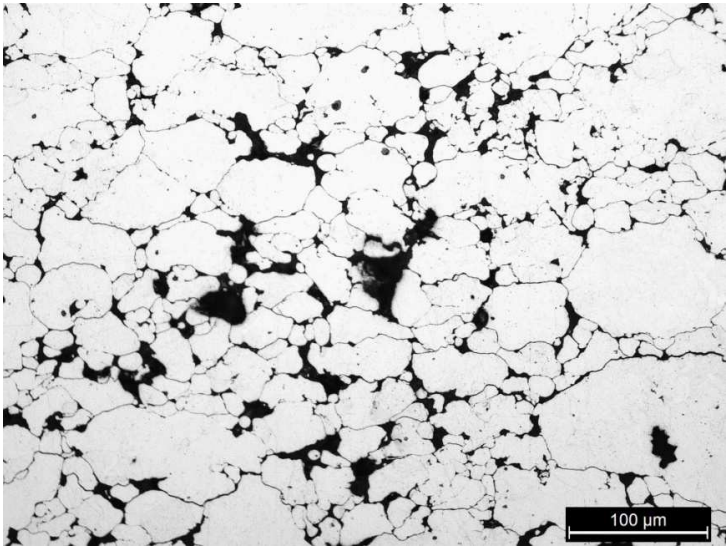

Figure 2.8. Deformed powder particles of a green component (magnification 200x).

The powder particles of Figure (2.8) are clearly compacted along the vertical axis of the picture that corresponds to the compaction direction, the corresponding deformation of the material results in a increase in dislocation density and contact area between the particles that is clearly not punctual as described by the two-sphere model of the classical theory of sintering. The anisotropy can be explained by a different grade of deformation of the powder particles along the principal directions (i.e. parallel and perpendicular to the compaction axis) that produces this geometry, the main characteristics of which can be resumed in a difference of the extension of the contact areas and of the density of the structural defects in the two directions. In the present work different typologies of analysis were used in order to measure and quantify the deformation of the material at the different stages of the sintering cycle and to correlate it to the sintering kinetic.

2.5 References

[1] R.L. Coble, Sintering Crystalline Solids. I. Intermediate and Final State Diffusion Models, J. Appl. Phys. 32 (1961) 787–792. doi:10.1063/1.1736107.

[2] M.F. Ashby, A first report on sintering diagrams, Acta Metall. 22 (1974) 275–289. doi:10.1016/0001-6160(74)90167-9.

[3] F.B. Swinkels, M.F. Ashby, A second report on sintering diagrams, Acta Metall. 29 (1981) 259–281. doi:10.1016/0001-6160(81)90154-1.

[4] K.S. Hwang, R.M. German, F.V. Lenel, Capillary forces between spheres during agglomeration and liquid phase sintering, Metall. Trans. A. 18 (1987) 11–17. doi:10.1007/BF02646216.

[5] H.E. Exner, E. Arzt, Sintering Processes, in: S. Sōmiya, Y. Moriyoshi (Eds.), Sinter. Key Pap., Springer Netherlands, 1990: pp. 157–184.

[6] F.V. Lenel, Powder metallurgy: principles and applications, Metal Powder Industry, 1980.

[7] F.V. Lenel, H.H. Hausner, I.A. El Shanshoury, J.G. Early, G.S. Ansel, The driving force for shrinkage in copper powder compacts during the early stages of sintering, Powder Metall. 5 (1962) 190–198. doi:10.1179/POM.1962.5.10.013.

[8] C. Herring, Surface Tension as a Motivation for Sintering, in: P.J.M. Ball, P.D. Kinderlehrer, P.P. Podio-Guidugli, P.M. Slemrod (Eds.), Fundam. Contrib. Contin. Theory Evol. Phase Interfaces Solids, Springer Berlin Heidelberg, 1999: pp. 33–69.

[9] G.C. Kuczynski, Self-diffusion in sintering of metallic particles, AIME TRANS. 185 (1949) 169–178.

[10] B.H. Alexander, R.W. Balluffi, The mechanism of sintering of copper, Acta Metall. 5 (1957) 666–677. doi:10.1016/0001-6160(57)90113-X.

[11] H. Ichinose, G.G. Kuczynski, Role of grain boundaries in sintering, Acta Metall. 10 (1962) 209–213. doi:10.1016/0001-6160(62)90118-9.

[12] H.E. Exner, P. Bross, Material transport rate and stress distribution during grain boundary diffusion driven by surface tension, Acta Metall. 27 (1979) 1007–1012.

[13] E. Friedrich, W. Schatt, Sintering of One-Component Model Systems: Nucleation and Movement of Dislocations in Necks, Powder Metall. 23 (1980) 193–197. doi:10.1179/pom.1980.23.4.193.

[14] E. Friedrich, W. Schatt, High Temperature Plasticity on Solid Phase Sintering, Sci Sinter. 15 (1983) 63–71.

[15] W. Schatt, E. Friedrich, Dislocation-Activated Sintering Processes, in: G.C. Kuczynski, D.P. Uskoković, H.P. III, M.M. Ristić (Eds.), Sintering'85, Springer US, 1987: pp. 133–141.
[16] R.M. German, Sintering theory and practice, Sinter. Theory Pract. Randall M Ger. Pp 568 ISBN 0-471-05786-X Wiley-VCH January 1996. 1 (1996).
[17] R. Smoluchowski, Theory of Grain Boundary Diffusion, Phys. Rev. 87 (1952) 482–487. doi:10.1103/PhysRev.87.482.
[18] Y. Shima, Y. Ishikawa, H. Nitta, Y. Yamazaki, K. Mimura, M. Isshiki, et al., Self-Diffusion along Dislocations in Ultra High Purity Iron, Mater. Trans. 43 (2002) 173–177. doi:10.2320/matertrans.43.173.
[19] Y. Iijima, Diffusion in high-purity iron: Influence of magnetic transformation on diffusion, J. Phase Equilibria Diffus. 26 (2005) 466–471. doi:10.1007/s11669-005-0036-1.
[20] L.G. Harrison, Influence of dislocations on diffusion kinetics in solids with particular reference to the alkali halides, Trans. Faraday Soc. 57 (1961) 1191–1199. doi:10.1039/TF9615701191.
[21] E.W. Hart, The Role cf Dislocations in Bulk Diffusion, Acta Metall. 5 (1957) 597–597. doi:10.1016/0001-6160(57)90127-X.
[22] C.L.D. H. A. Kuhn, Deformation Characteristics and Plasticity Theory of Sintered Powder Metals, Int J Powder Mat. 7 (1971).
[23] R.J. Green, A plasticity theory for porous solids, Int. J. Mech. Sci. 14 (1972) 215–224. doi:10.1016/0020-7403(72)90063-X.
[24] S. Shima, M. Oyane, Plasticity theory for porous metals, Int. J. Mech. Sci. 18 (1976) 285–291. doi:10.1016/0020-7403(76)90030-8.
[25] V.V. Skorokhod, M.B. Shtern, I.F. Martynova, Theory of nonlinearly viscous and plastic behavior of porous materials, Sov. Powder Metall. Met. Ceram. 26 (1987) 621–626. doi:10.1007/BF00810620.
[26] D.S. Wilkinson, M.F. Ashby, Pressure sintering by power law creep, Acta Metall. 23 (1975) 1277–1285. doi:10.1016/0001-6160(75)90136-4.
[27] J.M. Duva, A constitutive description of nonlinear materials containing voids, Mech. Mater. 5 (1986) 137–144. doi:10.1016/0167-6636(86)90029-3.
[28] J. Frenkel, Viscous flow of crystalline bodies under the action of surface tension., J Phys USSR. 9 (1945) 385–391.
[29] J.K. Mackenzie, R. Shuttleworth, A Phenomenological Theory of Sintering, Proc. Phys. Soc. Sect. B. 62 (1949) 833. doi:10.1088/0370-1301/62/12/310.
[30] E.A. Olevsky, Theory of sintering: from discrete to continuum, Mater. Sci. Eng. R Rep. 23 (1998) 41–100. doi:10.1016/S0927-796X(98)00009-6.

[31] W.R. Cannon, P.M. Raj, Evolution of Sintering Anisotropy Using a 2D Finite Difference Method, J. Am. Ceram. Soc. 92 (2009) 1391–1395. doi:10.1111/j.1551-2916.2009.03013.x.
[32] P.M. Raj, A. Odulena, W.R. Cannon, Anisotropic shrinkage during sintering of particle-oriented systems—numerical simulation and experimental studies, Acta Mater. 50 (2002) 2559–2570.
[33] E.A. Olevsky, B. Kushnarev, A. Maximenko, V. Tikare, M. Braginsky, Modelling of anisotropic sintering in crystalline ceramics, Philos. Mag. 85 (2005) 2123–2146. doi:10.1080/14786430412331331989.
[34] A. Zavaliangos, J.M. Missiaen, D. Bouvard, Anisotropy in shrinkage during sintering, Sci. Sinter. 38 (2006) 13–25.
[35] F. Wakai, T. Akatsu, Anisotropic viscosities and shrinkage rates in sintering of particles arranged in a simple orthorhombic structure, Acta Mater. 58 (2010) 1921–1929.
[36] F. Li, J. Pan, O. Guillon, A. Cocks, Predicting sintering deformation of ceramic film constrained by rigid substrate using anisotropic constitutive law, Acta Mater. 58 (2010) 5980–5988.
[37] V. Tikare, M. Braginsky, E. Olevsky, D.L. Johnson, Numerical Simulation of Anisotropic Shrinkage in a 2D Compact of Elongated Particles, J. Am. Ceram. Soc. 88 (2005) 59–65. doi:10.1111/j.1551-2916.2004.00042.x.
[38] A. Wonisch, O. Guillon, T. Kraft, M. Moseler, H. Riedel, J. Rödel, Stress-induced anisotropy of sintering alumina: Discrete element modelling and experiments, Acta Mater. 55 (2007) 5187–5199.
[39] H.H. Hausner, O.V. Roman, Linear shrinkage of metal powder compacts during sintering, Sov. Powder Metall. Met. Ceram. 3 (1965) 180–184. doi:10.1007/BF00773945.
[40] G.C. Kuczynski, G. Arghir, Short note: anisotropic shrinkage of copper compacts, Powder Met. Int. 10 (1978) 73.
[41] M. Mitkov, H.E. Exner, G. Petzow, Orientation of pore structure in loose and presses carbonyl iron and its influence on shrinkage anisotropy, Sinter. - New Dev. (1979) 90–98.
[42] H.E. Exner, An Introduction To The Development And Effects Of Voids In Sintered Materials, J. Microsc. 116 (1979) 25–37. doi:10.1111/j.1365-2818.1979.tb00186.x.
[43] E. Olevsky, V. Skorohod, Deformation aspects of anisotropic-porous bodies sintering, J. Phys. IV. 03 (1993) C7–739–C7–742. doi:10.1051/jp4:19937117.
[44] H.E. Exner, E.A. Giess, A Stereology — Based Equation for Isotropic Shrinkage During Sintering by Viscous Flow, in: D.P. Uskoković, H.P. III, R.M. Spriggs (Eds.), Sci. Sinter., Springer US, 1989: pp. 73–82.

[45] F.V. Lenel, H.H. Hausner, O.V. Roman, G.S. Ansell, The influence of gravity in sintering, Sov. Powder Metall. Met. Ceram. 2 (1963) 379–384. doi:10.1007/BF01194674.
[46] E.A. Olevsky, R.M. German, Effect of gravity on dimensional change during sintering—I. Shrinkage anisotropy, Acta Mater. 48 (2000) 1153–1166. doi:10.1016/S1359-6454(99)00368-7.
[47] E. Torresani, Studio sulle variazioni dimensionali in sinterizzazione, n.d.
[48] I. Cristofolini, F. Selber, C. Menapace, M. Pilla, A. Molinari, S. Libardi, Anisotropy of Dimensional Variation and its Effect on Precision of Sintered Parts, Euro PM2012 Congr. Exhib. Shrewsbury UK Eur. Powder Metall. Assoc. EPMA. (2012) 16–19.
[49] I. Cristofolini, C. Menapace, M. Cazzolli, A. Rao, W. Pahl, A. Molinari, The effect of anisotropic dimensional change on the precision of steel parts produced by powder metallurgy, J. Mater. Process. Technol. 212 (2012) 1513–1519. doi:10.1016/j.jmatprotec.2012.02.009.

Chapter III

Experimental procedure

3.1 Measurements of dimensional changes

3.1.1 Introduction

The anisotropic dimensional changes during the sintering were studied in this work using an atomized iron powder with 25% of the particles having a diameter lower than 45µm, mixed with 0.6%$_{wt}$ amide wax as lubricant. The mixture was cold compacted to produce two geometries and different densities:

- Charpy impact bars (55 mm x 10 mm x 10 mm) with 6.9 g/cm^3 green density that were delubed at 550°C for one hour in argon.
- Rings (ϕ_{ext}= 100mm, ϕ_{int}= 40mm, h= 40mm) of 5 different green densities: 6.5 g/cm^3, 6.7 g/cm^3, 6.9 g/cm^3, 7.2 g/cm^3 and 7.3 g/cm^3. They were delubed at 550°C for one hour in argon/hydrogen mixture gas.

In order to study the dimensional changes in the different directions, prismatic specimens with a length of 10 mm and section area of 3 x 3 mm^2 were cut from the Charpy bars and the rings along the direction of the compaction (longitudinal) and in the compaction plane (transversal), as shown in Figure (3.1).

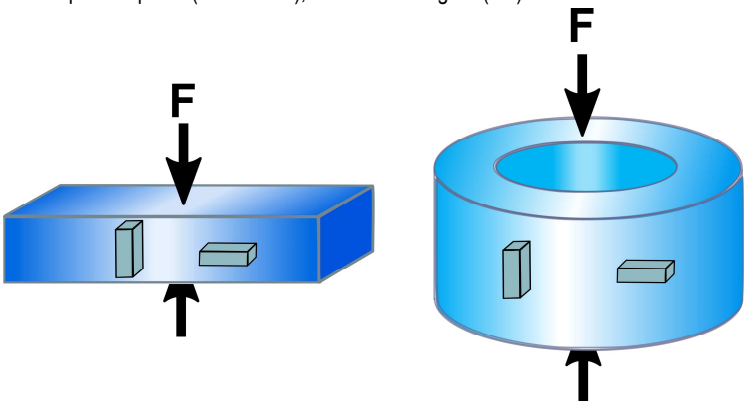

Figure 3.1. The two components used in this work a) Charpy bar, b) ring , and the specimens obtained from these along the longitudinal direction and the transversal one.

3.1.2 Dilatometric analysis

The dimensional changes during sintering were analyzed using a quench dilatometer (DIL805A/D Bähr TA instrument), the principal parts of which are shown in Figure (3.2).

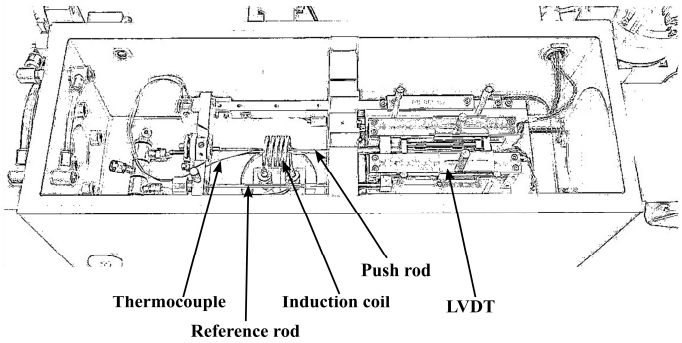

Figure 3.2. Representation of the chamber of inductively heated dilatometer.

The change in length is measured using two push rods made of fused quartz attached to a linear variable differential transformer (LVDT). The sample is heated using a high-frequency current through the inductor composed by a water cooled copper coil. A thermocouple made of Pt-$Pt_{90}Rh_{10}$ is welded on the sample and is used to measure and control the temperature during the entire thermal cycle (Figure (3.3)).

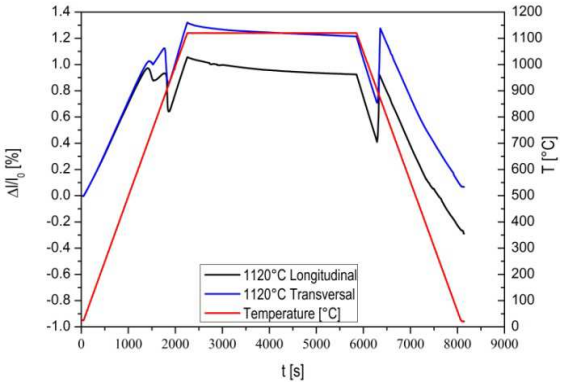

Figure 3.3. Dilatometry curves at 1120°C along longitudinal and transversal directions.

The experiments were performed in Argon in order to create a protective atmosphere and avoid the oxidation of specimens. For the specimens cut from the Charpy bars tests were carried with isothermal holding at temperatures in the range between 640°C and 1120°C, with a heating rate of 0.5°C/s and 3600s of isothermal holding. The same experimental conditions were used for the tests on specimens obtained from the rings, but only the lowest and highest temperatures of the range (640°C and 1120°C) were analyzed.

3.2 Micorstructure characterization

3.2.1 Image analysis

The dilatometric specimens obtained from the Charpy bars and sintered at 640°C, 730°C, 860°C, 960°C and 1120°C and a green specimen of each density of the rings were mounted in a cold cured epoxy resin to obtain metallographic samples. The preparation of the surface consisted in an initial grinding using a set of silica carbide papers (sandpapers), performed in order to remove the superficial layer of resin and obtain a smooth surface. The second step of the preparation consisted in the opening of porosity in order to observe the real structure of the material. This was attained using nylon polishing cloth and the following abrasives:

- ✓ 3 μm diamond paste;
- ✓ 1 μm diamond paste;
- ✓ 0.04 μm colloidal silica suspension OP-S.

During these steps the samples, especially the green and that sintered at 640°C, were handled very carefully in order to avoid the detachments of the powder particles. Images of the material structure were taken using a SEM microscope with a magnification between 200X and 5000X, which allowed to measure the internal and external neck radii and determine the coordination numbers of the particles. The measurement of the dimensions of the radii were obtained using an open sources software of image analysis: ImageJ®.

3.2.1.1 *Measurements of internal and external radii of the neck.*

The two sphere model proposed in the classical theory (Figure (3.4a)) of sintering considers the presence of a punctual contact in the first stage of sintering. Starting from this initial condition (a>>X with reference to Figure (3.4)) the external radius can be derived using the simplified geometrical correlation shown in Equation (3.1):

$$r = \frac{X^2}{4(a - X)} \approx \frac{X^2}{4a} \tag{3.1}$$

In this study the two sphere model is modified and the new configuration is shown in Figure (3.4b), where the deformation of the particles due to prior cold compaction ($a_N \neq a$) is considered and the initial contact is correlated to other geometrical parameters of the sphere.

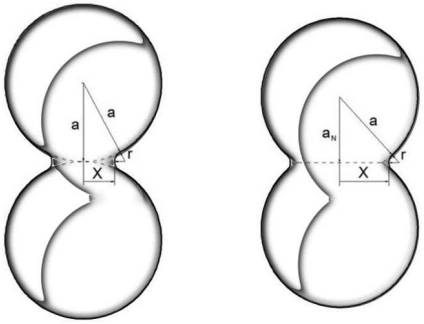

Figure 3.4. Two sphere model: a) classical theory (a>>X), b) new model (a ≈ X).

In this new model the correlation that links the dimensions of the powder particles and of the contact areas is no more the simple Equation (3.1), but can be expressed by Equation (3.2):

$$r = \frac{X^2 - a^2 + a_N^2}{4(a - X)} \tag{3.2}$$

Analysing SEM images at higher magnification (800 x - 5000 x) using the image analysis software ImageJ®, the external contact radius in a sample pre-sintered at low temperature was measured.

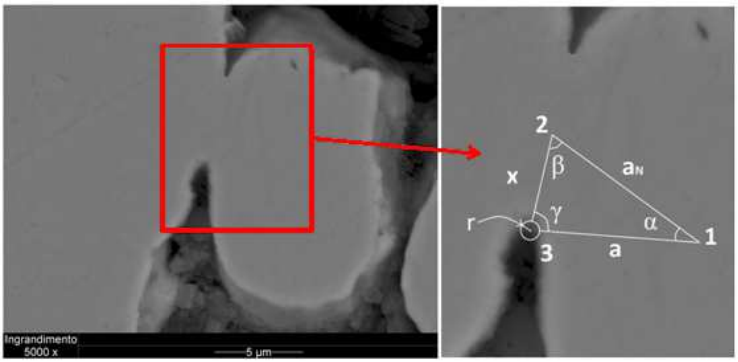

Figure 3.5. Measurment of geometrical parameter of particles to calculate the external neck radius.

As shown in Figure (3.5) the powder particle is considered as an ellipse of which the radii a and a_N were measured. The radius a_N connects the centre of particle to the middle point of the neck and *a* joins the centre with the border of the particle in correspondence of the circle tangent to the two particles that has the same radius of the neck. Moreover the semi contact length (internal neck radius) X and the angles (α, β and γ) of the triangle formed by the segments that represent the two radii (a_N and a) and the internal neck radius were measured. Using the simple trigonometric correlation represented by the Equation (3.3) the external neck radius is determined:

$$r = a_N \frac{\sin(\alpha)}{\sin(\gamma)} - X \qquad (3.3)$$

The internal neck radius was also measured in specimens sintered at different temperatures (640°C, 730°C, 860°C 960°C and 1120C°C) and were used SEM images between 200 x and 800 x of magnification in order to have a broader view of the microstructure. As shown by Figure (3.6) the contacts are disposed not only along the principal direction longitudinal and transversal but are also inclined.

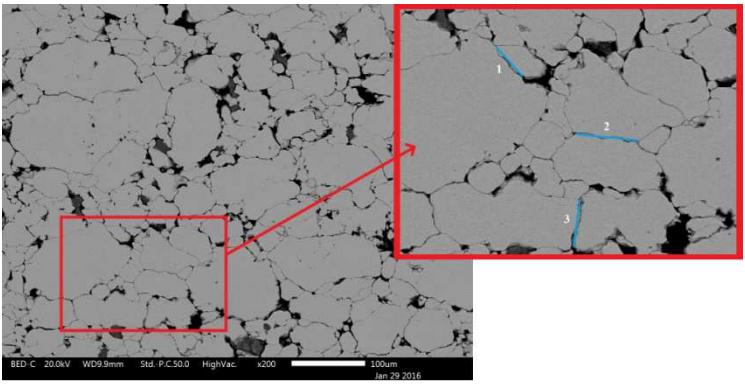

Figure 3.6 Measurement of the length of contacts: 1) inclined, 2) transversal, 3) longitudinal.

In case of inclined contact (contact 1 in Figure (3.6)) its length was distributed between the two main directions and determined through simple trigonometric correlations.

Regarding this image analysis method it is necessary to consider that the plan of the metallographic section intersects the particles and the neck cross sections at a statistically variable distance from the centres and with a statistically variable inclination from the perpendicular and the horizontal directions. This experimental uncertainty derives directly from the surface preparation technique used to prepare the metallographic samples and cannot be avoided. Consequently, the experimental measurements do not correspond to the value of the geometrical parameters at the baricentric section and there is the necessity to introduce correction coefficients. The construction of a geometrical model of the green parts was needed to determine these correction parameters of the measured dimensions. For this purpose, a model was obtained using a cluster of “deformed” spheres and different geometrical arrangements of spheres (Figure (3.7)) were compared to select the more representative:

- ✓ simple cubic structure,
- ✓ body-centred cubic structure with the centre sphere smaller than the edge ones;
- ✓ hexagonal close packed structure.

From these the particles cluster arrangement that allows to model all the possible orientations of neck radius was selected .

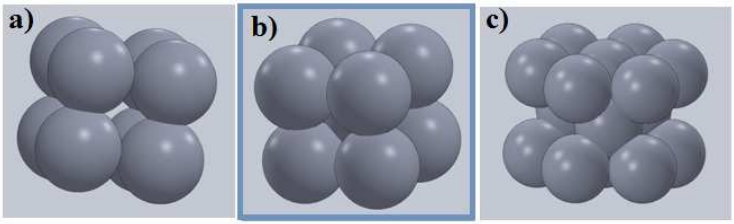

Figure 3.7. Cluster of "deformed" sphere: a) simple cubic, b) body-centred cubic, c) hexagonal close packed structure.

As marked in Figure (3.7) the body-centred cubic was selected as the one that permits to observe the all possible combination of neck radius through different metallographic sections (Figure (3.8)):

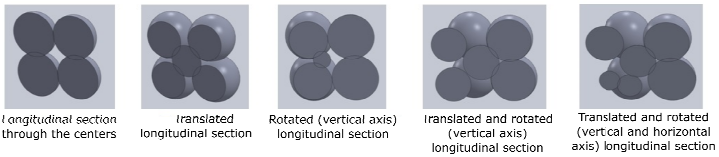

Figure 3.8. Different combination of translation and rotation of section plane in bbc structure.

Using an imaginary section plane that passes through the cluster in different combination of translation and rotation along the different axis it may be observed how the contact length appears "deformed" respect its value in the barycentrical section.

3.2.1.2 ***Coordination number***

The coordination number was measured using SEM images at magnification between 200 x and 800 x. Using the same procedure used for the contact length they were measured the number of contacts, their extension and the inclination in order to divide the contribution along the two directions (Figure (3.6)).

For each particle analysed every contact was considered as circular.

Its projected area along the two directions and the fraction of the total area of the contacts has been calculated. Equation (3.4) is referred to the projected area in the compaction plane (X):

$$A_i^X(\%) = \frac{A_i^X}{\sum_{i=1}^{n} A_i^X} 100 \qquad (3.4)$$

This was used to obtain a coordination number “corrected” in order to consider the extension of the contact and its orientation.

3.3 Quantitative analysis of dislocation density

It has been observed that inside the numerous grains which constitute the polycrystalline materials a complex patterns of heterogeneity are developed during deformation, caused due the presence of grain/sub-grain boundaries, different orientation of grains, second phase particles, twins, etc. These are composed by the dislocation generated during the plastic deformation due the presence of limits to the free paths of mobile dislocation that results in local phenomena (i.e. pile-ups). However the basic physical mechanisms of dislocation generation is not completely clear and is still debatable is some cases.

In literature some works that use a mechanics point of view to describe the dislocations classify them as proposed by Ashby [1] in two typology:

- Statistically store dislocations (SSDs);
- Geometrically necessary dislocations (GNDs).

Whit GNDs were classified the dislocation that cause a lattice curvature in presence of any non-uniform plastic strain without contribute to the plastic strain but they increase the work hardening hindering the motion of the SSDs GNDs are extra dislocation into Burger’s circuit to relax plastic strain gradient while statistically stored dislocations (SSDs) glide to relax the stress [2]. On the other hand the SSDs do not contribute to the lattice curvature and their net Burgers vector is without misclosure effect.

Measuring experimentally the dislocation density is fundamental to understand the deformation mechanics. Some different experimental methods are capable to obtain the GND density as TEM based techniques [3], EBSD microscopy based techniques in 2D [4] and 3D [5], X-ray microscopy based technique [6] and ISE based technique [7].

In this work they have been used both the ISE and EBSD microscopy based techniques which will be described below.

3.3.1 ISE

3.3.1.1 *Nanoindentation*

Before performing the measurements on a real cold compacted components the experimental procedure was set up using a model that simulates the powder particles. With this purpose some copper spheres with diameter between 2.5 and 3 mm were compacted in a die using two different pressures: 156 MPa and 500 MPa. Some deformed and undeferomed spheres were selected and incorporated in a cold cured epoxy resin in order to prepare a metallographic sample in correspondence of their barycentric section. After an accurate surface preparation a set of micro-hardness measurements using three different loads (0.2N, 0.1N and 0.05N) were collected for the undeformed sphere at the edge and for the deformed sphere in correspondence of the contact area. (Figure(3.11)).

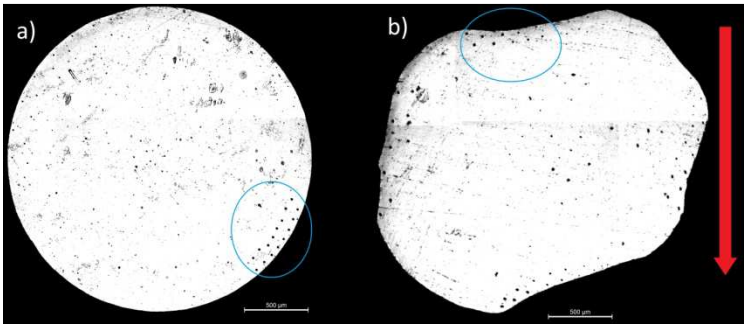

Figure 3.11. Barycentric section: a) undeformed sphere, b) deformed sphere. In the blue circles are shown the microindentation imprints.

The dilatometric samples sintered at 640°C, 730°C, 860°C and 960°C were mounted in thermosetting resin. Surfaces were prepared according to the method used for the metallographic samples described above. A special care was used for polishing these samples because the nanoindentation is a technique very sensitive to the quality of surface preparation and to the possible presence of a deformation and the consequent hardening of the material caused by scratches derived from the diamond paste and the colloidal silica suspension. The importance and difficulties of surface preparation of the specimen will be discussed in details after the description of the methods.

The nanoindentation measurements were performed using the mechanical tester CB500 (NANOVEA). As shown in Figure (3.12) this is equipped with an automated planar X-Y stage (50mm x 100mm) above which is located the sample stage and a

vertical Z stage (25 mm) where there are the nano-testing module and a video zoom microscope.

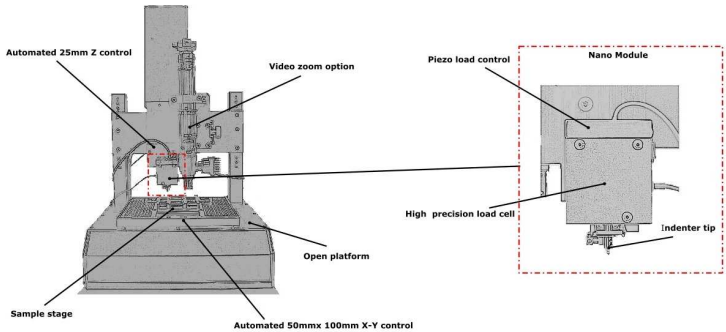

Figure 3.12. Representation of nanoindenter (a) and nano module (b).

On the nano module it is mounted a standard Berkovic tip that is characterized by the geometrical parameters reported in Table (3.1), over there are present the load cell and the piezo load control.

Parameter	Value
α_t	141.9°
α	65.03°
A_d/h^2	$3\sqrt{3} \cdot \frac{\sin\alpha}{\cos^2\alpha} \approx 26.97$
A_p/h^2	$3\sqrt{3} \cdot \tan^2\alpha \approx 24.494$
A_d/A_p	$1/\sin\alpha \approx 1.1010$

Table 3.1. Angle and area data for the Berkovic indenter where α_t is the total included angle, α is the angle between the axis and the faces of the pyramids, A_d is the developed contact area and A_p is the projected contact area.

The nanoindentations were performed in order to measure the dislocation density in the contact area between the powder particles along the different directions. Therefore the indentation were located at the edge of the particles in correspondence of a contact with another particle as shown in Figure (3.13).

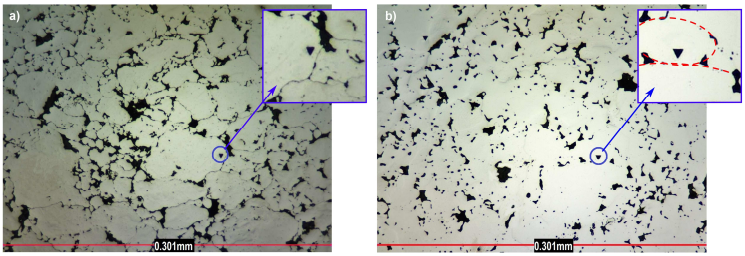

Figure 3.13. Nanoindentation imprints on sintered samples: a) 640°C, b) 1120°C.

In this work three different loads: 55 mN, 75 mN and 95 mN were used and maintained for 20s before unloading.
From the hardness measurements the values of dislocation density using the Indentation Size Effect (ISE) [7,16,17] were obtained.

3.3.1.1.1 Specimens preparation and measurements.

As introduced above the specimens preparation has a fundamental importance in order to obtain quality experimental data to be analyzed using the ISE. The issues in the surface preparation can be divided in three groups:

- ✓ Surface contamination: oxides, thin organic and contaminants layer;
- ✓ Mechanical damage from surface preparation;
- ✓ Surface roughness.

When contaminants are present on the surface, a variation in hardness value with the depth can be measured but that is due to the presence of a layer with a different hardness from the bulk of specimens and not for an intrinsic characteristic of material. The mechanical damage from the surface preparation is an extremely important factor that influences the hardness measurements. Obtaining a good surface finish is not sufficient to obtain a surface that is free from mechanical damage and the consequent increase in hardness at small depths due the deformed layer at the surface. Related to this point some works show how the surface preparation and the relative hardness measurements can influence the indentation size effect results. In two different works the ISE is studied analyzing a Cu single-crystal [18,19] where different surface preparations were used. The first method consists in the surface polishing using the 0.06 μm colloidal suspension, the second method used was the electropolishing technique [19]. As shown in Figure (3.14) the difference in the results obtained from ISE model is appreciable.

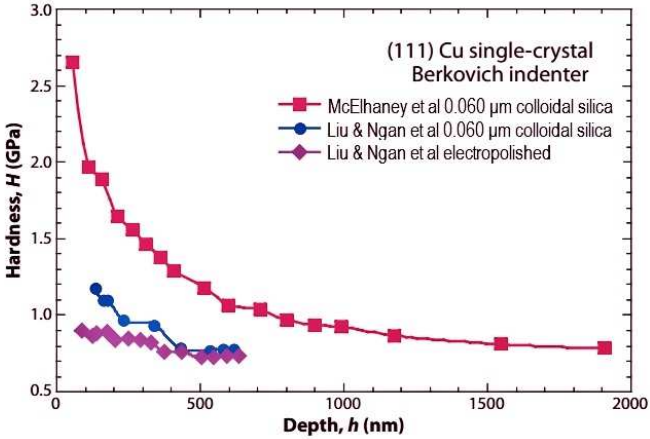

Figure 3.14 ISE data for (111) Cu single crystal obtained in McElhaney et al. work [18] and in Liu & Ngan [19] work using the nanoindentation measurements.

Comparing the ISE measurements obtained in the work of Liu & Ngan [19] with those present in McELhaney's work [18] for samples polished with colloidal silica it is possible to notice how they are significantly different, but comparing them with the results of electropolished sample they are quite similar. It confirms how the different quality in surface preparation has a fundamental importance in the nanoindentation technique and consequently in the ISE analysis.
Lastly the surface roughness influences the accuracy and introduces a significant error in hardness measurements when its dimension is comparable to the indentation depth [20,21].

3.3.2 EBSD

In recent years the electron backscattering diffraction (BESD) has acquired importance as an analytical technique for the crystallographic aspects of microstructure.
An interesting application of EBSD consists in its capability to quantify the elastic and plastic contribution to strain. Elastic and plastic strain indeed appear differently in EBSD, corresponding to a different Kikuchi pattern. (Figure (3.15)).

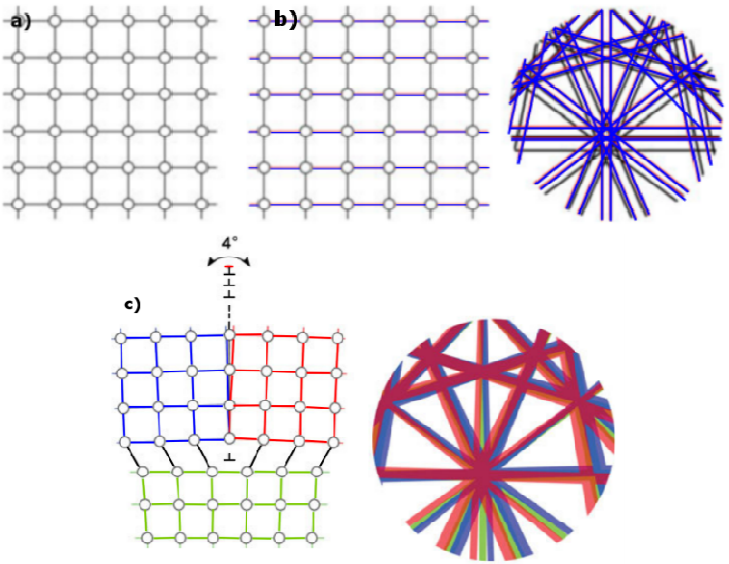

Figure 3.15. scheme for a crystal lattice and relative comparison between undeformed a) and patterns for b) stained and c) subgrain boundary.

The capability of EBSD to capture and process these patterns results in an absolute lattice orientation precision of around 2° [22] and angular resolution of 0.5° [23] which permits to utilise Nye/Kröner's theories to obtain the lattice orientation gradients and hence the dislocation density tensor.
The samples have to be prepared carefully in order to obtain a perfectly flat surface and to avoid to introduce plastic strain during polishing, that degradates the quality of diffraction patterns.
The EBSD based dislocation density resolution (ρ_G^{min}) depends on several factors: binning size, angular resolution and step size.

$$\rho_G^{min} = \frac{\text{Angular Resolution [rad]}}{\text{Step size [m]} \times \text{Burger's vector [m]}} \qquad (3.17)$$

A critical issue in dislocation density analysis is choosing the appropriate step size since it must be not too large to neglect the variation in the dislocation cell structure (undulations in the lattice curvature) and not too small to introduce measurement

error. Since the SSDs were typically stored in dipoles and multipoles, if the step size is small enough to separate the dipoles and to attribute part of the contribution from the SSDs to GNDs, all the SSDs may be recognized as GNDs. For the practice, this last case is not desired due to the resulting measurement noise (Equation (3.17)). Typically, the step size is either at the length scale of the dislocation cell structure or smaller, in order to reveal most of the dislocation networks.
The validation of the EBSD equipment used in this work (Bruker e-Falsh combined with SEM Quanta 600) was carried out canning a selected area on a single crystal Ge sample with appropriate setup.

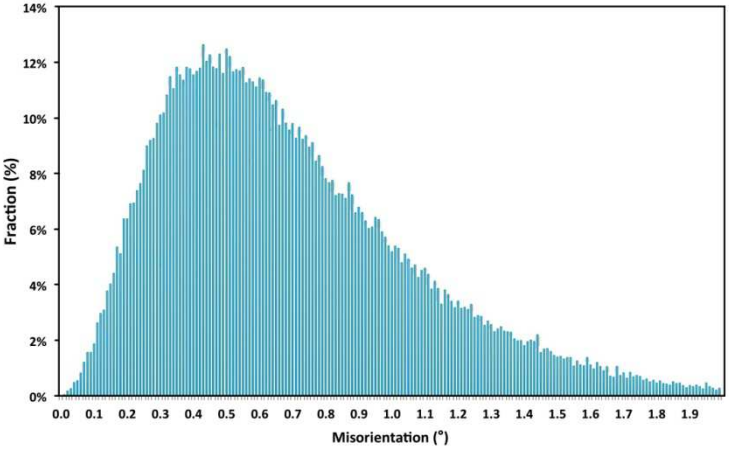

Figure 3.16. Angular Resolution of Bruker e-Flash combined with SEM Quanta 600.

From the resulting histogram distribution shown in Figure (3.16), a peak was found around 0.4° that correspond to the angular resolution of the EBSD system. The resulting combination with the measured GND density distribution (Figure (3.17)) shows that the measured GND densities are above the resolution limit. Hence the calculated data based on Nye tensor is validated.

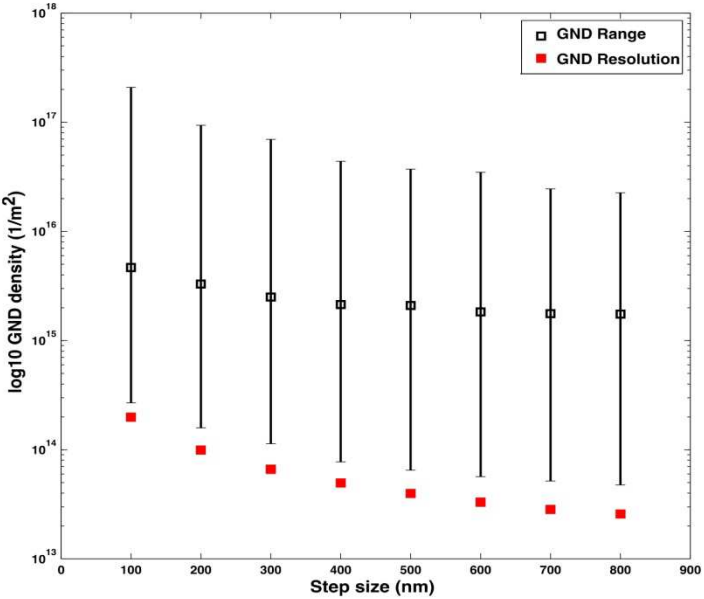

Figure 3.17. Measured GND density range compared with the GND density resolution limit predicated based on angular resolution of EBSD system.

The Nye tensor (Equation (3.18)) can be applied to EBSD technique:

$$\alpha_{ij} = -\epsilon_{klj}\frac{\partial \beta_{ij}^{el}}{\partial x_l} \approx -\epsilon_{klj}\, g_{ij,l} \tag{3.18}$$

where β_{ij}^{el} is the elastic components of the distortion tensor, ϵ_{kij} represents the components of the permutation tensor and $g_{ij,l}$ it the lattice orientation tensor components.

The Frank's loop construction can be used for characterised Burger's vectors, relating the line vector $\hat{\boldsymbol{l}}$, slip direction **b** and the plane normal **r**:

$$\mathbf{B} = \mathbf{b}\left(\hat{\boldsymbol{l}} \cdot \mathbf{r}\right) = \left(\mathbf{b} \otimes \hat{\boldsymbol{l}}\right) \mathbf{r} \tag{3.25}$$

Summing over individual dislocation densities yields the components of total dislocation density tensor and each type of dislocation (N) can be represented by $\hat{\boldsymbol{l}}$ and **b**:

$$\alpha_{ij} = \sum_{n=1}^{N=16} \rho_{GND}^{n} b_i^n \bar{l}_j^n \qquad (3.26)$$

The bcc crystal is characterized by 4 screw <111> type dislocations and 12 edge <111>{110} dislocations, in total are 16 different types, if the negative sign dislocations are ignored. Anyway, only components in the dislocation density tensor compose a set of underdetermined system that has nine equations with 16 unknowns slip system. The active slip system matrix ($\boldsymbol{\xi}$) is formed by slip systems reported in Table (3.2).

Screw dislocations	
$\hat{\boldsymbol{l}}$	$\hat{\mathbf{b}}$
[1 1 1]/√3	[1 1 1]/√3
[1 1 -1]/√3	[1 1 -1]/√3
[-1 1 1]/√3	[-1 1 1]/√3
[1 -1 1]/√3	[1 -1 1]/√3
Edge dislocations	
$\hat{\boldsymbol{l}}$	$\hat{\mathbf{b}}$
[-1 -1 2]/√6	[-1 -1 -1]/√3
[-1 2 -1]/√6	[-1 -1 -1]/√3
[2 -1 -1]/√6	[-1 -1 -1]/√3
[-1 1 -2]/√6	[-1 1 1]/√3
[-1 -2 1]/√6	[-1 1 1]/√3
[2 1 1]/√6	[-1 1 1]/√3
[1 -1 -2]/√6	[1 -1 1]/√3
[1 2 1]/√6	[1 -1 1]/√3
[-2 -1 1]/√6	[1 -1 1]/√3
[1 1 2]/√6	[1 1 -1]/√3
[1 -2 -1]/√6	[1 1 -1]/√3
[-2 1 -1]/√6	[1 1 -1]/√3

Table 3.2. Slip directions and line vectors of dislocations for GNDs in bcc crystal

The lattice orientation gradients ($\boldsymbol{\Lambda}$) is composed by the vectors of Nye tensor as:

$$\xi(9\times16)\cdot(16\times1) = \boldsymbol{\Lambda}(9\times1) \qquad (3.38)$$

L^1-energy minimization scheme is adopted to minimize the total dislocation energy so that the dislocation density vector could be uniquely determined for 9 randomly chose slip system:

$$\rho(9\times1) = \xi^{-1}(9\times9)\cdot\Lambda(9\times1) \tag{3.39}$$

The total dislocation density is obtained from the sum of all the components in ρ(9x9), which correspond to the region where the lattice orientation gradients are extracted on the EBSD map with respect to the neighbouring points, as shown in Figure (3.18).

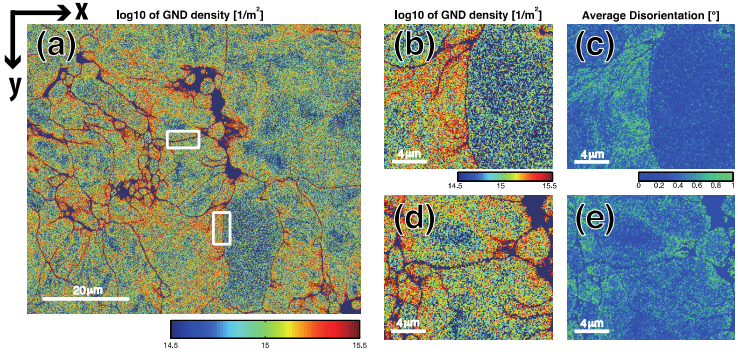

Figure 3.18. GND density distribution measured as log10(dislocations per m²) and average disorientation angle distribution in degrees (a) GND distribution at 100nm step size on the edge of the sample with 2000 magnification; GND density distribution around a particle-particle boundary (b) along y axis and (d) along x axis; Average disorientation angle distribution around a particle-particle boundary (c) along y axis and (e) along x axis.

L^1 total dislocation energy minimisation is commonly utilised norm for solving the underdetermined linear system considering the energy difference between edge and screw dislocations:

$$\frac{E_{edge}}{E_{screw}} = \frac{1}{1-\upsilon} \tag{3.40}$$

Other two minimisation method were compared, L^1 dislocation length minimisation and L^2 least square minimisation of dislocation density and was found that have similar results (Figure (3.19)).

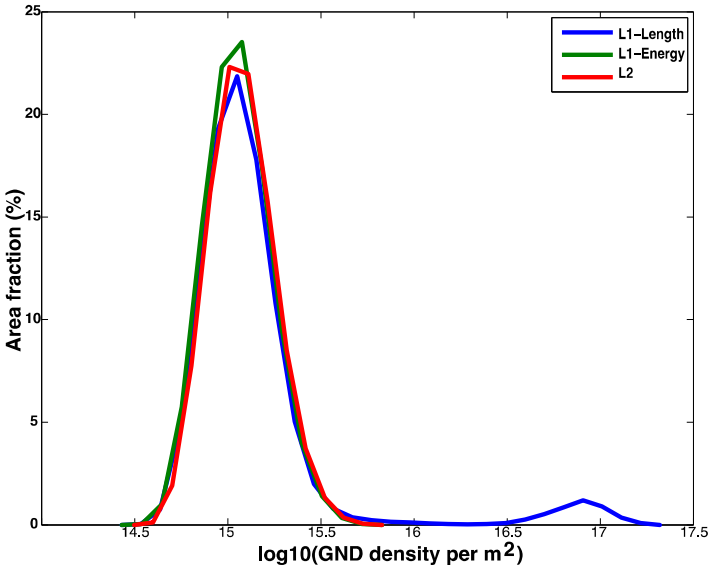

Figure 3.19. Different minimisation schemes compared.

The three minimisation schemes give similar distribution with the only exception for the L^1 length minimisation scheme at very high dislocation density. This is probably due to an overestimation of the dislocation density while the only dislocation length does not reflect physically the lowest possible energy combination of screw and edge dislocations. Accordingly, L^1energy was used in the present work.

3.3.2.1 *Sample preparation and data acquisition.*

Samples were mounted in hot mounting resin and grinded up to 1200 grit. Polishing was made with 3μm, 1μm diamond suspension (DiaDuo Struers) and OP-U Nondry (0.04 μm colloidal silica solution). A final polishing was done using the OP-S activated disk and DI water.

The Argus image collected by the FSE detector at roughly 25mm detector distance from the sample surface were used to pre-selecting the particle boundary. The EBSD scan was done at 20kV and WD of ~15 mm.

The particle contacts could be readily found near two pointed pores. In addition, we could always do a rough scan first and then check the pattern quality image, Figure (3.20).

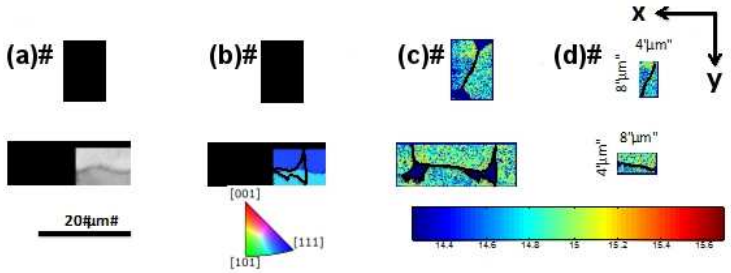

Figure 3.20 Particle boundary selection on a 1010°C sample (a) pattern quality image showing the porosity of the sample and the horizontal and vertical particle boundaries; (b) EBSD scan of the pre-selected regions; (c) log10 (ρ_G [m^{-2}]) map around the particle boundaries; (d) particle boundary selection using a box of 8 by 4 µm along x and y directions.

Then, we decreased the detector distance down to around 15 mm and put masks on the selected particle boundaries for EBSD scans. Three images per sample were collected at a step size of 200 nm at different positions close to the center of the sample surface. Approximately around 15 particles contacts for each direction were detected for every sample (30 for every sample, 120 in total). Instead of doing the EBSD on the entire sample, we only did selected area EBSD scans. Post-processing of the images was done on Matlab® R2014a with our own code for GND calculation (excluding the maximum and minimum GND density). In case of particle boundaries selection, the dimension of the boxes we used to select the specific region from the EBSD scans were set to have the short side of (across any particle contact) exactly 4 µm and the long side of 8 µm (along the contact), see Figure (3.18). The centre of the boxes were selected manually from the EBSD images to accurately keep the particle boundary in the centre of the box .The mean value of the GND was a pixel-wise mean (i.e. sum of total GND for all pixels/#of pixels with nonzero GND).

3.4 References

[1] M.F. Ashby, The deformation of plastically non-homogeneous materials, Philos. Mag. 21 (1970) 399–424.

[2] H. Gao, Y. Huang, Geometrically necessary dislocation and size-dependent plasticity, Scr. Mater. 48 (2003) 113–118.

[3] P.B. Hirsch, A. Howie, R. Nicholson, D. Pashley, M.J. Whelan, Electron microscopy of thin crystals, Butterworths, 1965.

[4] B.S. El-Dasher, B.L. Adams, A.D. Rollett, Viewpoint: experimental recovery of geometrically necessary dislocation density in polycrystals, Scr. Mater. 48 (2003) 141–145.

[5] S. Zaefferer, S.I. Wright, D. Raabe, Three-dimensional orientation microscopy in a focused ion beam–scanning electron microscope: A new dimension of microstructure characterization, Metall. Mater. Trans. A. 39 (2008) 374–389.

[6] B.C. Larson, A. El-Azab, W. Yang, J.Z. Tischler, W. Liu, G.E. Ice, Experimental characterization of the mesoscale dislocation density tensor, Philos. Mag. 87 (2007) 1327–1347.

[7] W.D. Nix, H. Gao, Indentation size effects in crystalline materials: a law for strain gradient plasticity, J. Mech. Phys. Solids. 46 (1998) 411–425.

[8] B. Mott, Microindentation Hardness Testing, Lond. Butterworths. (1957).

[9] H. Bückle, Progress in micro-indentation hardness testing, Metall. Rev. 4 (1959) 49–100.

[10] N. Gane, The direct measurement of the strength of metals on a sub-micrometre scale, in: Proc. R. Soc. Lond. Math. Phys. Eng. Sci., The Royal Society, 1970: pp. 367–391.

[11] D. Tabor, Indentation hardness and its measurement: some cautionary comments, in: Microindentation Tech. Mater. Sci. Eng., ASTM International, 1985.

[12] W.W. Gerberich, N.I. Tymiak, J.C. Grunlan, M.F. Horstemeyer, M.I. Baskes, Interpretations of indentation size effects, J. Appl. Mech. 69 (2002) 433–442.

[13] S.J. Bull, On the origins and mechanisms of the indentation size effect, Z. Für Met. 94 (2003) 787–792.

[14] Y. Huang, S. Qu, K.C. Hwang, M. Li, H. Gao, A conventional theory of mechanism-based strain gradient plasticity, Int. J. Plast. 20 (2004) 753–782.

[15] A. Arsenlis, D.M. Parks, Crystallographic aspects of geometrically-necessary and statistically-stored dislocation density, Acta Mater. 47 (1999) 1597–1611.

[16] M. Barmouz, K. Abrinia, J. khosravi, Using hardness measurement for dislocation densities determination in FSPed metal in order to evaluation of strain rate effect on the tensile behavior, Mater. Sci. Eng. A. 559 (2013) 917–919. doi:10.1016/j.msea.2012.08.086.

[17] D. Faghihi, G.Z. Voyiadjis, Determination of nanoindentation size effects and variable material intrinsic length scale for body-centered cubic metals, Mech. Mater. 44 (2012) 189–211.
[18] K.W. McElhaney, J.J. Vlassak, W.D. Nix, Determination of indenter tip geometry and indentation contact area for depth-sensing indentation experiments, J. Mater. Res. 13 (1998) 1300–1306.
[19] Y. Liu, A.H.W. Ngan, Depth dependence of hardness in copper single crystals measured by nanoindentation, Scr. Mater. 2 (2001) 237–241.
[20] S. Pathak, D. Stojakovic, R. Doherty, S.R. Kalidindi, Importance of surface preparation on the nano-indentation stress-strain curves measured in metals, J. Mater. Res. 24 (2009) 1142–1155.
[21] J.-Y. Kim, S.-K. Kang, J.-J. Lee, J. Jang, Y.-H. Lee, D. Kwon, Influence of surface-roughness on indentation size effect, Acta Mater. 55 (2007) 3555–3562.
[22] P.S. Bate, R.D. Knutsen, I. Brough, F.J. Humphreys, The characterization of low-angle boundaries by EBSD, J. Microsc. 220 (2005) 36–46. doi:10.1111/j.1365-2818.2005.01513.x.
[23] S.I. Wright, A review of automated orientation imaging microscopy(OIM), J. Comput.-Assist. Microsc. 5 (1993) 207–221.
[24] B. Beausir, C. Fressengeas, Disclination densities from EBSD orientation mapping, Int. J. Solids Struct. 50 (2013) 137–146. doi:10.1016/j.ijsolstr.2012.09.016.
[25] W. Pantleon, Resolving the geometrically necessary dislocation content by conventional electron backscattering diffraction, Scr. Mater. 58 (2008) 994–997.
[26] E. Demir, D. Raabe, N. Zaafarani, S. Zaefferer, Investigation of the indentation size effect through the measurement of the geometrically necessary dislocations beneath small indents of different depths using EBSD tomography, Acta Mater. 57 (2009) 559–569.

Chapter IV

Results

Part of this chapter has been published in:

C.Menapace, M.Larsson, E.Torresani, I.Cristofolini, A.Molinari,

"*Study of Anisotropy during Sintering of Ferrous Alloys*",
Proceedings PM2012, 2012 Powder Metallurgy World Congress & Exhibition, Yokohama (Japan) 14-18 October 2012, CD-room, Japan Society of Powder and Powder Metallurgy, ISBN: 978-4-9900214-9-8.

A. Molinari, C. Menapace, E. Torresani, I. Cristofolini, M.Larsson,

"*Working hypothesis for origin of anisotropic sintering shrinkage caused by prior uniaxial cold compaction*",
Powder Metallurgy, 56 [3] (2013) 189-195

A. Molinari, E. Torresani, C. Menapace, I. Cristofolini, M. Larsson,

"*A study of sintering shrinkage kinetics of cold compacted ferrous green parts*",
Advances in Powder Metallurgy and Particulate Materials 5(2013)25-32

E. Torresani, G.Ischia, A. Molinari,

"*Study of deformation of powders due the cold compaction*",
Proceedings EURO PM2014 Congress & Exhibition, Salzburg 21-24 September 2014, ed. EPMA, Shrewsbury (UK), CD room

A. Molinari, E. Torresani,

"*Preliminary study to determine the sintering stress from microstructural analysis of green parts*",
Powder Metallurgy, 58 [5] (2015) 323-327

E. Torresani, I. Cristofolini, A. Molinari,

"*Study of the anisotropic microstructure of the uniaxially cold compacted green parts*",
Advances in Powder Metallurgy and Particulate Materials (2015) 9-18

3.1 Study of shrinkage by Dilatometry: samples at 6.9g/cm^3 green density

3.1.1 Analysis of the dilatometric curves

Some examples of records of dimensional variations obtained at the different temperatures along the longitudinal and transversal directions are reported in Figure (4.1).

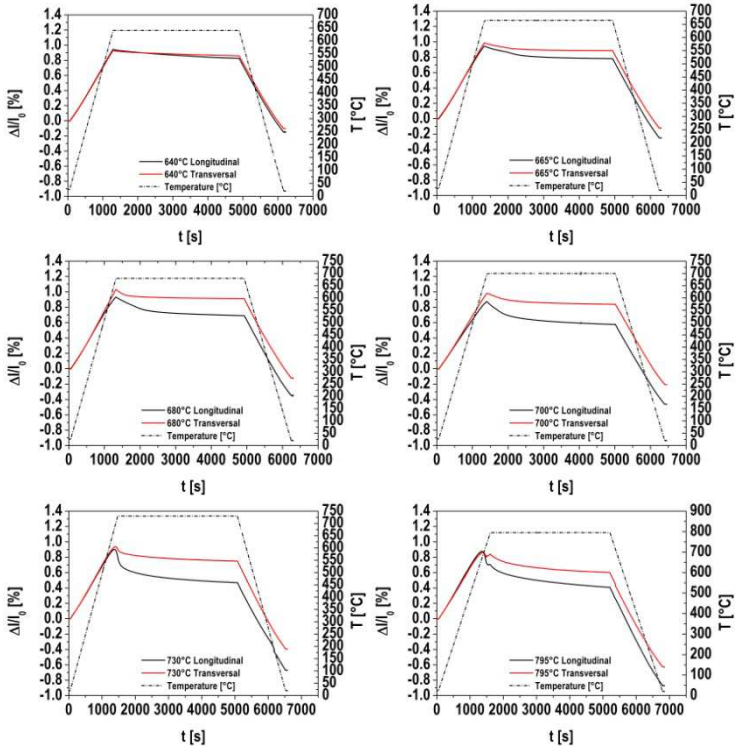

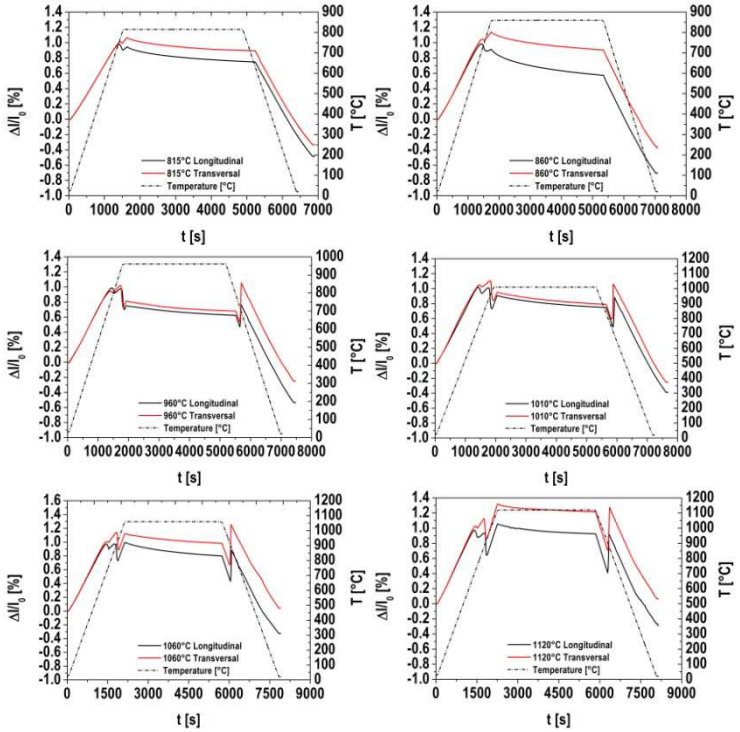

Figure 4.1. Dilatometric curves at different temperatures for the longitudinal and transversal directions.

For all the temperatures the shrinkage of the green compacts is different along the two directions. The curves show a deviation from the linear thermal expansion during the heating ramp, with a different intensity along the two directions, starting at relative low temperature (~400°C - 600°C). Such a behavior is shown in Figure (4.2). This deviation from the theoretical thermal expansion is due to shrinkage, that starts at relatively low temperature with an appreciable anisotropy.

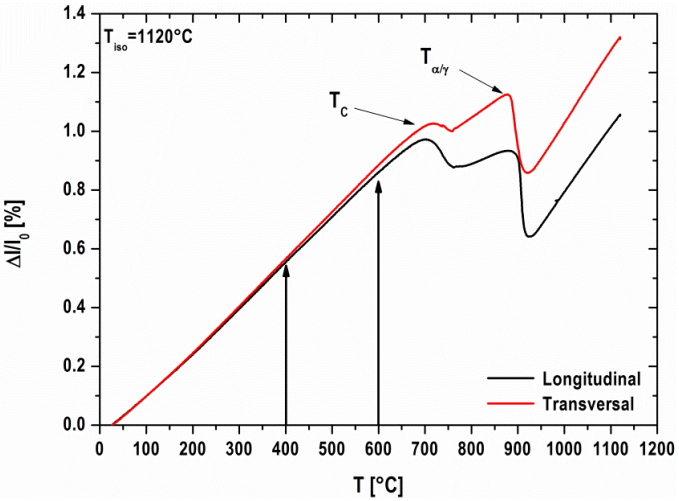

Figure 4.2. Detail of the dilatometric curves at 1120°C of the longitudinal and transversal specimens.

Figure (4.2) shows a maximum of the curve in the correspondence of the Curie temperature followed by a sharp contraction. Above the contraction at T_C, the thermal expansion is still present, smaller than at the beginning of the heating ramp. This indicates that the shrinkage is still very active. These phenomena are more pronounced in the longitudinal specimen than in the transversal one as shown by the different slope of the two curves up to the alpha/gamma transformation temperature. At temperatures above $T_{\alpha/\gamma}$, i.e. in austenite field, the curves show a very similar slope along the two directions.

Back to Figure (4.1), isothermal shrinkage at the different temperatures is anisotropic in alpha filed, while the difference between the two directions in austenite field is quite poor.

Deviation from thermal expansion, that is significant of shrinkage, can be investigated comparing the heating and the cooling ramps of the dilatometric curves, as shown in Figure (4.3) as an example.

The slope of the cooling ramp is correlated to the thermal expansion coefficient, that is not affected by porosity. That of the heating ramp can therefore be compared to the cooling one, to individuate the temperature ranges interested by shrinkage phenomena, and their intensity. Five different temperature ranges were considered:

400-640°C, 650°C-670°C, 670°C-730°C, 800°C-880°C, 940°C-1120°C, the relevant expansion/shrinkage along the different directions was calculated with a linear interpolation and the thermal expansion coefficient was determined from the slope.

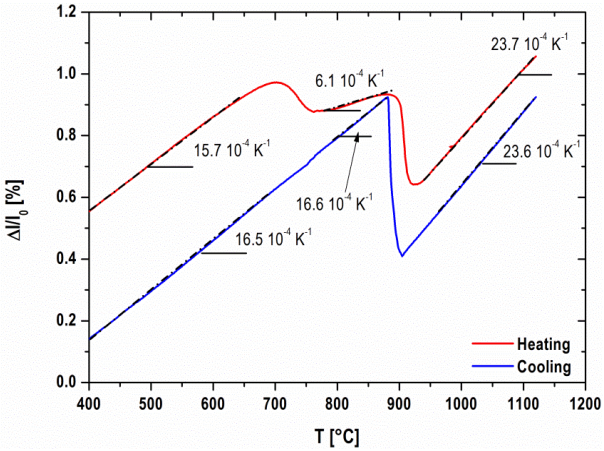

Figure 4.3. Examples of linear interpolation of the dimensional changes during the heating and cooling ramps for the longitudinal direction.

The thermal expansion coefficient for bcc iron increases from 12.2 10^{-6} K^{-1} at 100°C up to 14.6 10^{-6} K^{-1} at 800°C [1]; for fcc iron it is 20.6 10^{-6} K^{-1} [2].
The results of elaboration of the curves are reported in Table (4.1), along with the thermal expansion coefficient of iron.

Thermal Expansion Coefficient α [10^{-6} K^{-1}]						
T Range [°C]	Longitudinal		Transversal		T [°C]	Iron
	Heating	Cooling	Heating	Cooling		
400-650	15.7	16.5	15.6	16.4	**200**	12.9
650-670	11.6	16.0	13.0	16.2	**400**	13.8
670-730	6.4	16.1	10.5	16.2	**600**	14.5
790-880	6.1	16.6	11.0	17.0	**800**	14.6
940-1120	23.7	23.6	22.3	23.9	**γ-Fe**	20.6

Table 4.1. Thermal expansion coefficient during the heating and cooling ramps and iron.

The coefficients of thermal expansion calculated from the cooling ramps are comparable with the thermal expansion coefficient of iron and do not show any appreciable differences between the two directions. Those resulting from the heating ramp show a deviation from the reference data and a dependence on the direction in the ranges 650°C-670°C, 670°C-730°C, 800°C-880°C.
To highlight the results, Figure (4.4) shows the comparison between the real curves and those calculated from the thermal expansion coefficient, as representative of the expansion expected in absence of any shrinkage.

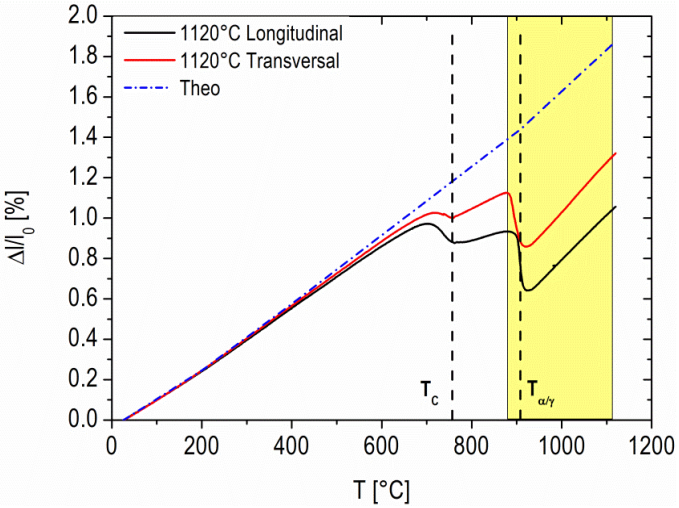

Figure 4.4. Comparison between the theoretical and the experimental thermal expansion in Fe-α paramagnetic field for the longitudinal and transversal directions.

At temperature lower than 600° the thermal expansions along the two directions are comparable to the theoretical one, that means neither shrinkage nor anisotropy. In this temperature range, the diffusive mechanisms promoting shrinkage are not activated. Between T_C and the alpha/gamma transformation temperature an anisotropic shrinkage is clearly indicated. In austenite there is a slightly anisotropic shrinkage.
These results can be interpreted considering the effect of the structural defectiveness introduced by cold compaction, that is very pronounced in alpha field

and is almost negligible in austenite because during the phase transformation the defects introduced by the prior cold compaction are eliminated due the action of recrystallization. The anisotropy above the austenitic transformation temperature can be mostly imputed to the different extension of the interparticle contacts and to the effect of the structural defects responsible for the self-activation.
Anisotropy of dimensional change at the different temperatures is shown in Figure (4.5) where the total isothermal shrinkage at the various temperatures is reported.

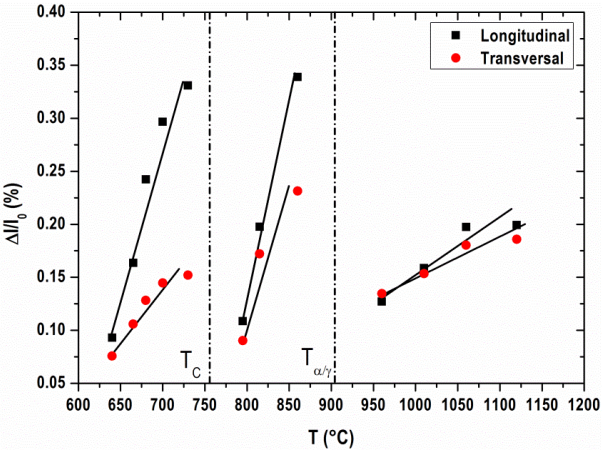

Figure 4.5. Isothermal shrinkage (60min holding) versus the isothermal temperature.

For both directions the shrinkage increases with the isothermal temperature in all the three temperature ranges, but two discontinuities are visible in correspondence of the Curie and of the austenitic transformation temperature, with a sharp decrease on moving from one range to the other. The decrease at the alpha/gamma transformation is due to the smaller self-diffusion coefficient in the fcc lattice than in the bcc lattice. Moreover in the austenitic field, how explained above, the low anisotropy of shrinkage is due to the reduction of the influence of the structural defectiveness on diffusion. The decrease above the Curie temperature can be attributed to the different influence of the structural defectiveness on bulk diffusivity. When the bcc iron is approaching the transition in its magnetic behavior form ferromagnetic to paramagnetic, due to the effects of the magnetic dipole on the atomic flow on the dislocation pipe diffusion, bulk diffusivity results particularly enhanced [3]. An evaluation of the contribution to shrinkage of heating up to and of isothermal holding at a given temperature was made by calculating anisothermal shrinkage at the temperatures shown in Figure (4.6).

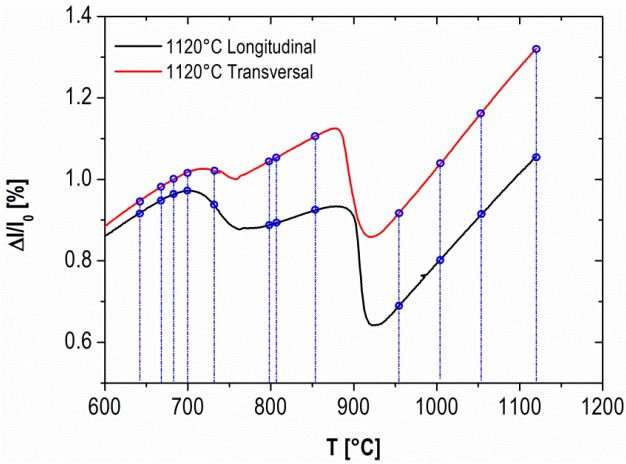

Figure 4.6. Dimensional variations during the heating ramp of the dilatometric test with isothermal temperature of 1120°C, the blue lines are corresponding to the temperatures used in the others dilatometric tests.

As is clearly shown in Figure (4.7(a)) and (4.7(b)), anisothermal shrinkage is higher than the isothermal one at all temperatures

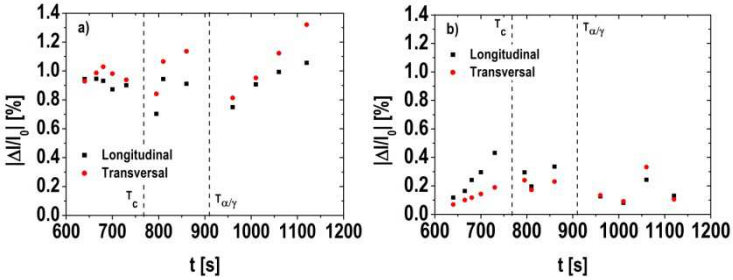

Figure 4.7. Dimensional changes a) due the heating ramp, b) due the isothermal holding.

During heating the difference between the dimensional changes is appreciable and increases with the increasing of the temperature (Figure (4.7(a))). For the dimensional changes during the isothermal holding for the temperatures below Tc, the divergence of dimensional variations increases with temperature, in the paramagnetic field is still present but is quite low, while for temperatures in the austenitic field the dimensional changes along the two directions are comparable. Furthermore in α-Fe, in both the ferromagnetic and paramagnetic field, the

divergence between final and initial anisotropy of dimensional changes increases with the increasing temperature.

To highlight the anisotropy displayed on heating and on isothermal holding, Figure (4.8) shows the difference between the dimensional variations along the two directions during the heating ramp and during the isothermal holding.

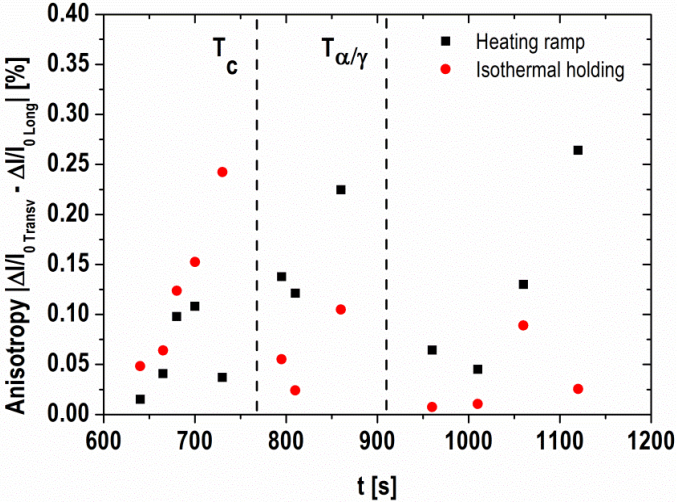

Figure 4.8. Comparison between the contribution of the heating ramp and the isothermal holding to the anisotropy of dimensional variations.

The contribution to anisotropy of dimensional variations from the isothermal holding is greater than that from the heating ramp only in the ferromagnetic field and increases with temperature on approaching T_C In the paramagnetic field and in austenite he trend is reversed, mainly because the contribution from isothermal holding is much smaller than below T_C.

3.1.2 Kinetic analysis

Equation (2.19) describes the shrinkage kinetic during the isothermal holding in function of the predominant mass transport mechanism.

The parameters n, m and B (Table (2.2)) are time dependent but they usually were considered constant and in many previous works this equation was used for identify the sintering mechanism using the exponent *n* [4].

The shrinkage rate during the isothermal holding is not constant (Figure (4.1)), and from the relation between $\log(\Delta l/l_0)$ and log (t) the exponent n can be determined in the whole isothermal range, as shown by some examples in Figure (4.10).

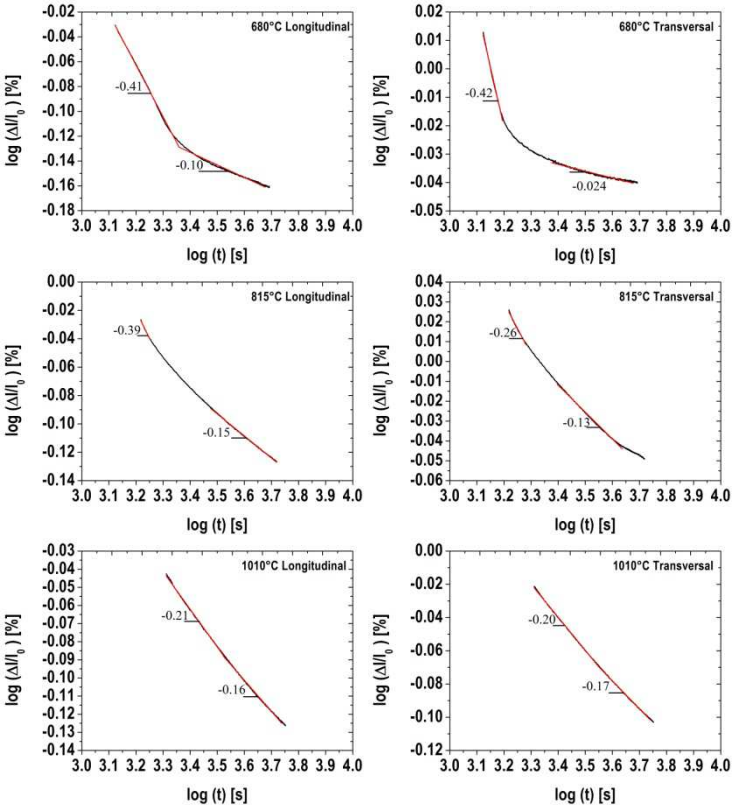

Figure 4.10. Plot of $\log(\Delta l/l_0)$ vs log(t) during the isothermal holding; the slope corresponds to 2*n.

The parameter n is not constant in the isothermal holding time range investigated. It decreases on increasing isothermal time. The greater change is observed for the temperatures below Tc; for the temperatures in the paramagnetic field the change is still appreciable, while in the austenitic field the change is not so pronounced.
The curves were elaborated as in the previous works [5], to calculate the time depending effective diffusion coefficient, resulting from the contribution of dislocation pipe diffusion to bulk diffusion, and affected by the change in the dislocation density during the isothermal holding. Introducing D_{eff} in Equation (2.19) the diffusion coefficient can be expressed as a function of the isothermal holding time:

$$D_{eff} = \frac{\Delta l}{l_0}\left[\frac{2D^3kT}{5\gamma_S\Omega}\right]^{2/5}\frac{1}{t^{2/5}} \qquad (4.1)$$

Using Equation (4.1) the variation of the effective diffusion coefficient during isothermal shrinkage was calculated, and the trends shown in Figure (4.11) are obtained.

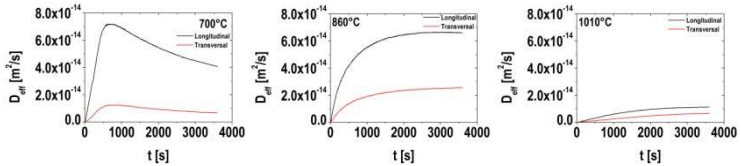

Figure 4.11. Example of effective diffusion coefficient calculated using Equation (4.1) for the volume diffusion mechanisms plotted versus the time of isothermal holding.

D_{eff} has three different trends in the three temperature ranges. Below the T_C it initially increases until reaching a maximum after which if decreases, whereas in the other two temperatures ranges the increase is continuous with a decreasing slope. This trend of the diffusion coefficient can be explained with the presence of opposite mechanisms during sintering that contribute to the variation of the dislocation density in the neck region. The increase in D_{eff} is due to the continuous generation of dislocations at the particles contact surfaces when the defects are rearranged in a high energy grain boundary in the growing neck region, as proposed in Schatt and Friedrich [6–8]. When a critical dislocation density is reached an opposite mechanism is activated: recovery and/or recrystallization.

Once they are activated the dislocation density starts to decrease, and consequently the diffusivity gets progressively attenuated. The dislocation density produced by sintering is in addition to that introduced by prior cold compaction, both contributing to the structural activity. The presence of the maximum in the curves only below T_C demonstrates that the influence of structural activity is greater in this temperature range than in the other two. From the curves shown in Figure (4.11), the maximum effective diffusion coefficient and the weighted mean effective diffusion coefficient were calculated; the results are reported in Figure (4.12) as a function of the temperature.

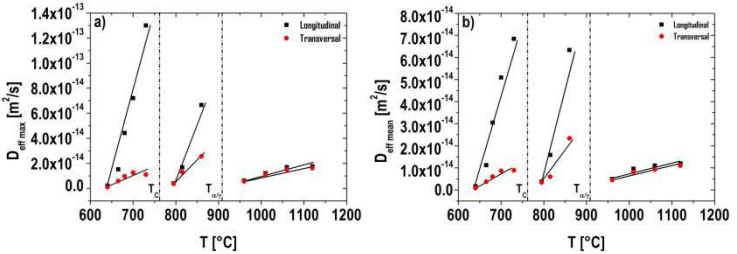

Figure 4.12. a) Maximum and b) mean value of effective diffusion coefficient obtained using Equation (4.1).

The figure shows that within the three temperature ranges both the maximum and the mean effective diffusivity increase with the temperature, and there is a significant difference between the diffusivity in the two directions in alpha phase. The anisotropy and its evolution with the isothermal temperature can be better visualized observing the ratio between the two diffusivities along the transversal and longitudinal directions shown in Figure (4.13).

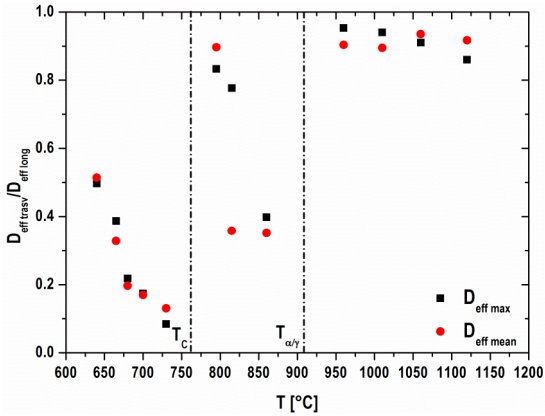

Figure 4.13. Ratio between the two diffusivities along the longitudinal and transversal directions.

It is clearly shown how the increase in temperature in the three ranges causes a progressive enhancement of the anisotropy until reaching the next range, where an attenuation appears. The effective diffusion coefficient expressed with Equation (2.10) is higher than the equilibrium coefficient that corresponds to the bulk diffusivity in presence of an equilibrium density of structural defects that is reported in the literature [1].

α-Fe ferromagnetic					
T [°C]	**640**	**665**	**680**	**700**	**730**
D_v [m²/s]	$1.09\ 10^{-19}$	$4.06\ 10^{-19}$	$8.11\ 10^{-19}$	$1.97\ 10^{-18}$	$6.99\ 10^{-18}$
α-Fe paramagnetic					
T [°C]	**795**	**815**	**860**	--	--
D_v [m²/s]	$1.54\ 10^{-16}$	$3.68\ 10^{-16}$	$7.77\ 10^{-16}$	--	--
γ-Fe					
T [°C]	**960**	**1010**	**1060**	**1120**	--
D_v [m²/s]	$2.71\ 10^{-17}$	$8.85\ 10^{-17}$	$2.64\ 10^{-16}$	$8.85\ 10^{-16}$	--

Table 4.3. Volume diffusivity at equilibrium.

The ratio between the effective diffusivity and the reference values gives the enhancement of diffusivity due to the structural activity. The ratio of the maximum and mean effective diffusion coefficients to the reference coefficient along the two directions is shown in Figure (4.14).

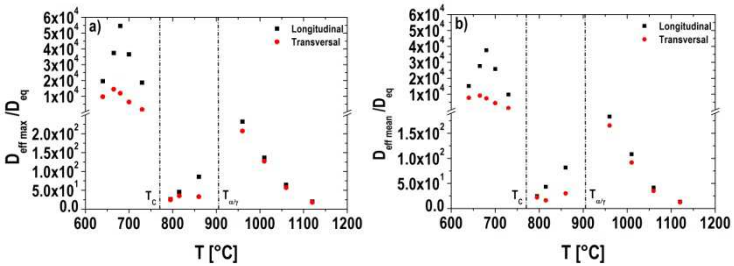

Figure 4.14. a) $D_{eff\ max}/D_{eq}$ and b) $D_{eff\ mean}/D_{eq}$ versus the isothermal temperature

In the temperature range below T_C the structural activity results particularly intense and it is greater along the longitudinal than the transversal direction; the value of diffusivity has four orders of magnitude of difference. At higher temperatures the influence of the structural defects decreases and the resulting maximum enhancement of diffusivity is only by two orders of magnitude but is still higher along the longitudinal direction. In paramagnetic field the structural activity effect is smaller than in ferromagnetic field, moving into the austenite field initially increases but subsequently decreases continuously with increasing the temperature.

The analysis of the results of the dilatometric tests confirm the conclusion that the sintering kinetic, in uniaxially cold compacted pure iron, is influenced by the different plastic deformation of the material during cold compaction along the longitudinal and transversal directions. The effects of cold compaction that influence anisotropy of dimensional changes can be divided in two typology: structural activity, that groups the influence of the structural defectiveness on the bulk diffusivity, and the geometrical activity, that considers the influence of the different extension of the interparticle contact areas in the green parts.

3.1.2.1 *Diffusivity Equation*

The correlation between the effective diffusion coefficient and time shown in Figure (4.11) may be fitted by Equation (4.2) [5,9]:

$$D_{eff} = \frac{t}{a + bt - ct^{0.97}} \qquad (4.2)$$

An example of fitting is reported in Figure (4.15).

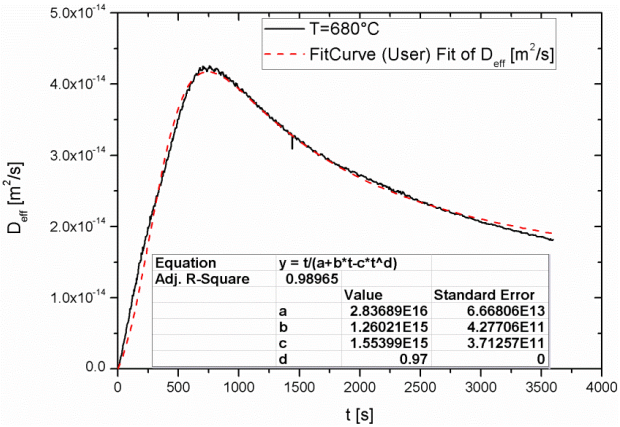

Figure 4.15. Example of fitting of experimental curve. (Longitudinal direction with isothermal holding at 680°C).

The Equation (4.2) fits experimental data quite well at all temperatures investigated with the only exception of the data relevant to the lower temperature.
All the results for the parameters *a*, *b*, and *c* are reported in Table (4.4)

	Longitudinal			Transversal		
T [°C]	**a**	**b**	**c**	**a**	**b**	**c**
640	$6.00 \cdot 10^{17}$	$3.50 \cdot 10^{14}$	$5.54 \cdot 10^{14}$	$8.92 \cdot 10^{17}$	$7.68 \cdot 10^{14}$	$1.42 \cdot 10^{16}$
665	$1.69 \cdot 10^{17}$	$4.28 \cdot 10^{15}$	$5.38 \cdot 10^{15}$	$2.28 \cdot 10^{17}$	$1.02 \cdot 10^{16}$	$1.26 \cdot 10^{16}$
680	$3.72 \cdot 10^{16}$	$1.22 \cdot 10^{15}$	$1.52 \cdot 10^{15}$	$3.16 \cdot 10^{16}$	$3.36 \cdot 10^{15}$	$4.04 \cdot 10^{15}$
700	$1.07 \cdot 10^{16}$	$4.69 \cdot 10^{14}$	$5.72 \cdot 10^{14}$	$7.52 \cdot 10^{16}$	$3.13 \cdot 10^{15}$	$3.85 \cdot 10^{15}$
730	$5.63 \cdot 10^{14}$	$1.38 \cdot 10^{14}$	$1.57 \cdot 10^{14}$	$4.51 \cdot 10^{15}$	$6.47 \cdot 10^{14}$	$6.78 \cdot 10^{14}$
795	$5.08 \cdot 10^{16}$	$1.36 \cdot 10^{15}$	$1.36 \cdot 10^{15}$	$6.79 \cdot 10^{16}$	$1.01 \cdot 10^{15}$	$1.10 \cdot 10^{15}$
815	$3.11 \cdot 10^{16}$	$3.19 \cdot 10^{14}$	$3.43 \cdot 10^{14}$	$5.92 \cdot 10^{16}$	$8.24 \cdot 10^{14}$	$9.70 \cdot 10^{14}$
860	$6.99 \cdot 10^{15}$	$6.47 \cdot 10^{13}$	$6.61 \cdot 10^{13}$	$2.40 \cdot 10^{16}$	$1.36 \cdot 10^{14}$	$1.32 \cdot 10^{14}$
960	$3.84 \cdot 10^{17}$	$1.31 \cdot 10^{15}$	$1.62 \cdot 10^{15}$	$3.16 \cdot 10^{17}$	$3.41 \cdot 10^{15}$	$4.30 \cdot 10^{15}$
1010	$1.87 \cdot 10^{17}$	$1.47 \cdot 10^{15}$	$1.83 \cdot 10^{15}$	$1.52 \cdot 10^{17}$	$7.74 \cdot 10^{14}$	$9.40 \cdot 10^{14}$
1060	$1.17 \cdot 10^{16}$	$8.37 \cdot 10^{13}$	$1.01 \cdot 10^{14}$	$2.49 \cdot 10^{17}$	$1.82 \cdot 10^{15}$	$2.27 \cdot 10^{14}$
1120	$1.16 \cdot 10^{17}$	$1.48 \cdot 10^{15}$	$1.77 \cdot 10^{15}$	$4.57 \cdot 10^{17}$	$6.44 \cdot 10^{14}$	$5.36 \cdot 10^{14}$

Table 4.2. Parameters a, b and c of Equation (4.2) at the different temperatures and for the two directions.

The plot of the parameters in Figure (4.16) highlights their correlation with temperature ranges with the exception of the data relevant to the lowest temperature:

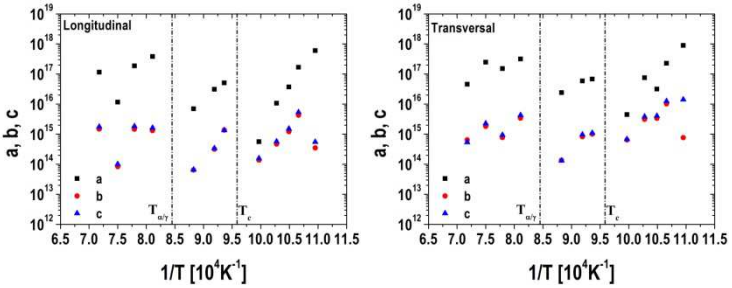

Figure 4.16. Parameters a, b and c of Equation (4.2) versus 1/T.

Figure (4.16) shows a linear correlation in the three temperature ranges between the logarithm of the parameters and 1/T. Therefore the model of the effective diffusion coefficient may be completed by the following Equations (4.3) (4.4) and (4.5) describing the parameters a, b and *c* as a function of the temperature:

$$\log a = m_a T + q_a \qquad (4.3)$$

$$\log b = m_b T + qb \qquad (4.4)$$

$$\log c = m_c T + q_c \qquad (4.5)$$

where T is the temperature in Celsius; the values of m_a, m_b, m_c, q_a, q_b and q_c for the three temperature ranges are reported in Table (4.5).

	Ferromagnetic		Paramagnetic		Austenite	
Parameters	**Long**	**Transv**	**Long**	**Transv**	**Long**	**Transv**
m_a	-0.034	-0.024	-0.013	-0.07	-0.05	-0.005
q_a	39.6	33.7	27.4	22.6	22.0	22.0
$m_b = m_c$	-0.022	-0.019	-0.020	-0.014	-0.002	-0.003
$q_b = q_c$	30.5	29.1	30.5	26.3	16.8	18.7

Table 4.5. Parameters for Equation (4.3) - (4.5)

Considering that the values of m_b and q_b are very similar to m_c and q_c, respectively, Equation (4.2) can be rewritten as:

$$D_{eff} = \frac{t}{a + b\left(t - t^{0.97}\right)} \tag{4.6}$$

That, along with eq. (4.3), (4.4) and (4.5), represents the time and temperature dependence of the effective diffusion coefficient.
Equation (4.2) does not have a physical meaning related to the generation of dislocations and the recovery/recrystallization, that are respectively the phenomena responsible for the initial increase and the subsequent decrease in the effective diffusion coefficient. The theory of the dislocation pipe diffusion proposes a linear correlation between volume diffusion and dislocation density as shown in Equation (2.10). Therefore the time dependence of the effective diffusion coefficient should be a combination of:

- the square root dependence proposed by Schatt and Friedrich [6–8] for the increase in the dislocation density in the neck region;
- a linear dependence with ρ^{-1} if the recovery is controlled by the dislocation climb (for material with high stacking fault energy, as the case of α-iron) that begins only after a given dislocation density has been reached.

These elaboration of shrinkage curves is based on the two sphere model which does not take into account the different extension of the contact areas along the directions parallel to the compaction and transversal, which also has an influence on anisotropy.
The contact area between the deformed particles is an aspect that cannot be neglected in the diffusion process since it is the source of atoms diffusing toward the neck and the intensity of the flux is proportional to the extension of the contact. How explained before the geometrical activity influences the anisotropy mostly in the austenitic field where its contribution dominates over that given by dislocations, because the most part of the strain hardening is eliminated by the alpha/ gamma phase transformation.

3.2 Analysis of the structural and geometrical activity

All the conclusion and all data relevant to diffusivity shown in the Section 4.1 derive from the elaboration of the isothermal shrinkage curves, modifying the shrinkage kinetic model given by Equation (2.19), which is based on the two-sphere model. How remarked before this model does not consider plastic deformation caused by cold compaction, which introduces a high density of structural defects, mainly dislocations, in the contact regions and the formation of an interparticle contact area that cannot be approximated with a point contact.
In the following sections the results of the structural and geometrical characterization of the uniaxially cold compacted powder particles are presented.

3.2.1 Structural activity

The structural activity is the enhancement of diffusivity due to the presence of a high dislocation density in the material after cold compaction and due to its increase at the initial stage of sintering, according to the self activation mechanisms. The measure of the dislocation density in the interparticle contact region and in the growing neck is not easy. In order to pursue this objective, direct and indirect measure methods were used which were described in Chapter III.

3.2.1.1 *Dilatometric data analysis*

As shown in previous section, the evolution of the diffusion coefficient during the isothermal holding is obtained from the dilatometric curve; it may be used to obtain the evolution of dislocation density during the isothermal holding, through Equation (2.10), that expresses the relationship between the dislocation density and the effective diffusion coefficient. The results are shown in Figure (4.17).

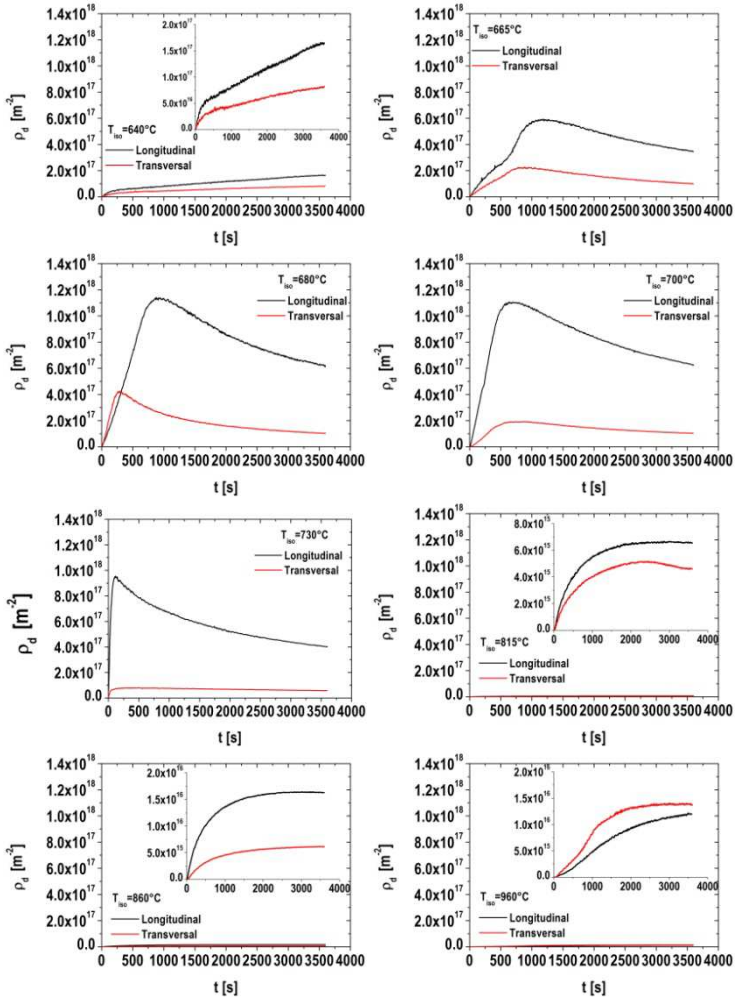

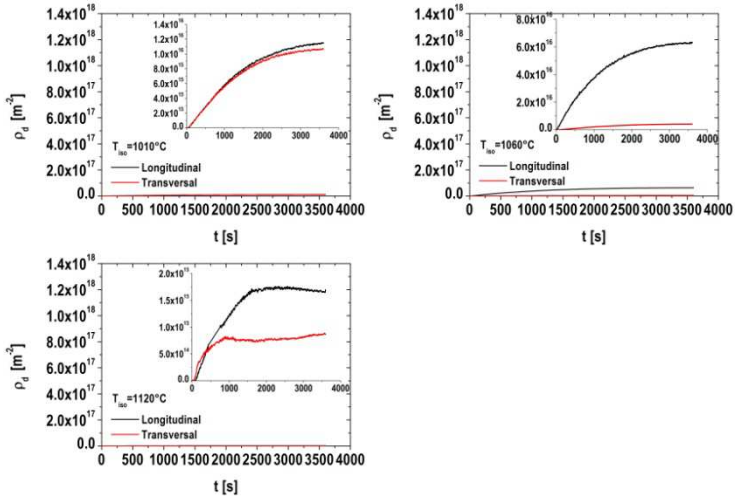

Figure IV - 17. Dislocation density along the two direction obtained with Equation (2.10).

As in the case of the diffusion coefficient, different trends in correspondence of the three temperature ranges can be observed. For temperatures below T_C the dislocations density displays a maximum, in paramagnetic field these increase until reach a plateau and smaller densities, whereas in austenitic field temperature ranges it increases continuously, but with a much small intensity.

The representations in Figure (4.18) show a possible interpretation of how the temperature and the direction may influence the dislocation density evolution during the isothermal holding.

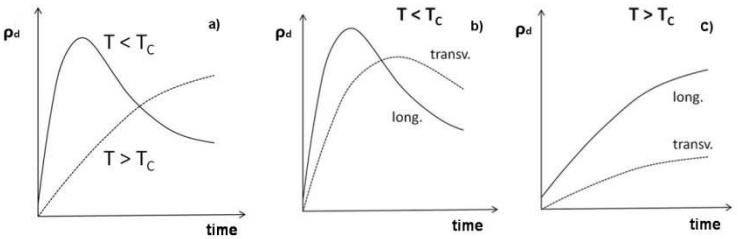

Figure 4.18. Schematic representation of dislocation density as a function of the isothermal holding time for: a) same direction at temperature below and above T_C, b) different directions in ferromagnetic field and c) different directions for temperature above T_C.

In Figure (4.18(a)), where the same direction is considered, for temperatures below Tc the dislocation density increases due to the self activation mechanism and reaches a maximum before decreasing due to recovery/recrystallization that are activated when a critical dislocation density is reached. This trend reminds the one obtained by Friedrich and Shatt [6]. For temperature above T_C dislocation density increases slowly, due to the smaller diffusion coefficient and the simultaneous presence of the recovery/recrystallization. Therefore, the maximum value of dislocation density is reached only in the cases with strong shrinkage. In Figure (4.18(b)) and Figure (4.18(c)) is represented how the density of dislocation changes along different directions at the same temperature (below or above T_C). For the transversal direction at temperature below T_C the maximum dislocation density is reached later and it is lower than for the longitudinal direction, due to the less deformation along this direction promoted by cold compaction.

The effect of the temperature on the dislocation density can be observed in Figure (4.19) where its maximum and mean values, calculated from the maximum and the mean D_{eff}, respectively, are reported as a function of temperature.

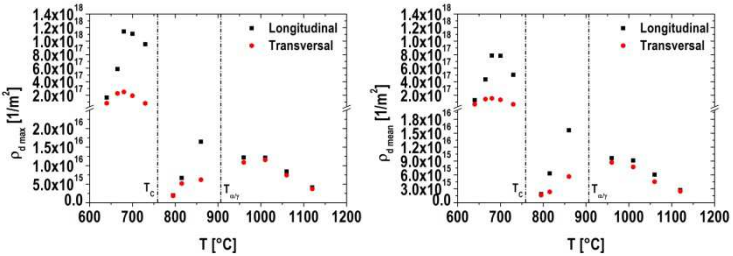

Figure 4.19. Maximum and mean dislocation density versus the temperature of isothermal holding.

In the temperature range of ferromagnetic iron the maximum and mean values of dislocation density increase until reaching a maximum at 680°C (approximately 100°C lower than T_C). Above this temperature both maximum and mean values start to decrease, probably due to the reduction of the critical dislocation density that causes the activation of recovery/recrystallization.

In the second temperature range (paramagnetic field) the maximum and mean dislocation density are initially two order of magnitude smaller than in the ferromagnetic field, but they increase on increasing temperature. In the austenitic field the dislocation density along the two directions is quite similar for almost all the temperatures but decreases with the increase in temperature.

In Figure (4.20) the ratio between the transversal and longitudinal mean and maximum values of dislocation density is reported.

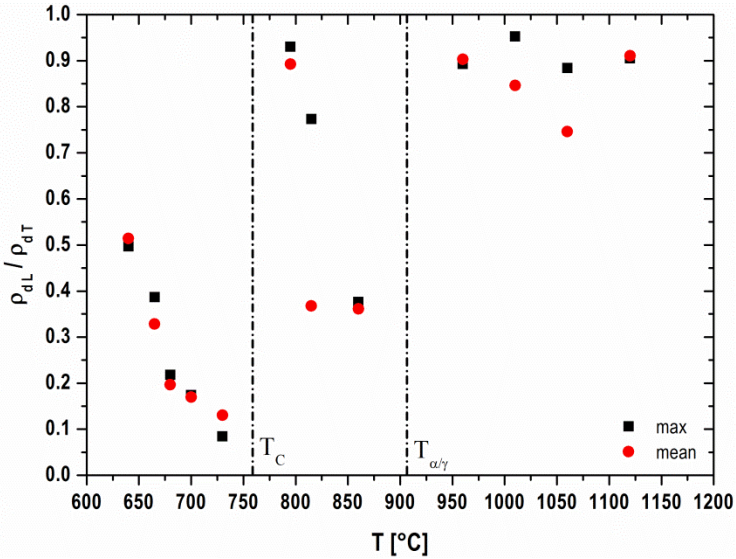

Figure 4.20. Ratio between the two diffusivities along the transversal and longitudinal directions.

Only in the austenitic field the concentration of defects is near to isotropy. This is due to the recrystallization during the phase transformation which has removed the most of the defects. This is confirmed by the previous results obtained studying the thermal expansion during the heating ramps. From these results an attempt was made to create a model with a physical meaning that can explain the evolution of dislocation density during isothermal holding, alternative to Equation (4.2).

3.2.1.1.1 Model with physical meaning

The diffusivity model represented by Equation (4.2) does not have in its structure the explicit reference to the contribution of the different mechanisms that are active during the sintering: self activation and recovery/recrystallization. A new equation was developed to describe the variation of the dislocation density during the isothermal holding which is directly correlated to the diffusivity.

For the different physical phenomena the time depending equations present in literature were used:

- ✓ Self-activation: the dislocation density increases proportionally to the square root of the time.

$$\rho(t) = b\sqrt{t} \tag{4.7}$$

- ✓ Recovery: for materials that show a high stacking fault energy, as in the case of iron, the dislocation climb enhances recovery. For the recovery due to dislocation climb the kinetic can be expressed as:

$$\frac{1}{\rho(t)} - \frac{1}{\rho_0} = ct \tag{4.8}$$

Where c and b are constants and ρ_0 is the dislocation density at the beginning of the isothermal holding, that is the results of both the deformation due to the prior cold compaction and the dislocations generated by sintering during the heating ramp.
Using these two kinetic correlations a model that describes the variation of dislocation density was obtained:

$$\begin{cases} \rho(t) = \dfrac{1}{\dfrac{1}{\rho_0 + b\sqrt{t}}} & (t < t_1 \,\&\, t < t_2) \quad \text{(a)} \\ \rho(t) = \dfrac{1}{\dfrac{1}{\rho_0 + b\sqrt{t}} + c(t - t_2)} & (t < t_1 \,\&\, t > t_2) \quad \text{(b)} \\ \rho(t) = \dfrac{1}{\dfrac{1}{\rho_0 + b\sqrt{t_1}} + c(t - t_2)} & (t > t_1 \,\&\, t > t_2) \quad \text{(c)} \end{cases} \tag{4.9}$$

Where t_1 is the time after which the self-activation contribution disappears, and t_2 is the time where the recovery is activated.
The equation (a) describes the kinetic when only the self-activation and the consequent increase in dislocation are present, the equation (b) represents the situation when both the mechanisms are activated, in (c) the self-activation reached the saturation and the recovery causes the decrease of dislocation density.
The model interpolates the experimental data with a good approximation but the parameters show an unstable (scattered) trend in the different temperature ranges; their values are reported in Table (4.6).

Longitudinal					
T [°C]	**ρ_0 [m^{-2}]**	**b**	**c**	**t1 [s]**	**t2 [s]**
640	$1.10 \cdot 10^{14}$	$2.67 \cdot 10^{15}$	--	3600	3600
665	$3.78 \cdot 10^{14}$	$1.53 \cdot 10^{16}$	$5.47 \cdot 10^{-22}$	1368	1569
680	$2.35 \cdot 10^{15}$	$3.41 \cdot 10^{16}$	$3.01 \cdot 10^{-22}$	1054	1138
700	$1.69 \cdot 10^{14}$	$4.15 \cdot 10^{16}$	$2.51 \cdot 10^{-22}$	783	667
730	$5.37 \cdot 10^{16}$	$9.30 \cdot 10^{16}$	$4.29 \cdot 10^{-22}$	87	89
795	$4.73 \cdot 10^{13}$	$7.38 \cdot 10^{13}$	$1.04 \cdot 10^{-19}$	3600	0
815	$1.74 \cdot 10^{13}$	$1.85 \cdot 10^{14}$	$1.82 \cdot 10^{-20}$	3600	146
860	$3.08 \cdot 10^{13}$	$4.66 \cdot 10^{14}$	$7.31 \cdot 10^{-21}$	3600	6
960	$2.89 \cdot 10^{13}$	$2.26 \cdot 10^{14}$	$3.42 \cdot 10^{-21}$	3600	0
1010	$2.11 \cdot 10^{13}$	$1.88 \cdot 10^{14}$	$9.82 \cdot 10^{-21}$	3600	3059
1060	$5.26 \cdot 10^{13}$	$1.57 \cdot 10^{14}$	$1.69 \cdot 10^{-21}$	3600	2462
1120	$1.32 \cdot 10^{13}$	$3.90 \cdot 10^{13}$	$1.07 \cdot 10^{-19}$	3600	1882
Transversal					
T [°C]	**ρ_0 [m^{-2}]**	**b**	**c**	**t1 [s]**	**t2 [s]**
640	$4.63 \cdot 10^{15}$	$1.28 \cdot 10^{15}$	--	3600	3600
665	$8.79 \cdot 10^{13}$	$6.98 \cdot 10^{15}$	$2.11 \cdot 10^{-21}$	954	1196
680	$2.18 \cdot 10^{15}$	$2.29 \cdot 10^{16}$	$2.31 \cdot 10^{-21}$	320	343
700	$2.24 \cdot 10^{14}$	$6.87 \cdot 10^{15}$	$1.72 \cdot 10^{-21}$	769	980
730	$5.22 \cdot 10^{15}$	$7.00 \cdot 10^{15}$	$1.51 \cdot 10^{-21}$	105	832
795	$6.18 \cdot 10^{13}$	$9.09 \cdot 10^{13}$	$1.37 \cdot 10^{-20}$	1254	2667
815	$3.82 \cdot 10^{13}$	$1.24 \cdot 10^{14}$	$2.43 \cdot 10^{-20}$	2478	1152
860	$1.34 \cdot 10^{12}$	$1.39 \cdot 10^{14}$	$1.74 \cdot 10^{-20}$	3600	1079
960	$1.08 \cdot 10^{12}$	$2.82 \cdot 10^{14}$	$9.33 \cdot 10^{-21}$	3600	2200
1010	$4.17 \cdot 10^{12}$	$2.1 \cdot 10^{14}$	$2.43 \cdot 10^{-21}$	3600	0
1060	$5.34 \cdot 10^{12}$	$7.26 \cdot 10^{13}$	$3.76 \cdot 10^{-95}$	3218	0
1120	$1.29 \cdot 10^{13}$	$2.67 \cdot 10^{13}$	$1.49 \cdot 10^{-94}$	853	0

Table 4.6. parameters ρ_0, b, c, t_1, t_2 of Equations (4.9) at the different temperature and for the two directions

The only exception is the parameter b that shows in almost linear correlation as shown in Figure (4.21).

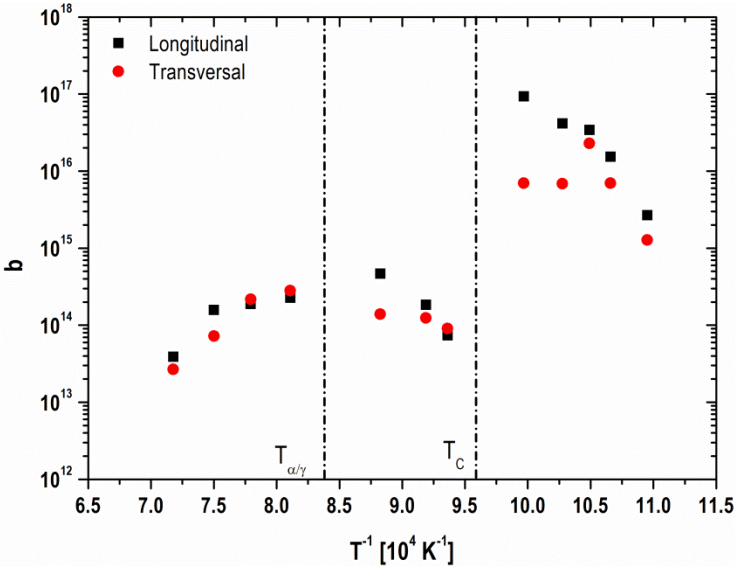

Figure 4.21. Parameters b of Equation (4.19) versus $10^4/T$

In the ferromagnetic field the parameter b is greater than in the other temperature ranges; below T_C it increases with the temperature; in the paramagnetic field its value is lower but still increases with the temperature; in the austenitic field b shows an opposite trend and starts to decrease with the increase in temperature. This trend can be explained because b is correlated to the mechanisms of the self-activation of the diffusion and is higher where the diffusion mechanism is active (approaching to Tc) and decreases when there are changes in the material magnetic and structural proprieties. The slope in the austenitic field is opposite to the others two, this shows how the influence of the structural activity is smaller after the phase transformation and decreases with the reorganization of the material lattice.

As shown in Figure (4.16) the parameter b shows a linear correlation in the three temperature ranges, therefore the previous model may be completed by the following Equation (4.10) to describe the parameter as a function of the temperature:

$$\log b = m_b T + q_b \qquad (4.10)$$

where T is the temperature in Celsius; the values of m_b and q_b for the three temperature ranges are reported in Table (4.7).

Parameters	Ferromagnetic		Paramagnetic		Austenite	
	Long	Transv	Long	Transv	Long	Transv
m_b	0.0162	0.0064	0.0117	0.0026	-0.0032	-0.067
q_b	5.292	11.409	4.600	11.965	17.611	20.994

Table 4.7. Parameters for Equation (4.10)

The values of ρ_0 in function of the temperature along the two direction are shown in Figure (4.22).

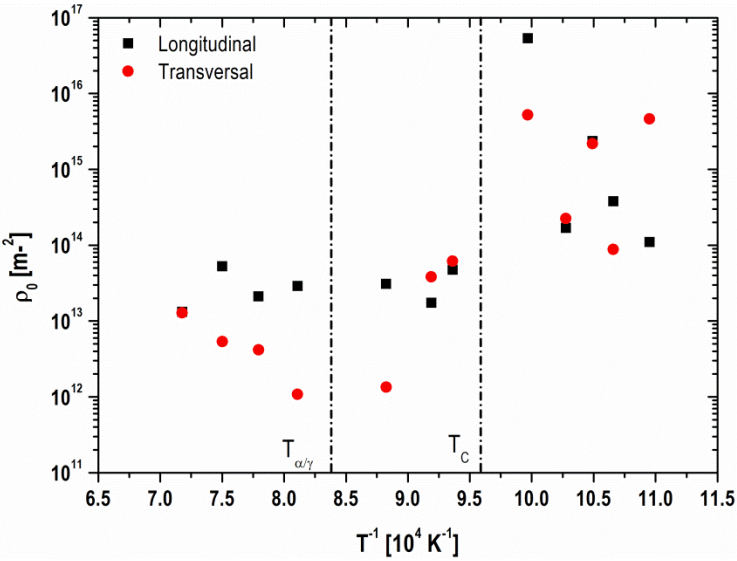

Figure 4.22. Parameter ρ_0 of Equation (4.19) versus 10^4/T

The dislocation density at the beginning of the isothermal holding is greater in the ferromagnetic field than in the other two temperature ranges and increases with the temperature; on the contrary it decreases in the paramagnetic field. In the temperature ranges of the austenitic phase along the longitudinal direction ρ_0 seems constant, and for the transversal tends to increase until reaching the same values of the longitudinal direction at the maximum temperature.

This attempt is a good first step towards the build-in of a mathematical correlation that explicitly shows the contribution of the different mechanisms involved, but it needs some improvement because some of the parameters (especially those related to recrystallization) are very scattered in austenitic flied (Figure (4.23)). This is probably due to the uncertainty in many cases to determine its activation time (t_2).

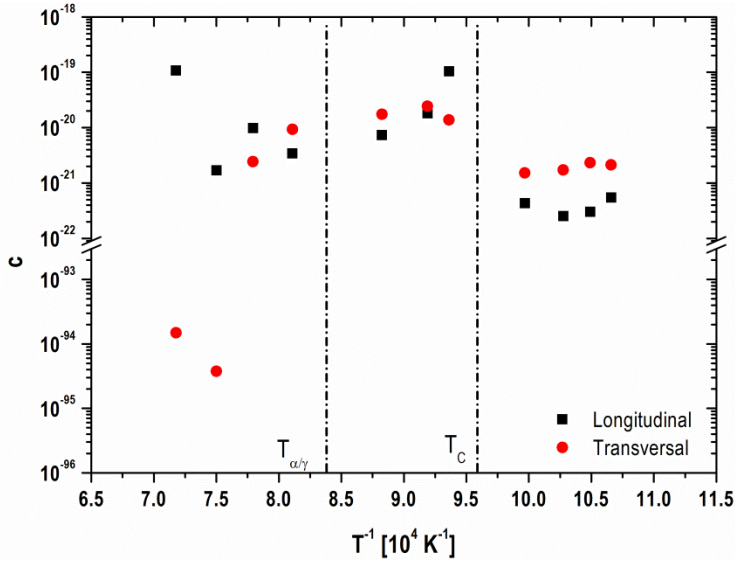

Figure 4.23. Parameter c of Equation (4.19) versus 10^4/T

The results obtained analyzing the dilatometric data are probably overestimated due to the impossibility to observe separately the contribute derived from the structural and geometrical activity. The dislocation densities obtained using this method are probably overestimated, but in order to obtain a validation, other experimental measurements through ISE method and EBSD analysis were used.

3.2.1.2 *Indentation size Effect*

As shown in Chapter III the ISE method correlates the hardness measurements at micro- and nano-scale to the dislocation density. In order to set up the experimental procedure and to verify if it is possible to distinguish the different deformation in the different areas of particles, copper spheres compacted in a die to simulate green components have been used. The sensibility of this method was studied compacting the spheres whit two different pressures: 156 MPa and 500 MPa .

In Figure (4.24) the deformation of the copper spheres due compaction is shown.

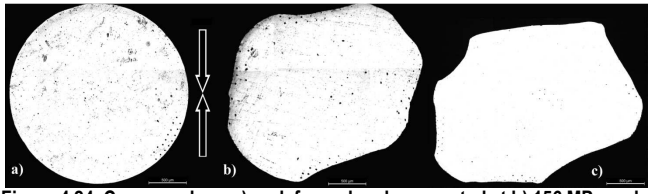

Figure 4.24. Copper sphere a) undeformed and compacted at b) 156 MPa and c) 500 MPa.

The presence of dislocations was observed directly using TEM analysis and SEM images of the surface of a sphere after being dipped in a specific etching.
Figure (4.25) shows the difference in material structure between the bulk and the surface of the spheres.

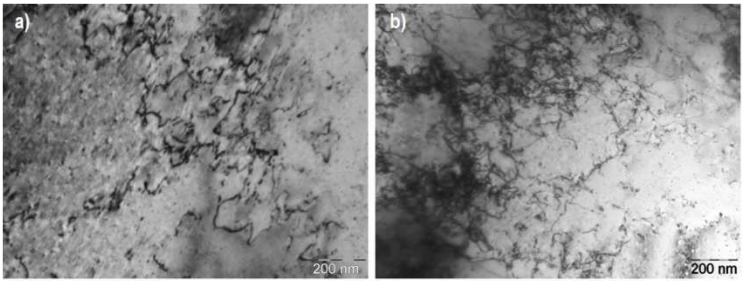

Figure 4.25 TEM image of a) surface of sphere and b) contact area on surface.

In the contact area (Figure (4.25(b))) plastic deformation caused the generation and accumulation of dislocations; they appear roughly uniformly distributed with a slight tendency to form a cell structure, as typical of pure metals during dynamic recovery. The lattice in the bulk of the sphere (Figure (4.25(a))) shows the presence of dislocations due to the deformation but it is evident how these are much less than in the contact area.
Using SEM we observed directly the contact area on the surface of a sphere,. In Figure (4.26) SEM images of the etched contact zones of a sphere compacted at 196 MPa are reported.

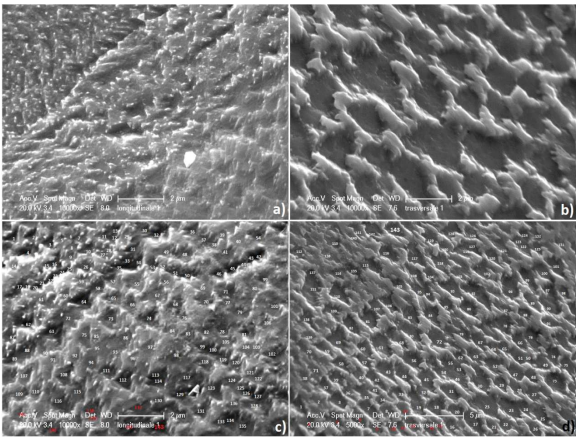

Fig.4.26 a) Etching pits in contact zone along the direction of compaction and b) in the transversal plane at 10000x. c) Count of pits for the direction parallel to the pressure at 10000x and d) transversal at 5000x.

Etching caused the formation of a large number of pits that may give a semiquantitative indication about the different deformation and dislocations density in the observed regions. Dislocation density is indeed proportional to the number of pits, but it does not exist a one to one correspondence between pits and dislocations. Nevertheless it is possible to recognize the differences between the etching morphology in the contact zones differently oriented respect to the compaction direction. Those oriented along the compaction direction (Figure (4.26(a))) show a higher density of the pits, which appear almost overlapped. In the contact zones oriented perpendicularly to the compaction direction (Figure (4.26(b))), pits are more distinct and deep than in the other ones.

A semiquantitative measure of the dislocation density is obtained using Equation (4.11):

$$\rho_d = \frac{n}{A} \tag{4.11}$$

where n is the number of pits and A is the area of the region. The number of pits n was determined from the SEM images, as shown in Figures (4.19(c)) and (4.19(d)), and the area of the region analysed was measured by an image analysis software (ImageJ®). Different images were analysed, and ρ_d resulted $(9.8\pm3.5)\times10^{11}$ m^{-2} in the compaction direction and $(4.9\pm3.2)\times10^{11}$ m^{-2} in the transversal one. The hypothesis of a different dislocation density in the contact zones depending on their

orientation with respect to the compaction direction is semiquantitatively confirmed. The last experimental analysis utilized was the ISE method; the microindentation hardness at three different loads (0.2N, 0.1N and 0.05N). The indentation depths were plotted and fitted using Equation (4.12)

$$\left(\frac{H}{H_0}\right)^2 = 1 + \frac{h^*}{h} \qquad (4.12)$$

In Figure (4.27) the fit of the Vickers microhardness data collected on the undeformed and deformed at 196 MPa spheres is shown.

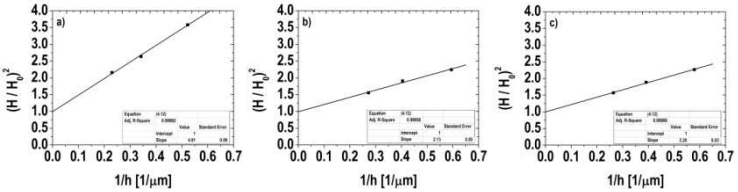

Figure 4.27. Fitting with Equation (4.13) of the data obtained from the surface a) for undeformed spheres. b) and c) for compacted sphere at 196 MPa respectively for the contact zone along the longitudinal (x) and transversal (y) direction.

From the interpolation of the experimental points, the parameter *h** was calculated which, used in Equation (3.15), gives the value of ρ_s that corresponds to the density of dislocations.

The results are reported in Table (4.8): h* and dislocation density are listed for the copper spheres after compaction at 196 MPa and prior to compaction (undeformed).

	Compacted at 196 MPa		Undeformed	Increase	
	x	y	Surface	x	y
h* [μm]	2.12	2.19	4.90		
ρ_s [10^{11}/m^2]	6.58	6.37	2.84	132%	124%

Table 4.8. Dislocation density obtained using Equation (3.15) for contact areas in the compact plane (x) and parallel to the compaction direction (y).

The dislocation density is increased by less than one order of magnitude after compaction. The dislocation density is slightly higher in the contact zone in the

compaction plane than along the compaction direction. The increase in the dislocation density is given by:

$$\text{increase} = \frac{(\rho_S)_{def} - (\rho_S)_{undef}}{(\rho_S)_{undef}} \qquad (4.13)$$

The difference between the two directions is rather small.
The same procedure was applied for the spheres deformed at 500 MPa and in Figure (4.28) the microhardness data fit for the calculation of h* is shown.

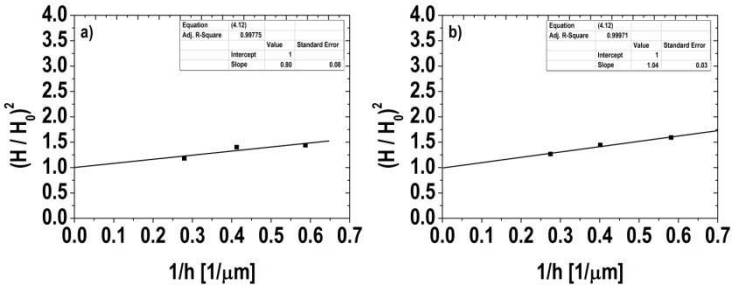

Figure 4.28. Fitting with Equation (4.13) of the data obtained from the surface for compacted sphere at 500 MPa respectively for the contact zone in compact plane (a) and parallel to the compaction direction (b).

In Table (4.9) the value of h* and the dislocation density for the sphere compacted at 500 MPa are reported.

	Compacted at 196 MPa		Undeformed	Increase	
	x	y	Surface	x	y
h* [μm]	0.81	1.04	4.90		
ρ_s [$10^{14}/m^2$]	1.72	1.34	$2.84 \cdot 10^{-3}$	506%	372%

Table 4.9. Dislocation density obtained using Equation (2.32) for contact areas in the compact plane (x) and parallel to the compaction direction (y).

The dislocation density introduced in the spheres at 500 MPa is higher than at 196 MPa, and the increase due to compaction is still less than one order of magnitude. The increment is still higher for the contacts in compaction plane than for the contacts parallel to the compaction, and their difference results increased with respect to that calculated at the lower compaction pressure, as it might be expected.

These results confirmed the capability of ISE method to measure the dislocation density in the material and its capacity to recognize the different deformation in the different area. The next step consists in applying the ISE method to a real cold compacted component that, how explained in the Chapter III, shows some critical aspects in the collection of hardness data.

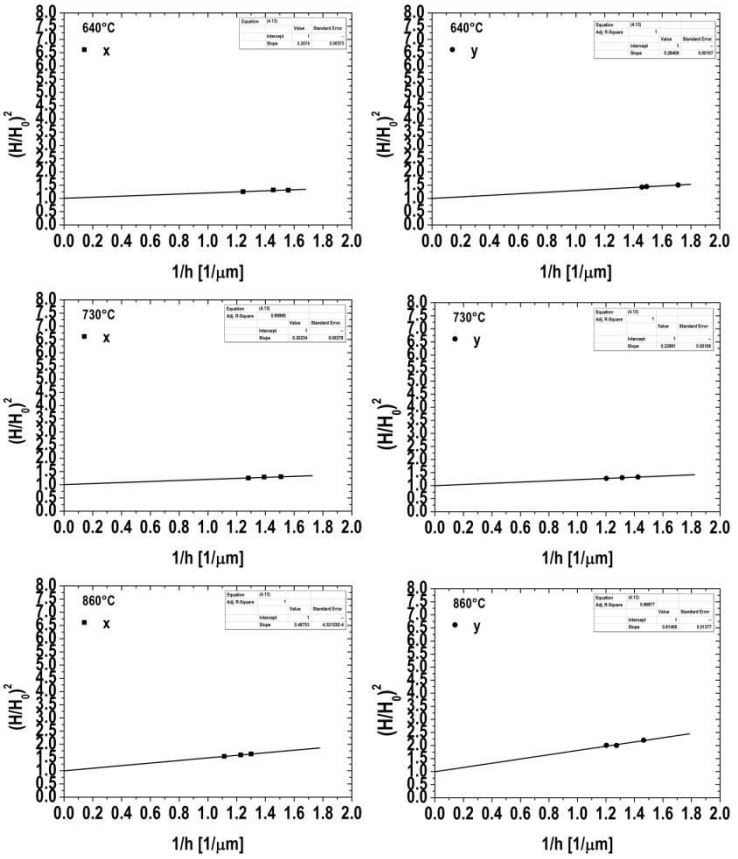

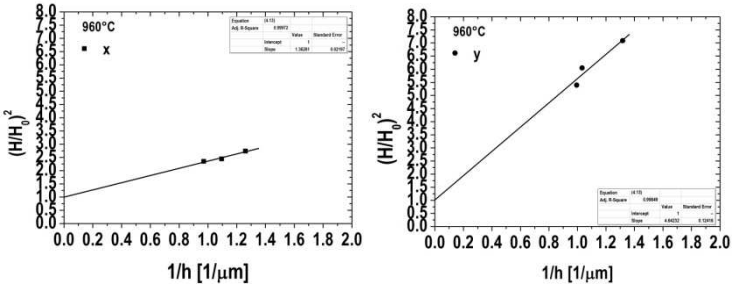

Figure 4.29. Fitting with Equation (4.12) for the data obtained from the real compacted samples sintered at 640°C, 730°C, 860°C and 960°C, for contact areas in compaction plane (x) and parallel to the compacting direction (y).

In Table (4.10) the values of h* and the dislocation density at the contact areas between the powder particles in real compacted components are reported.

		Contact	
		x	y
T=640°C	h* [μm]	0.21	0.29
	ρ_s [10^{15}/m^2]	11.7	8.26
T=730°C	h* [μm]	0.20	0.23
	ρ_s [10^{15}/m^2]	12.0	10.6
T=860°C	h* [μm]	0.49	0.81
	ρ_s [10^{15}/m^2]	4.98	2.98
T=960°C	h* [μm]	1.36	4.64
	ρ_s [10^{15}/m^2]	1.78	0.61

Table 4.10. Dislocation density obtained using Equation (2.32) for contact areas in the compact plane (x) and parallel to the compaction direction (y).

The dislocation density calculated using ISE is higher on contact areas perpendicular to the direction of the compaction than in the contact areas that are parallel to the compaction, as shown by Figure (4.30).

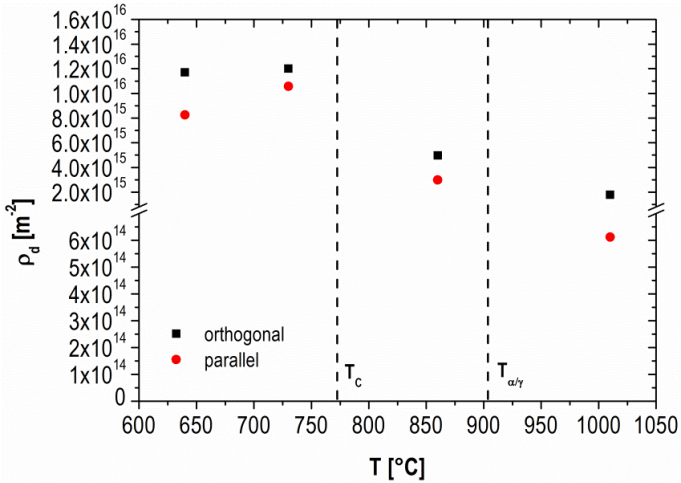

Figure 4.30 Dislocation density measured for the contact parallel (y) and orthogonal (x) to the direction of the compaction.

As for the values obtained from the dilatometric data, dislocation density increases on approaching T_C and decreases of one order of magnitude in the paramagnetic and austenitic field.

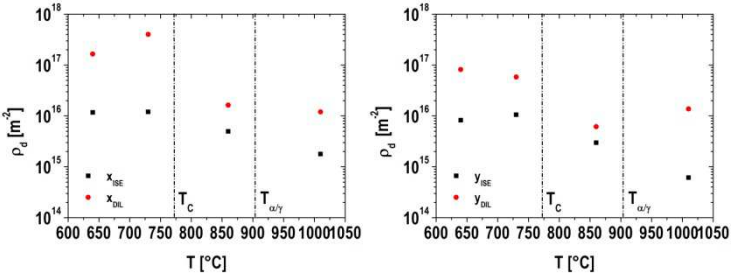

Figure 4.31. Comparisons between the dislocation density obtained from the dilatometry data and from the ISE method.

In Figure (4.31) the dislocation density measured using the ISE method is compared to an average dislocation density obtained from the analysis of the effective diffusion coefficient at the end of isothermal holding through the Equation (2.10). The values obtained from ISE method are smaller than those obtained using the dilatometry

because due to the uncertain position of the section in the powder particles that is analysed. Nano-hardness measurements are in fact an average value of deformed and undeformed material. However it can be appreciated how the ISE values follow the same trend of the dilatometric values as a function of temperature.

3.2.1.3 *EBSD*

From the post-processing of the EBSD images, the value of GNDs for the contact orthogonal (x or longitudinal) and parallel (y or transversal) to the compaction direction were obtained. The result are reported in Table (4.11).

	GND density		Ratio
T (°C)	ρ_{dx} (1/m^2)	ρ_{dy} (1/m^2)	ρ_{dx} / ρ_{dy}
640	1.04 10^{15}	1.02 10^{15}	1.01
730	1.06 10^{15}	1.02 10^{15}	1.04
860	8.88 10^{14}	8.61 10^{14}	1.03
1010	9.29 10^{14}	8.41 10^{14}	1.10

Table (4.11) Dislocation density measured from EBSD images.

The result obtained shows differences between the two directions and also values of the density smaller than those obtained with the others two methods. However, considering that the SSD cannot be detected through the EBS scanning, these results can be considered comparable with the measurements made with the ISE method.

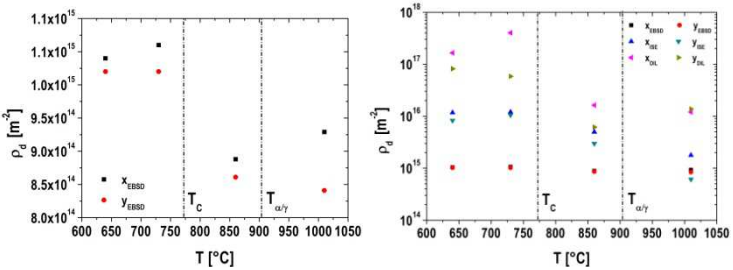

Figure 4.32. a) Dislocation densities measured with EBSD analysis, b) comparison of dislocation densities measured with the different methods.

As shown in Figure (4.32), despite the different order of magnitude, the values obtained with the various methods show the same trend, with higher dislocation

density before T_C and a reduction up to one order of magnitude in paramagnetic and austenitic field.

3.2.2 Geometrical activity

The geometry and arrangement of the powder particles in the porous body, and the different extension of the interparticle contacts are aspects that in the classical theory of sintering are not taken into account to describe and model the kinetic of sintering shrinkage. On the contrary they are considered in the continuum mechanics models, i.e. the external neck radius is correlated to the sintering stress, the driving force of sintering.
The contact area between the deformed particles is not a negligible aspect of the sintering kinetic. This area represents the sources of atoms diffusing toward the neck; the larger its extension, the more intense is the flux of atoms. The contribution of this geometrical characteristic to anisotropy of shrinkage is expected to dominate over that given by dislocations in austenite, because strain hardening promoted by cold compaction should be mostly eliminated by the alpha/gamma phase transformation.

3.2.2.1 *External neck radius*

As shown in Chapter II, the sintering stress, that represents the driving force of the sintering mechanisms, can be expressed through different relationships: as difference in external stress, pressure or concentration. These are represented by Equations (2.2), (2.3) and (2.4) that are related to the geometry of the contact between two particles, and principally to the surface curvature, through the external neck radius (r). The measurements of the external neck radius were performed on the sample sintered at lower temperature (640°C) in order to observe well resolved neck profile, that it is not possible in a green component. Such a profile permits to define the circumference corresponding to the neck surface arc with a good precision, resulting in an error corresponding to the lateral resolution of SEM (typically in the range 10-60 nm [10]). The permanence in temperature, even if very short, can cause some neck growth and change of neck morphology; therefore the data collected cannot represent perfectly the green state. However this slight neck growth does not affect this study, that is focused on a comparison between the neck external radius corresponding to the contact parallel (transversal contact) and to the contact perpendicular (longitudinal contact) to the compaction direction. Since the neck growth and the change in its morphology at this temperature is quite low and occurs with the same probability in the different directions, it is still possible obtain a comparison for samples sintered at the same temperature. The results are reported in Figure (4.33). .

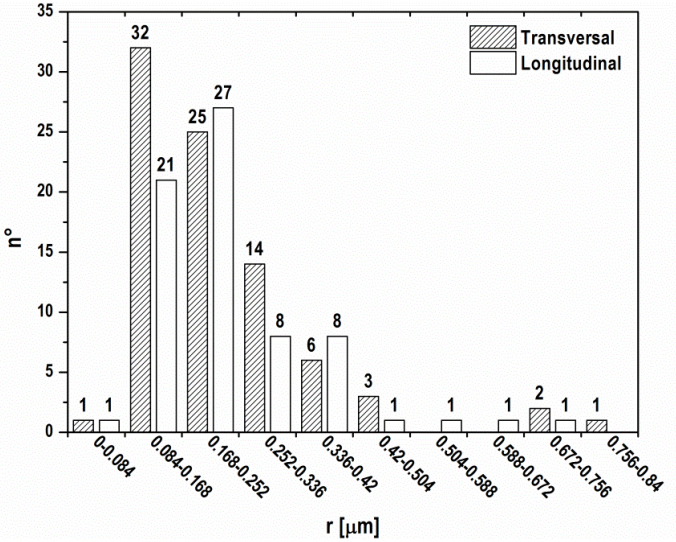

Figure 4.33. Distribution of external neck radius for the contact disposed along (Transversal) and orthogonal (Longitudinal) the direction of compaction.

The medians of the two distributions of the neck radius are reported in Table (4.12)

Direction	r [μm]
Longitudinal	0.20
Transversal	0.19

Table 4.12. Medians of neck radius in the two directions.

The external neck radius in the two directions is almost the same; this result shows that the driving force is not involved in the anisotropy of dimensional change of the green components.

3.2.2.2 ***Internal neck radius***

The internal neck radius or contact area between the deformed particles is connected with the flux of diffusing atoms, since it represents their source. It is reasonable to think that the more extended is a contact, the higher is the corresponding quantity of atoms involved in the diffusion and shrinkage is consequently increasing.

In this study the contacts where measured as explained in Chapter III obtaining the distribution of the radius X of the contacts disposed perpendicular to the compaction direction and parallel to it that is shown in Figure (4.34).

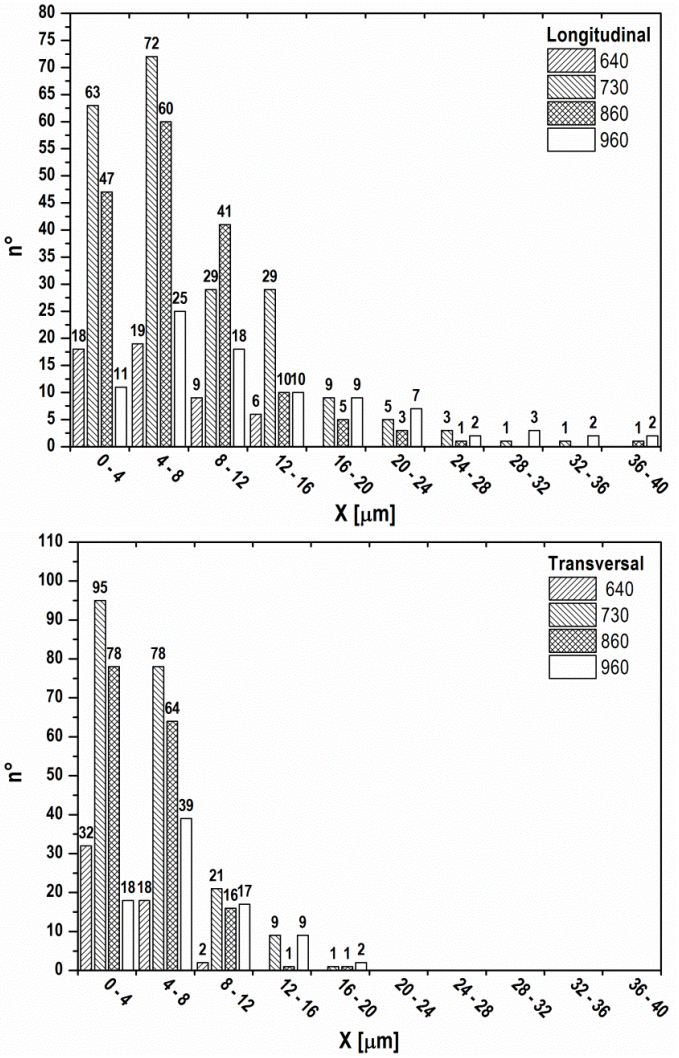

Figure 4.34. Histogram of the distribution of the length of the contacts perpendicular to the direction of the compaction (Longitudinal) and parallel to this (Transversal).

From these distributions it is clear that the contacts perpendicular to the compaction direction are larger than those parallel to it. Furthermore their extension increases with the sintering temperature .

3.2.2.2.1 Correction coefficients

As explained in Chapter III correction coefficients were obtained using a cluster of sphere in bcc arrangement to model the green body.

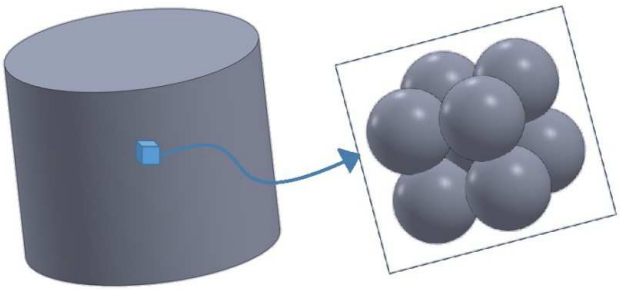

Figure 4.35. A bcc cluster of sphere used for simulate the powder compact arrangements.

The model was designed with dimensions shown in figure 4.36.

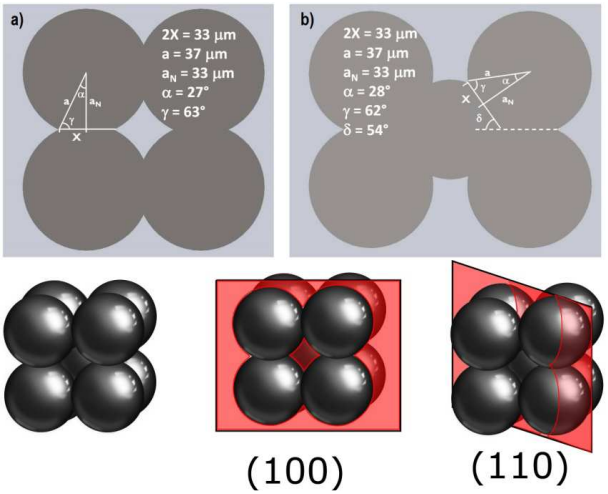

Figure 4.36. True dimensions of the necks: a) longitudinal and of the transversal from the section along the plan (100) through the centres of the edge spheres; b) inclined from the section along the plan (110) through the centre of the central sphere.

These clusters were sectioned using a plane, which simulates the metallographic section and for any translation (Figure (4.36(a))) and rotation (Figure (4.36(b))) of this plane the resulting contacts and geometrical parameters were measured.

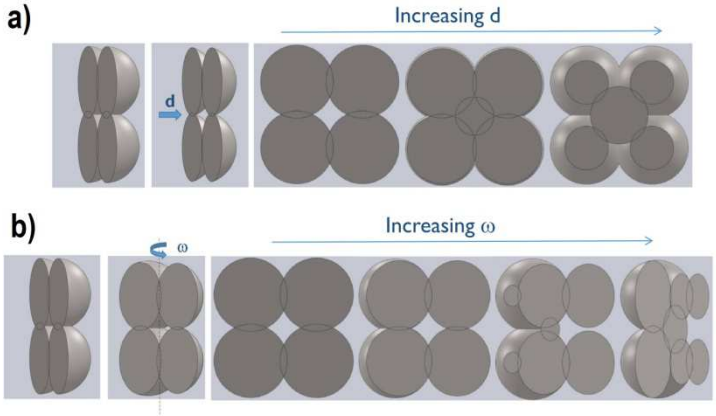

Figure 4.37. Representation of the evolution of the necks and geometry of particles in function of the translation or rotation of the sectioning plane.

In Figure (4.37) the progressive changes of the geometry of the particles and contacts due the translation and rotation of the "metallographic" plane is shown. From the case of the rotation around the vertical and horizontal axis, in a range of a certain angle of inclination, "deceptive" configuration of the contact were founded (Figure (4.38)).

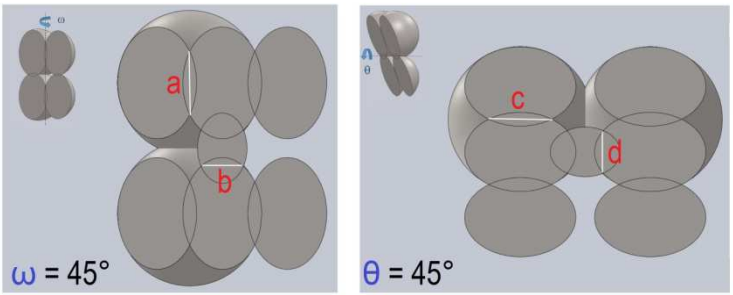

Figure 4.38. Representation of the "deceptive" configuration of the contact for the rotation around the vertical (ω) and the horizontal (θ) axis.

The contact (a) is a transversal neck that is orthogonal to the other detected when the rotation angle ω is between 31° and 64°C, the contacts (b) and (d) are inclined but with a 1.1% of probability they can be detected respectively as longitudinal and transversal. The contact (c) is a transversal contact that is detected as longitudinal when the rotation angle θ is between 31° and 64°.
These deceptive configuration can be neglected for different reasons. The contact (a) remains a transversal neck so it does not introduces a significant error in the analysis. Conversely the contact (c) that is actually transversal is detected as longitudinal, this introduces a significant error, but in practice it can be neglected; through the preparation of the samples, both inclinations (ω and θ) obtained are smaller than 5°. For the case of the inclined contacts (b) and (d) the probability that their "distortion" can occur is quite low (1.1%).
The correction factors were obtained from the average of the ratio between the real dimension and the value measured in the possible cases of distortion of the neck. The results are reported in Table (4.13):

neck	X	δ	a	a_N	α	γ
longitudinal	1,42	1,00	1,24	1,33	1,25	1,09
transversal	1,47	1,00	1,30	1,37	1,33	1,12
inclined	1,66	1,26	1,38	1,54	1,59	1,43
mean	1,52	1,09	1,31	1,41	1,39	1,22

Table 4.13. Correction factors for the geometry parameters in function of the different type of neck.

The corrected medians $\overline{X}_L$ and $\overline{X}_T$ are reported in Table (4.14):

T [°C]	X_L [μm]	X_T [μm]	$\overline{X}_L$ [μm]	$\overline{X}_T$ [μm]]	$\overline{X}_L \backslash \overline{X}_T$
640	5.84	3.37	8.87	5.13	1.73
730	5.94	4.22	9.02	6.41	1.41
860	6.17	4.07	9.37	6.19	1.51
960	9.72	6.55	14.78	9.96	1.48

Table 4.14. Median value for the distribution of contacts length (X_L and X_T), median modified using the corrective factors and ratio between the two median.

From the values reported in Table (4.14) it is confirmed what highlighted above, the contact length X_L is greater than the X_T and both grow on increasing the temperature. The ratio between these lengths seems to be in the range between 1.4 and 1.7; even if the internal radii increase with sintering, they tend to maintain a constant ratio.

In this work the highest temperatures were not analyzed with the image analysis due to the difficulties in recognizing the powder particles that compose the porous body and in obtaining an accurate measure of these geometrical parameters (Figure (4.39)).

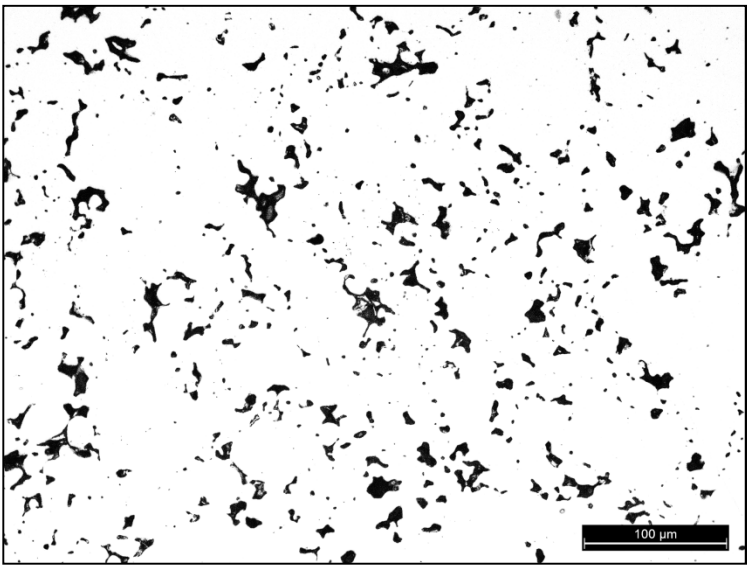

Figure 4.39. Optical image of a sample sintered at 1120°C

As shown in Figure (4.39) it is not easy to distinguish the particles from each other. Only for the smaller particles it is possible to recognize their shape.

3.2.2.3 *Coordination number*

From the image analysis and the division of contribution of the contact areas along the two directions using Equation (3.4), the two distributions shown in Figure (4.40) were obtained.

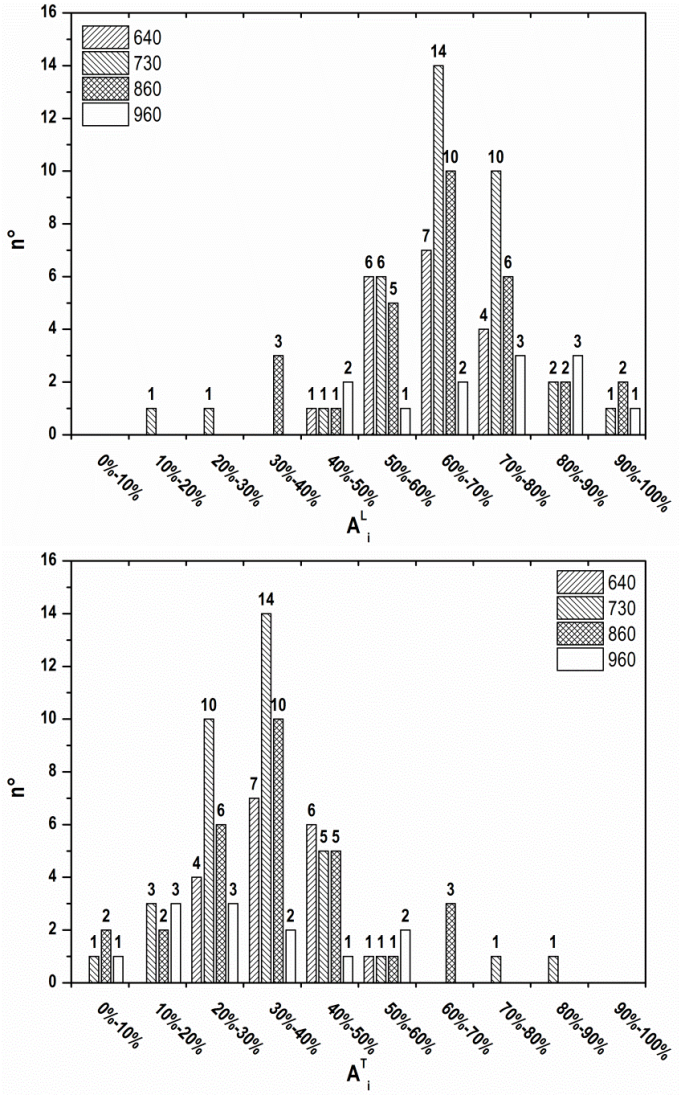

Figure 4.40. Distribution of the fraction area for the contacts in the compaction plane (L) and parallel to the compaction direction (T), at the different temperatures of isothermal holding.

From these distributions, the median values that used to divide the coordination number along the two directions were obtained: they are reported in table 4.15.

	640 [°C]	730 [°C]	860 [°C]	960 [°C]
L [%]	62.71	68.55	63.73	73.64
T [%]	37.29	31.14	36.27	26.36

Table 4.15. Median f the fraction area distributions for the contacts in the compaction plane (L) and parallel to the compaction direction (T), at the different temperatures of isothermal holding.

From all the measurements the mean number of contacts for each temperature was obtained, and using the data reported in Table (4.15) a corrected number of coordination for the principal directions has been obtained.

	640 [°C]	730 [°C]	860 [°C]	960 [°C]
n°	9.04	7.81	6.11	6.09
$n°_L$	5.67	5.35	3.89	4.48
$n°_T$	3.37	2.43	2.22	1.60

Table 4.16. Value of total coordination number and "corrected" coordination number along contacts in the compaction plane ($n°_L$) and parallel to the compaction direction ($n°_T$).

The coordination number decreases with increasing sintering temperature, only for the last two temperatures the coordination number is almost the same. However for all the temperatures the coordination number corrected for the contacts along the direction orthogonal to the compaction (L) is greater than for the direction parallel to the compaction (T) .

3.3 Continuum mechanics model

The continuum mechanics, unlike the classical approach, models the kinetic of sintering considering the influence derived from the geometry of the particle and of the porosity that composes the porous body.
In this part a micromechanical model will be described, which was developed starting from the Olevsky work [11] based on the continuum mechanics theory. In this work this model was adapted in order to consider the case of volume diffusion instead of the grain boundary diffusion. Consequently the first important change regards the geometry of the model that from a 2-D case becomes a 3-D case, as shown in Figure (4.41).

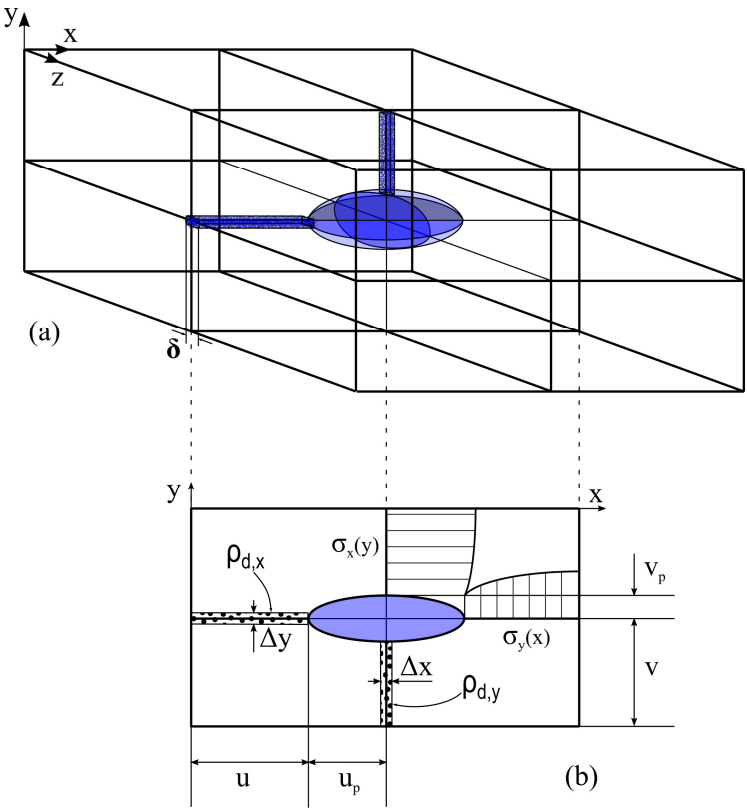

Figure 4.41. Model geometry, u and v are the semi-contacts length between the particles, u_p and v_p are the semi axis of the pore, and δ the grain boundary thickness.

The powder particles that compose the sinter body are represented as parallelepipeds oriented and simply packed with the different extension of the contact length parallel (v) and transversal (u=w) to the compaction direction. The pores are located at the junctions between the particles and have an oblate ellipsoid shape due to the same deformation in the compaction plane with the semi axes v_p, and $u_p=w_p$. This representation of the porous body permits to develop the model using the different geometrical parameters of powder particles flattened by cold compaction that influences the shrinkage kinetics.

As values of semi-contact between the particles the experimental data collected for the internal neck radius ($\overline{X}_L$ and $\overline{X}_T$) reported in the Section 4.2 were used.

To obtain a measurement of the geometrical parameters of the pores represented as ellipses, the same SEM images used for the previously described characterizations were analyzed through ImageJ® as shown in Figure (4.42):

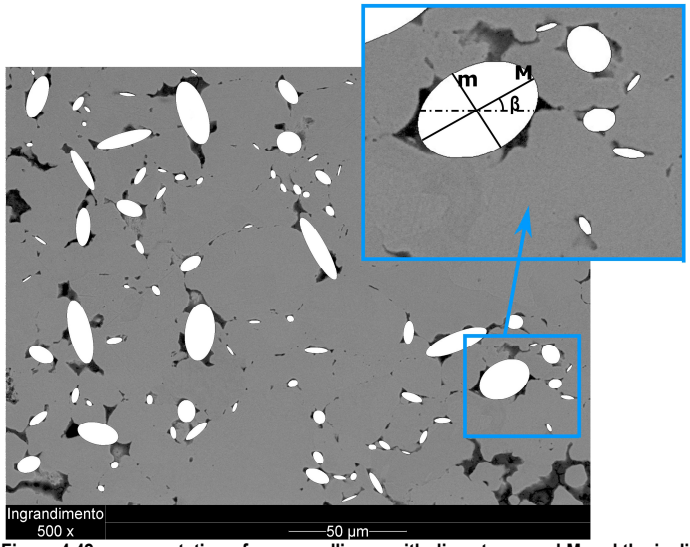

Figure 4.42. representation of pore as ellipses with diameter m and M and the inclination β.

This software allows to represent every single pore as an ellipse with an equivalent area comparable with that of the pore. The other geometrical parameter are the principal diameter (m and M) of the ellipse and the inclination (β) of the major axis with the horizontal direction of picture. Using these data the projection of the radii along the principal directions (v_p and u_p) at the different temperatures were obtained through a simple trigonometric correlation (Equation(4.14)).

$$\begin{cases} 0° \le \beta < 45° \rightarrow u_p = \dfrac{M}{2}\cos(\beta); \;\; v_p = m\sin(\beta) \\ 45° \le \beta < 135° \rightarrow u_p = \dfrac{m}{2}\left|\cos(\beta)\right|; \;\; v_p = M\sin(\beta) \\ 135° \le \beta < 180° \rightarrow u_p = \dfrac{M}{2}\left|\cos(\beta)\right|; \;\; v_p = m\sin(\beta) \end{cases} \qquad (4.14)$$

For the two radii the distributions shown in Figure (4.43) were obtained.

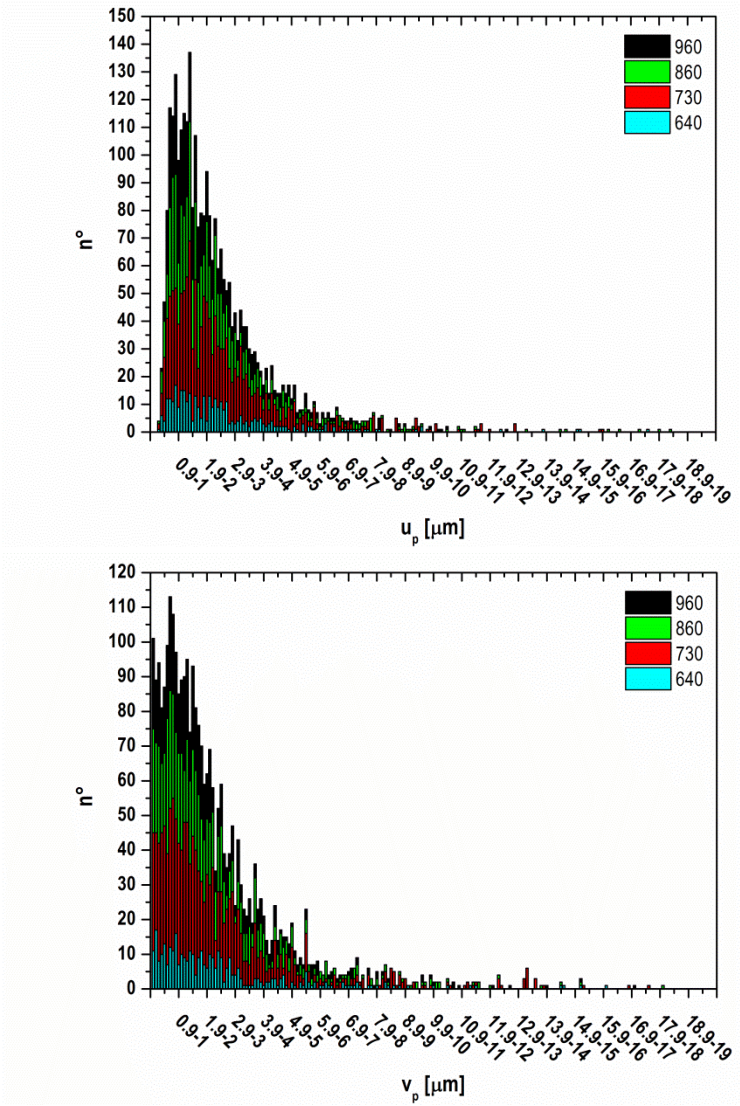

Figure 4.43. Distribution of u_p and v_p at different temperature.

Form these distributions the median values for u_p and v_p at various temperatures were calculated as reported in Table (4.17):

	640 [°C]	730 [°c]	860 [°C]	960 [°C]
u_p [μm]	2.02	1.96	1.79	1.57
v_p [μm]	1.73	1.59	1.56	1.49

Table 4.17. Median of u_p and v_p at different temperature

u_p is greater than v_p and both decrease with temperature. Moreover, at the highest temperature the difference between the two radii is quite low.
The radii of curvature of ellipse r_u, r_v and r_w were obtained using the Equation (4.15):

$$\begin{cases} r_u = \dfrac{{v_p}^2}{u_p} = \dfrac{{v_p}^2}{w_p} = r_w \\ r_v = \dfrac{{u_p}^2}{v_p} = \dfrac{{w_p}^2}{v_p} \end{cases} \tag{4.15}$$

An estimation of the surface area of this oblate ellipsoid (S_p) is obtained using the Equation (4.16):

$$S_p \approx 2\pi \cdot \left({u_p}^2 + {v_p}^2 \frac{\tanh^{-1}\left(\sin\left(\cos^{-1}\left(v_p / u_p\right)\right)\right)}{\sin\left(\cos^{-1}\left(v_p / u_p\right)\right)} \right) \tag{4.16}$$

The shrinkage kinetic along the two principal directions longitudinal (y) and transversal (x) were modelled following the Johnson work [12] and the stresses at the particles contact boundaries due the presence of the particles junction can be expressed as in Equation (4.17)

$$\begin{cases} \sigma_x = b_{1x} y^2 + b_{2x} y + b_{3x} \\ \sigma_y = b_{1y} x^2 + b_{2y} x + b_{3y} \end{cases} \tag{4.17}$$

The boundary conditions that these equations should satisfy considering the geometry of the problem are:

- the balance of the total particles contact force with the pore free surface tension at the junction:

$$\int_o^u \sigma_y dx = -\gamma_{sp} \sin\frac{\Phi}{2} \tag{4.18}$$

Where γ_{sp} is the free surface tension and ϕ is the dihedral angle that can be defined using the relation:

$$\gamma_{ss} = 2\gamma_s \cos\left(\Phi/2\right) \tag{4.19}$$

where γ_{ss} is the grain boundary energy.

- The normal stress at the pore surface (x=u):

$$\sigma_y(u) = \frac{\gamma_{sp}}{r_u} \tag{4.20}$$

- Symmetry of the stress distribution:

$$\nabla\sigma_y(0) = \frac{\nabla\sigma_y}{\partial x}(x=0) = 0 \tag{4.21}$$

These Equations are referring to the y direction; similar relationship exist along the x direction.
Using these boundary conditions, the coefficients, b_{1y}, b_{2y} and b_{3y} for the stresses distribution are calculated using Equation (4.22):

$$\begin{cases} b_{1y} = \dfrac{3\gamma_s}{2}\left[\dfrac{1}{u^2 r_u} - \dfrac{1}{u^3}\sin\left(\dfrac{\Phi}{2}\right)\right] \\ b_{2y} = 0 \\ b_{3y} = \gamma_s\left[\dfrac{3}{2u}\sin\left(\dfrac{\Phi}{2}\right) - \dfrac{1}{2r_u}\right] \end{cases} \tag{4.22}$$

The stress distribution for the particle contact in the compaction plane becomes:

$$\sigma_y = \frac{3\gamma_S}{2}\left\{\frac{1}{u^2}\left[\frac{1}{r_u}-\frac{1}{u}\sin\left(\frac{\Phi}{2}\right)\right]x^2+\left[\frac{1}{u}\sin\left(\frac{\Phi}{2}\right)-\frac{1}{3r_u}\right]\right\} \qquad (4.23)$$

For the particle contact parallel to the compaction direction the stress distribution is expresses by Equation (4.24).

$$\sigma_x = \frac{3\gamma_S}{2}\left\{\frac{1}{v^2}\left[\frac{1}{r_v}-\frac{1}{v}\sin\left(\frac{\Phi}{2}\right)\right]y^2+\left[\frac{1}{v}\sin\left(\frac{\Phi}{2}\right)-\frac{1}{3r_v}\right]\right\} \qquad (4.24)$$

Considering the mechanism of dislocation pipe diffusion the flux of matter can be expressed as:

$$\begin{cases} J_x^V = -\dfrac{D_{eff,x}}{kT\Omega}\dfrac{\partial\mu}{\partial x} \\ J_y^V = -\dfrac{D_{eff,y}}{kT\Omega}\dfrac{\partial\mu}{\partial y} \end{cases} \qquad (4.25)$$

Where $D_{eff,x}$ and $D_{eff,y}$ are the effective diffusion coefficient proportional to the dislocation density (Equation (2.10)) along the two principal directions, k is the Boltzmann's constant, T is the absolute temperature, Ω is the atomic volume, μ is the chemical potential that can be correlated to the stress through the Equation (4.26):

$$\begin{cases} \dfrac{\partial\mu}{\partial x} = -\Omega\dfrac{\partial\sigma_y}{\partial x} \\ \dfrac{\partial\mu}{\partial y} = -\Omega\dfrac{\partial\sigma_x}{\partial y} \end{cases} \qquad (4.26)$$

Using the Equations (4.23), (4.24), (4.25) and (4.26) the fluxes can be expressed with Equation (4.27):

$$\begin{cases} J_x^V = 3D_V\left(1+\pi r_p^2\rho_{d,x}\dfrac{D_p}{D_V}\right)\dfrac{1}{kT}\gamma_s\dfrac{1}{u}\left[\dfrac{1}{r_u}-\dfrac{1}{u}\sin\left(\dfrac{\Phi}{2}\right)\right] \\ J_y^V = 3D_V\left(1+\pi r_p^2\rho_{d,y}\dfrac{D_p}{D_V}\right)\dfrac{1}{kT}\gamma_s\dfrac{1}{v}\left[\dfrac{1}{r_v}-\dfrac{1}{v}\sin\left(\dfrac{\Phi}{2}\right)\right] \end{cases} \quad (4.27)$$

The fluxes are proportional to the change of the length of the contacts between the particles Δ_x and Δ_y:

$$\begin{cases} J_x^V(u) = -\dfrac{d(\Delta_y)}{dt}\dfrac{(u+u_p)}{\Omega(S_p/2)}\delta \\ J_y^V(v) = -\dfrac{d(\Delta_x)}{dt}\dfrac{(v+v_p)}{\Omega(S_p/2)}\delta \end{cases} \quad (4.28)$$

Where δ is the grain boundary thickness.
The strain rates along the directions x and y can expressed as function of the changing length of the contacts using Equation (4.29):

$$\begin{cases} \dot{\varepsilon}_x = \dfrac{d(\Delta_X)}{dt}\dfrac{1}{(v+v_p)} \\ \dot{\varepsilon}_y = \dfrac{d(\Delta y)}{dt}\dfrac{1}{(u+u_p)} \end{cases} \quad (4.29)$$

Using the Equations (4.27), (4.28) and (4.29) the shrinkage rate can be expresses as:

$$\begin{cases} \dot{\varepsilon}_x = -3\dfrac{D_V\left(1+\pi r_p^2\rho_y\dfrac{D_p}{D_V}\right)\Omega}{kT\delta}\gamma_s\dfrac{S_p/2}{(u+u_p)(v+v_p)}\dfrac{1}{v}\left[\dfrac{1}{r_v}-\dfrac{1}{v}\sin\left(\dfrac{\Phi}{2}\right)\right] \\ \dot{\varepsilon}_y = -3\dfrac{D_V\left(1+\pi r_p^2\rho_x\dfrac{D_p}{D_V}\right)\Omega}{kT\delta}\gamma_s\dfrac{S_p/2}{(v+v_p)(u+u_p)}\dfrac{1}{u}\left[\dfrac{1}{r_u}-\dfrac{1}{u}\sin\left(\dfrac{\Phi}{2}\right)\right] \end{cases} \quad (4.30)$$

This model expresses the shrinkage rate in the case of free sintering as a function of the geometry of powder particles and porosity and of the deformation of the material (dislocation density).
The average of the shrinkage rates during the isothermal holding of dilatometric analysis are reported in Table (4.18).

T [°C]	$\dot{\varepsilon}_x$ [1/s]	$\dot{\varepsilon}_y$ [1/s]
640	$-4.04\cdot10^{-5}$	$-5.31\cdot10^{-5}$
730	$-8.68\cdot10^{-5}$	$-1.65\cdot10^{-4}$
860	$-8.41\cdot10^{-5}$	$-1.23\cdot10^{-4}$
960	$-3.74\cdot10^{-5}$	$-3.54\cdot10^{-5}$

Table 4.18. Integral average of the shrinkage rates obtained from the isothermal shrinkage of the dilatometric analysis.

The values of the contact length along the principal directions and the semi-axes of the elliptic porosity come from the image analysis of SEM images. The other components of the model are experimental parameters (temperature), material constant as, boundary thickness (δ=0.5 nm), atomic volume ($\Omega=8.38\cdot10^{-30}$ m^3), surface tension (γs=2.5 N/m), pipe radius (r_p =0.5 nm) and dihedral angle ($\phi\approx157.5°$).
The volume and pipe diffusion coefficients at equilibrium are reported in Table (4.19) [1,13].

T [°C]	D_v [m^2/s]	D_p [m^2/s]
640	$1.09\cdot10^{-19}$	$1.63\cdot10^{-14}$
730	$6.99\cdot10^{-18}$	$1.74\cdot10^{-13}$
860	$7.77\cdot10^{-16}$	$2.72\cdot10^{-12}$
960	$2.71\cdot10^{-17}$	$6.56\cdot10^{-13}$

Table 4.19. Diffusivity at equilibrium for volume (D_v) and pipe diffusion (D_p).

Using those data in the Equation (4.30) the dislocation density at the different temperatures was derived, and compared with the ISE results in (Figure (4.44))

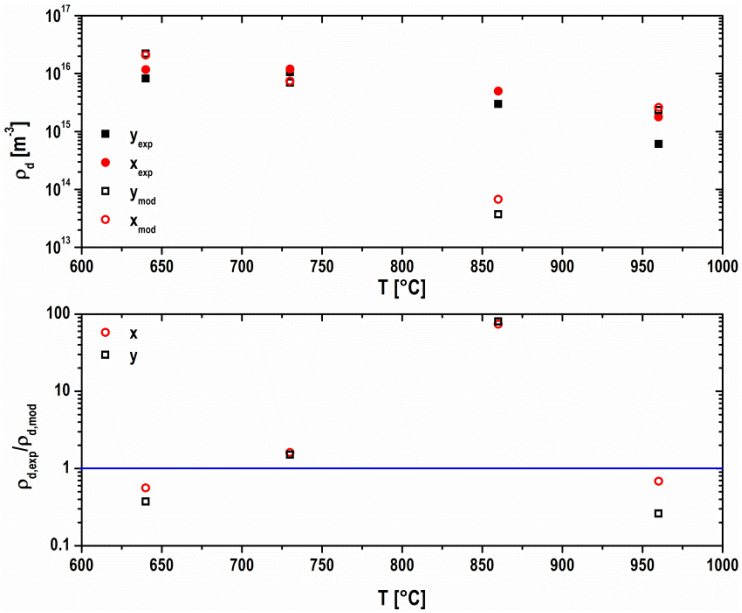

Figure 4.44. Comparisons between the dislocation density measured with the ISE method and that obtained with the model.

With the model it is possible to obtain the dislocation densities comparable to the experimental data with the only exception of the case of 860°C.

3.4 Effect of green density

3.4.1 Analysis of the dilatometric curves

In order to investigate the influence of green density on the kinetics of the sintering shrinkage along the two directions, the isothermal shrinkage of samples with a different green density of 6.5, 6.7, 6.9, 7.1 and 7.3 g/cm^3 was analyzed.
In Figure (4.45) the isothermal shrinkage, in absolute value, at 640°C and 1120°C along the two directions is shown.

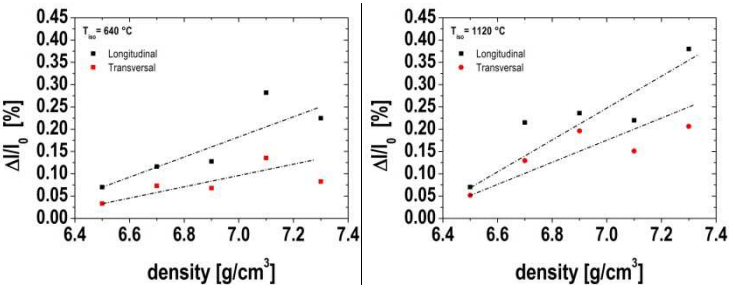

Figure 4.45. Total shrinkage along longitudinal and transversal direction in function of the green density for isothermal holding at 640°C and 1120°C.

Data do not depict an unambiguous dependence on green density. Nevertheless, a general increase of isothermal shrinkage on increasing green density may be argued. The ratio between the isothermal shrinkage along the longitudinal and the transversal directions can be used to evaluate its anisotropy. Results are reported in Figure (4.46) versus green density for both the temperatures.

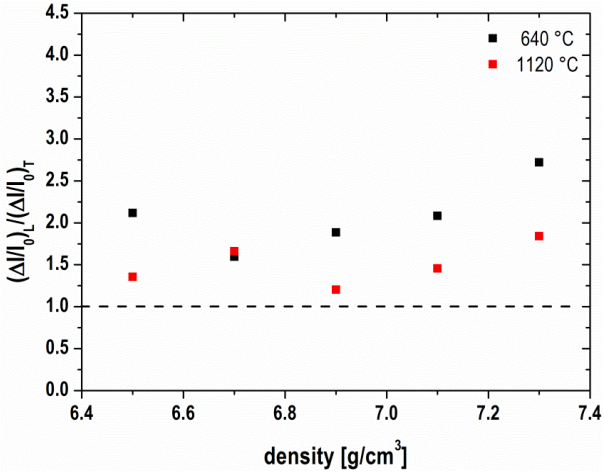

Figure 4.46. Ratio of total shrinkage along longitudinal and transversal direction in function of the green density for isothermal holding at 640°C and 1120°C.

The anisotropy at 640°C is greater than at 1120°C, confirming what observed and discussed in the previous section. On increasing green density, anisotropy tends to slightly decrease reaching a minimum at 6.9 g/cm^3; above this density anisotropy increases significantly, and tends to increase with green density. The conclusion about the real significance of the minimum will be drawn in the following.

The anisotropy developed during the heating step was studied through the comparisons between the theoretical expansion (thermal expansion) and the experimental dimensional change up to the austenitic transformation temperature (910°C).

The thermal expansion coefficients reported in Table (4.20) were used to calculate the theoretical expansion; they were obtained from mean values of the thermal contraction coefficient during the cooling ramps.

Temperature ranges [°C]	Thermal Expansion Coefficient [10^{-6} K^{-1}]
RT-200	14.0
200-400	16.5
400-910	17.0

Table 4.20. Theoretical expansion coefficient used for the comparison.

Figure (4.47) compares the theoretical expansion curve and the experimental curves, from which the results presented in Table (4.21) were calculated. The temperature interval is defined by the first datum collected by the dilatometry and by the austenite transformation start temperature.

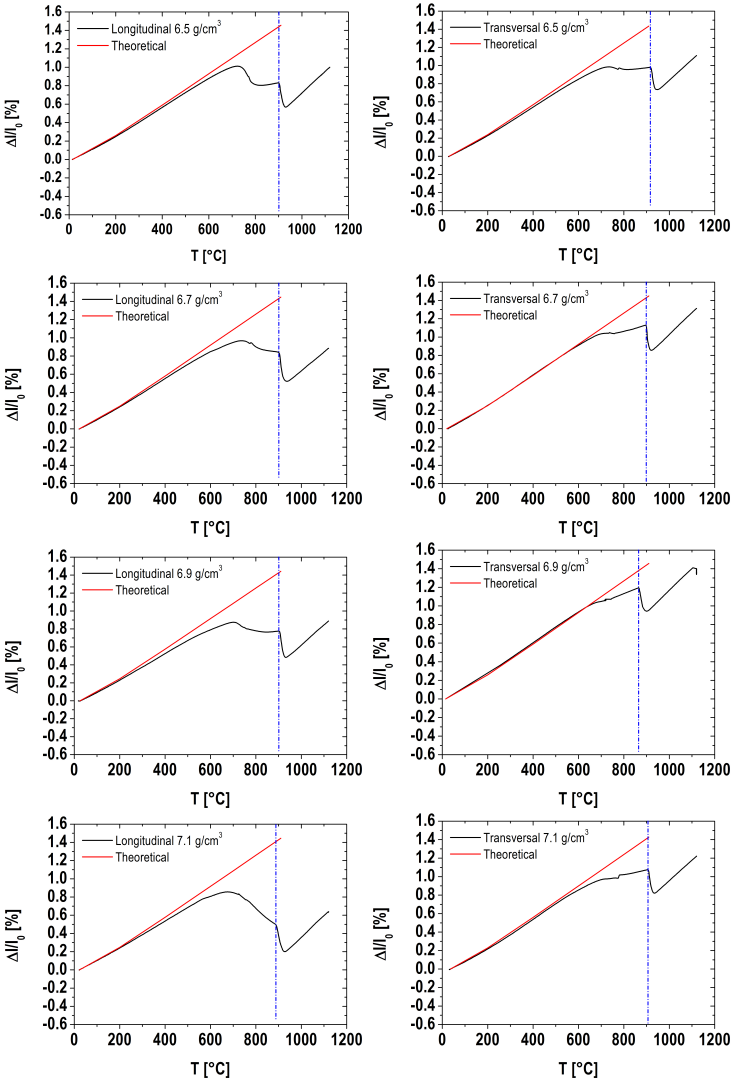

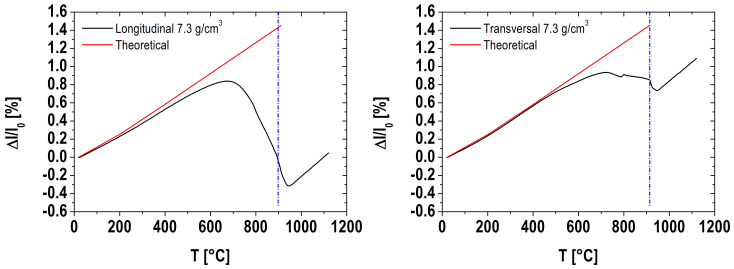

Figure 4.47. Comparison of theoretical thermal expansion and dimensional changes measured during the heating ramp.

Longitudinal					
density [g/cm^3]	T_{start} [°C]	$T_{\alpha/\gamma}$ [°C]	$\Delta l/l_{0\ exp}$ [%]	$\Delta l/l_{0\ theo}$ [%]	difference [%]
6.5	15	906	0.78	1.45	0.67
6.7	22	905	0.81	1.44	0.63
6.9	25	902	0.77	1.43	0.66
7.1	23	889	0.49	1.41	0.92
7.3	19	896	-0.02	1.43	1.45
Transversal					
density [g/cm^3]	T_{start} [°C]	$T_{\alpha/\gamma}$ [°C]	$\Delta l/l_{0\ exp}$ [%]	$\Delta l/l_{0\ theo}$ [%]	difference [%]
6.5	30	920	0.97	1.45	0.48
6.7	20	896	1.13	1.43	0.3
6.9	15	864	1.19	1.38	0.19
7.1	36	906	1.07	1.42	0.35
7.3	21	916	0.84	1.46	0.62

Table 4.21. Dimensional changes measured at $T_{\alpha/\gamma}$ and the theoretical expansion at the same temperature.

The anisothermal shrinkage is plotted in Figure (4.48) as a function of green density. I It is greater for longitudinal than for transversal direction.

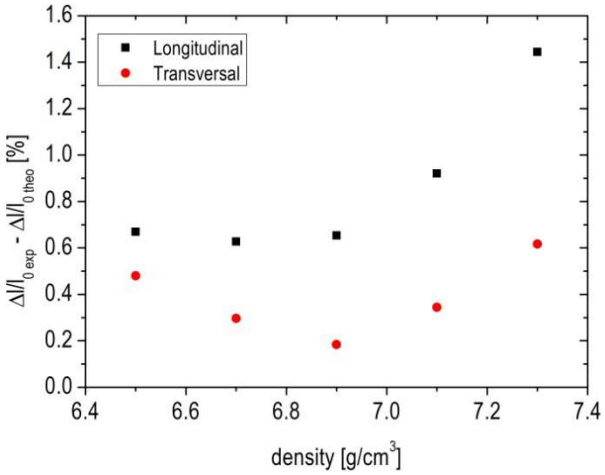

Figure 4.48. Difference between the theoretical and experimental thermal expansion at $T_{\alpha/\gamma}$ along the two directions.

The trend with green density still displays a minimum with a significant increase above 6.9 g/cm^3. Moreover, the difference between the two directions increases with the density. The transversal anisothermal shrinkage displays a minimum at 6.9 g/cm^3, while the longitudinal one is stable up to the same density, and then increases. This result may be explained as a combination of two effects: the decrease of driving force (related to the surface area) and the increase in the structural activity promoted by cold compaction, on increasing green density. Since the structural activity of the contacts responsible for transversal shrinkage is smaller than that of the longitudinal ones, due to the inhomogeneous deformation of the particles, the combination of the two effects leads to the minimum only in the transversal specimens.

The anisotropy of dimensional changes is still the result of the sum of the contributions from the different intensity of the diffusion mechanisms along the two directions during the heating ramp and during the isothermal holding. Figure (4.49) shows, as an example, that the difference between the longitudinal and the transversal curves at the beginning of isothermal holding at 1120°C is quite large, and is almost the same at the end of the isothermal holding.

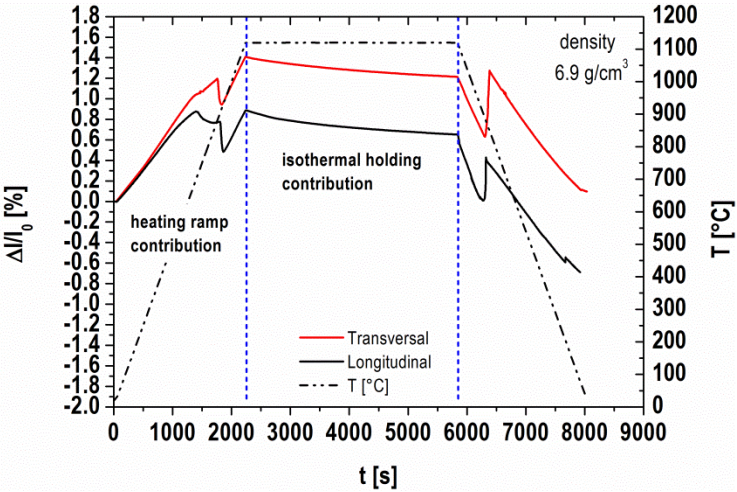

Figure 4.49. Division of dilatometric curve in two areas respectively where is present the contribution of anisotropy of the heating ramp and that of the isothermal holding.

The dimensional changes at the beginning and at the end of the isothermal holding are reported in Table (4.22).

	Tiso=640°C					
	Δl/l0 start			Δl/l0 end		
density	L [%]	T [%]	Δl/l0 L / Δl/l0 T	L [%]	T [%]	Δl/l0 L / Δl/l0 T
6.5	0.93	0.94	0.99	0.86	0.91	0.94
6.7	0.88	0.95	0.92	0.76	0.87	0.87
6.9	0.89	0.95	0.93	0.76	0.89	0.86
7.1	0.80	0.91	0.87	0.52	0.78	0.66
7.3	0.83	0.90	0.92	0.60	0.82	0.74

Table 4.22a. Dimensional changes measured at the beginning and end of isothermal holding at 640°C.

	T_{iso}=1120°C					
	$\Delta l/l_0$ start			$\Delta l/l_0$ end		
density	L [%]	T [%]	$\Delta l/l_{0\,L}$ / $\Delta l/l_{0\,T}$	L [%]	T [%]	$\Delta l/l_{0\,L}$ / $\Delta l/l_{0\,T}$
6.5	1.00	1.11	0.90	0.93	1.06	0.88
6.7	0.88	1.31	0.67	0.67	1.19	0.57
6.9	0.89	1.41	0.63	0.65	1.16	0.54
7.1	0.64	1.22	0.52	0.42	1.07	0.39
7.3	0.05	1.09	0.04	-0.33	0.88	-0.38

Table 4.22b. Dimensional changes measured at the beginning and end of isothermal holding at 1120°C.

Figure (4.50) shows the anisothermal shrinkage up to the various temperatures and the isotheral shrinkage at the same temperatures.

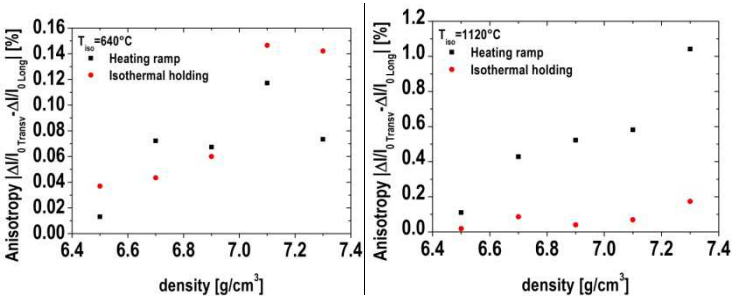

Figure 4.50. Anisotropy contribution of heating ramp and of isothermal holding.

At 640°C the contribution to anisotropy from the heating ramp is comparable to that of the isothermal holding, while for the tests at 1120°C the contribution of heating ramp is much higher than the isothermal holding. The figure shows that anisotropy of dimensional change increases with green density. The minimum observed in Figure (4.46) can therefore be due to the effect of small numbers on their ratio.
Table (4.24) compares the two contributions at the two temperatures.

	T_{iso}=640°C	
	Contribution to the anisotropy [%]	
density	heating ramp	isothermal holding
6.5	25.27	74.73
6.7	57.69	42.31
6.9	49.15	50.85
7.1	37.86	62.14
7.3	30.93	69.07

Table 4.24a. Percentage of the contribution of the heating ramp and isothermal holding for dilatometric test at 640°C.

	T_{iso}=1120°C	
	Contribution to the anisotropy [%]	
density	heating ramp	isothermal holding
6.5	80.76	19.24
6.7	74.85	25.15
6.9	84.25	15.75
7.1	78.21	21.79
7.3	69.54	30.46

Table 4.24b. Percentage of the contribution of the heating ramp and isothermal holding for dilatometric test at 1120°C.

As shown in Table (4.24), the contributions to the anisotropy that derive from the isothermal holding (42-75%) are greater than those derive from the heating ramp at 640°C, while for the isothermal holding at 1120°C the isothermal contributions to the anisotropy are at maximum 30.46% at the highest density. This shows how are the diffusion mechanisms active during the heating ramp for temperature below $T_{\alpha/\gamma}$ that have the greater influence on the anisotropy of dimensional changes, while over $T_{\alpha/\gamma}$ the defectiveness are eliminated by the recrystallization during the austenitic transformation, therefore the shrinkage and the material flow in the austenitic field are influenced by the geometrical activity.

3.4.1.1 *Shrinkage kinetic*

The time depending effective diffusion coefficient D_{eff}, that derives from the contribution of dislocation pipe diffusion to bulk diffusion, was calculated using Equation (4.1).

For the isothermal holding at 640°C D_{eff} as a function of green density is shown in Figure (4.51).

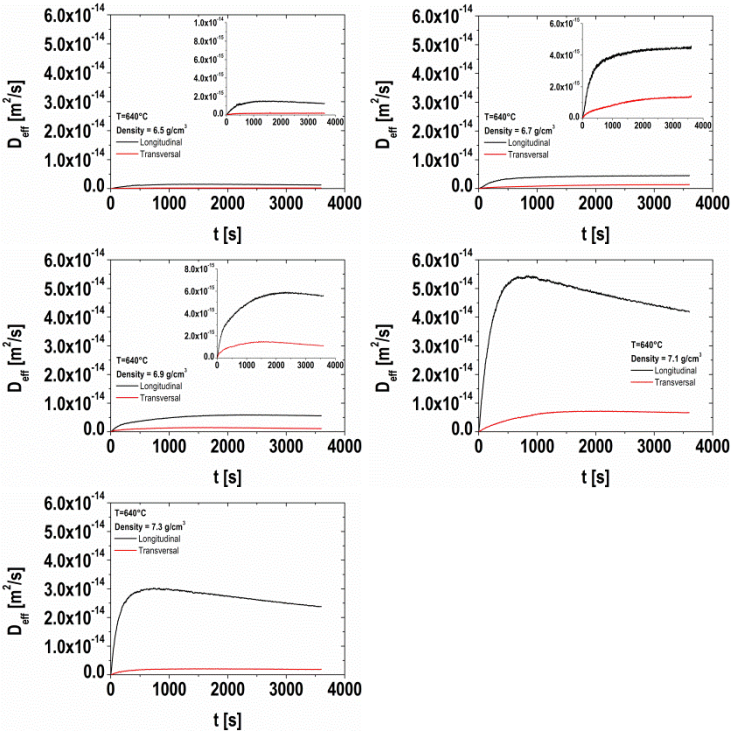

Figure 4.51. Effective diffusion coefficient for isothermal sintering at 640°C.

The effect of green density is affected by the isothermal shrinkage measured, that are shown in figure (4.45). D_{eff} increases with green density up to a maximum for 7.1 g/cm^3, and decreases at the highest density.

The effective diffusion coefficient was determined also for the isothermal holding at 1120°C, and the results are shown in Figure (4.52).

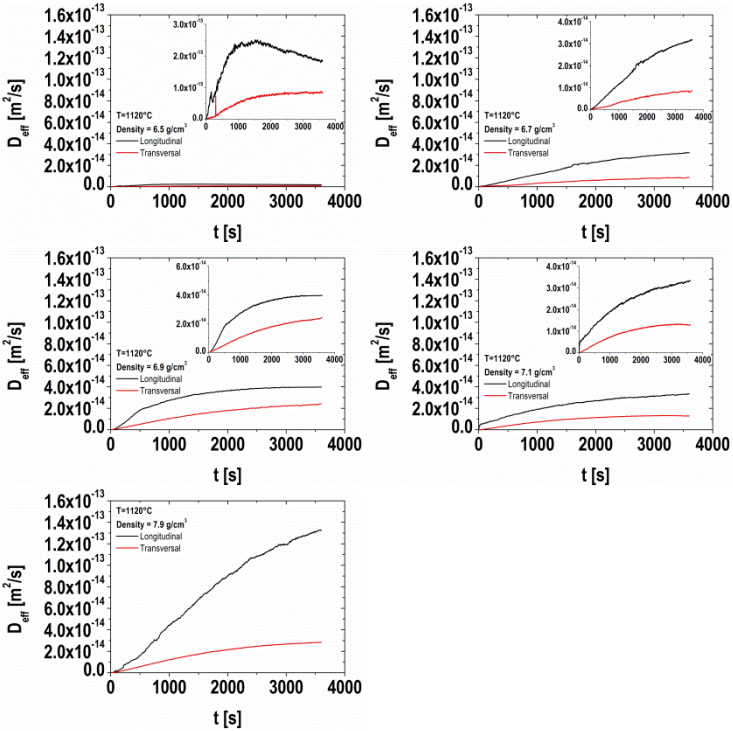

Figure 4.52. Effective diffusion coefficient for the dilatometric analysis at 1120°C.

At this temperature the effect of green density is more clear than at 640°C; D_{eff} increases with the increasing of green density. Along the longitudinal direction, D_{eff} shows the maximum only in the less dense sample, while in the other cases it increases monotonically. For the transversal specimens, the monotonic increase with time is much less pronounced.

Despite the D_{eff} calculated is greater for the isothermal holding at higher temperature, the real enhancement of diffusivity due to the structural activity has to be calculated as the ratio between the effective diffusivity and the diffusion coefficient at the equilibrium (Table (4.1)); results are shown in Figure (4.53), with reference to the maximum D_{eff} measured in all the experiments.

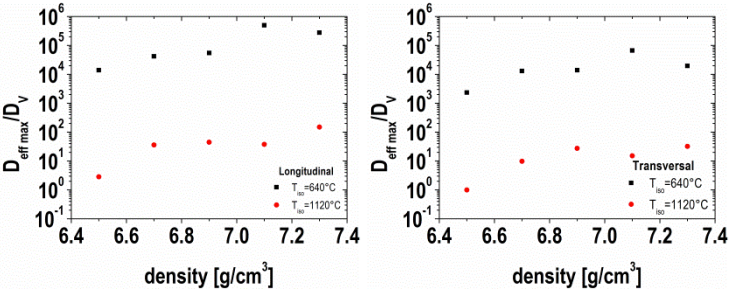

Figure 4.53. Ratio between effective diffusion coefficient and volume diffusion coefficient at the equilibrium for the dilatometric analysis at 640°C and 1120°C

The greater enhancement of the volume diffusion coefficient due to the contribute of the dislocation pipe diffusion is observed at the lowest temperature: it is approximately 4-6 order of magnitude for the longitudinal direction and 3-5 for the transversal direction. They both increase with green density. At the highest temperature the effective diffusion coefficient has the same order of magnitude of D_v for the lowest green density for both the directions, and increases with green density up to two orders of magnitude for the longitudinal direction and one for the transversal. The greater enhancement at the lower temperature is due to the presence of a high dislocation density and consequently a greater contribute to the diffusion derive from the dislocation pipe diffusion mechanisms. In the austenitic field where the defectiveness introduced through the compaction were cancelled by the recrystallization, the contribution of the dislocations pipe diffusion is absent or quite limited.

3.4.1.2 *Diffusivity Equation*

The Equation (4.2) was used for interpolate the correlation between the effective diffusion coefficient and time shown in Figure (4.51) and Figure (4.52). An example of fitting is reported in Figure (4.54).

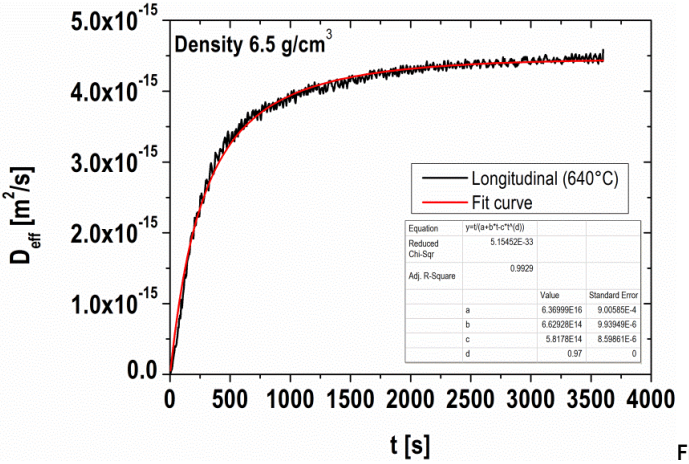

Figure 4.54. Example of fitting of experimental curve, Longitudinal direction with isothermal holding at 640°C for component with 6.5 g/cm³ of density.

The parameters a, b and c of Equation (4.2) obtained for the different densities and for the two isothermal temperatures are reported in Table (4.25)

	T_{iso}=640°C					
	Longitudinal			Transversal		
d [g/cm³]	a	b	c	a	b	c
6.5	3.49 10^{17}	9.08 10^{15}	1.07 10^{16}	1.01 10^{18}	1.20 10^{16}	9.00 10^{15}
6.7	6.37 10^{16}	6.63 10^{14}	5.82 10^{14}	6.06 10^{17}	1.03 10^{15}	6.03 10^{14}
6.9	6.65 10^{16}	6.16 10^{14}	5.93 10^{14}	3.62 10^{17}	9.65 10^{15}	1.14 10^{16}
7.1	5.30 10^{15}	2.41 10^{14}	2.79 10^{14}	1.25 10^{17}	2.07 10^{15}	2.50 10^{15}
7.3	5.79 10^{15}	3.21 10^{14}	3.60 10^{14}	1.41 10^{17}	3.74 10^{15}	4.17 10^{15}
	T_{iso}=1120°C					
	Longitudinal			Transversal		
d [g/cm³]	a	b	c	a	b	c
6.5	4.78 10^{17}	1.18 10^{16}	1.46 10^{16}	2.46 10^{18}	2.71 10^{16}	3.40 10^{16}
6.7	1.15 10^{17}	7.74 10^{14}	9.90 10^{14}	4.32 10^{17}	2.76 10^{15}	3.54 10^{15}
6.9	2.86 10^{16}	2.53 10^{14}	3.01 10^{14}	1.07 10^{17}	5.93 10^{14}	7.42 10^{14}
7.1	2.97 10^{16}	2.86 10^{13}	8.17 10^{12}	1.56 10^{17}	1.28 10^{15}	1.60 10^{15}
7.3	3.57 10^{16}	2.47 10^{14}	3.19 10^{14}	1.04 10^{17}	6.89 10^{14}	8.72 10^{14}

Table4.25. Parameters a, b and c of Equation (4.2).

The plot of the parameters in Figure (4.55) highlights their correlation with green density.

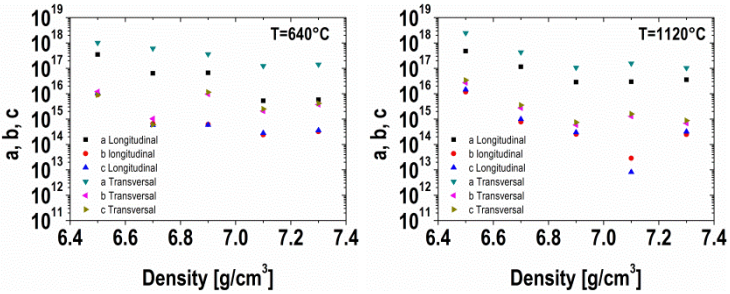

Figure 4.55. Parameters a, b and c of Equation (4.2) versus the density.

As in the previous section relevant to the study of the effect of sintering temperature, b and c for longitudinal and transversal direction are very similar. The effect of green density is ambiguous but, with some exceptions, it seems that all the parameters tend to decrease on increasing it.

3.4.2 Structural activity

The increase in green density is obtained by applying a greater pressure during cold compaction that causes a higher deformation of the powder particles.

Using the Equation (2.19) from the data of the effective diffusion coefficient the dislocation densities along the two directions and for the different densities was obtained. In Figure (4.56) the dislocation density calculated for the isothermal holding at 640°C is shown.

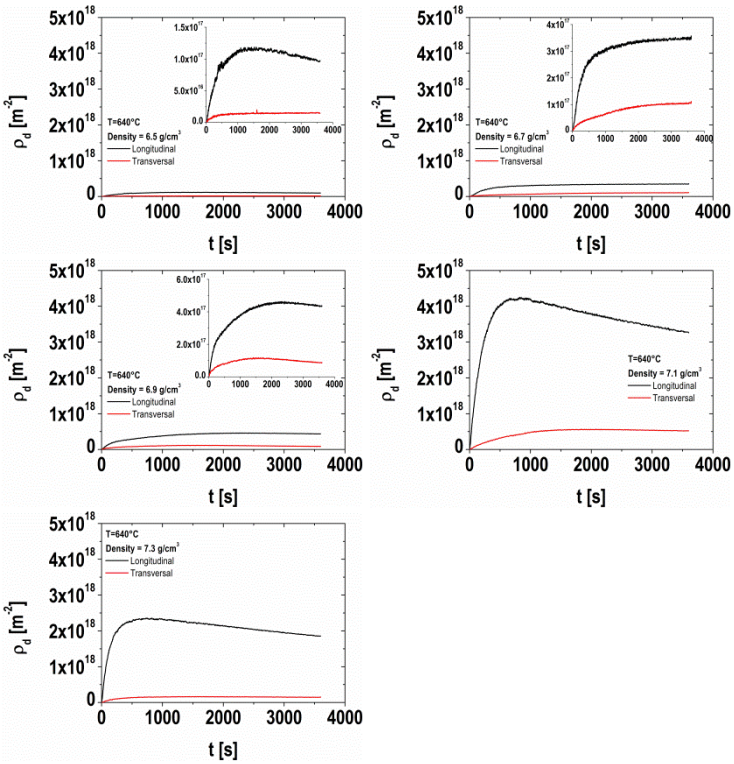

Figure 4.56. Dislocation density for the isothermal holding at 640°C.

The dislocation density is higher along the longitudinal direction and increases with green density (a part from the 7.3 g/cm^3 specimens). The effect of the isothermal holding time is a consequence of the evolution of D_{eff} during sintering. Dislocation density seems to increases until reaching a plateau, while for the last two green density after reaching a maximum, starts to decrease.
In Figure (4.57) the dislocation density for isothermal holding at 1120°C are shown:

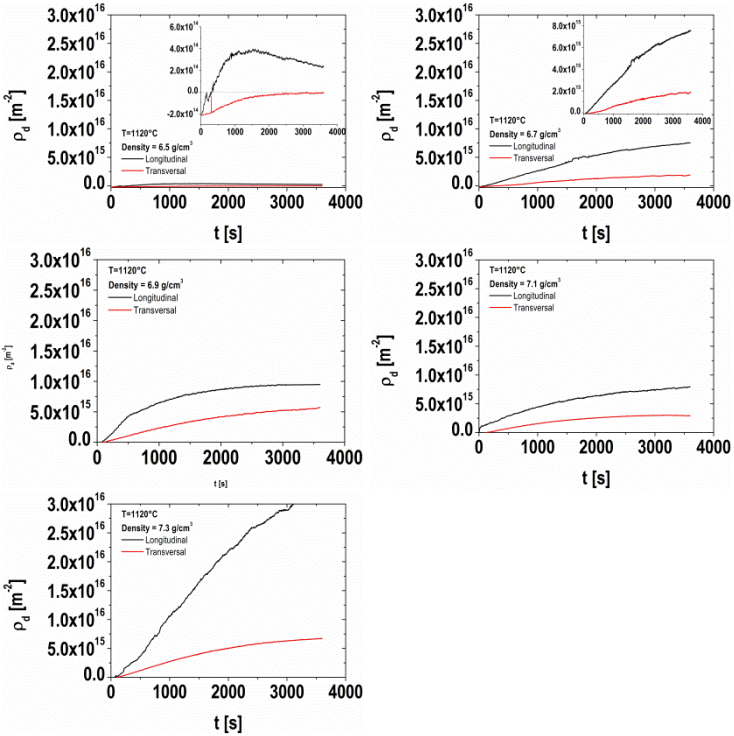

Figure 4.57. Dislocation density for the isothermal holding at 1120°C.

At this temperature the dislocations density is lower than at 640°C and increases monotonically with time, except for the lowest density where it shows the maximum for the curve of the longitudinal direction. Dislocation density results negative for the transversal direction at the lowest green density. Obviously this result does not have any physical meaning; it simply indicates that the equilibrium bulk diffusivity used for

the calculation of D_{eff} does not apply to the material investigated. Nevertheless, the trend with time and green density, as well as the difference between the directions are significant of a real behaviour.

The comparison between the two direction at the different isothermal holding temperature for the different green density are shown in Figure (4.58), using the dislocation density calculated from the maximum D_{eff} for each specimen and test.

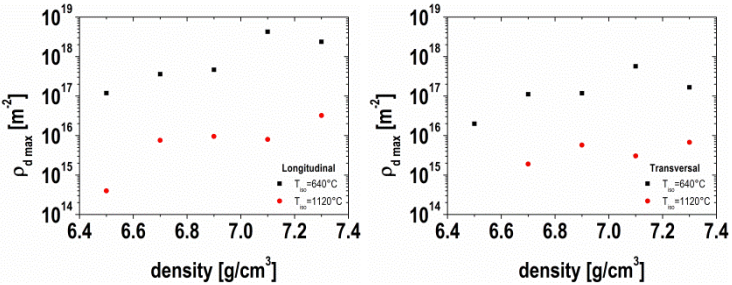

Figure 4.58. Maximum dislocation density for the isothermal holding at 1120°C and 640°C along the two direction versus the density.

The dislocation density increases with green density for both the temperatures and directions. The dislocations density at 1120°C is smaller than that at 640°C and is similar along the two directions. At 640°C there is one order of magnitude difference between the two directions.

3.4.3 Geometrical activity

SEM images (200 x) of the green compacts at 6.5, 6.9 and 7.3 g/cm^3 were collected in order to measure the extension of contacts between the particles in function of the density. In figure (4.59) some images of the green compacts are shown.

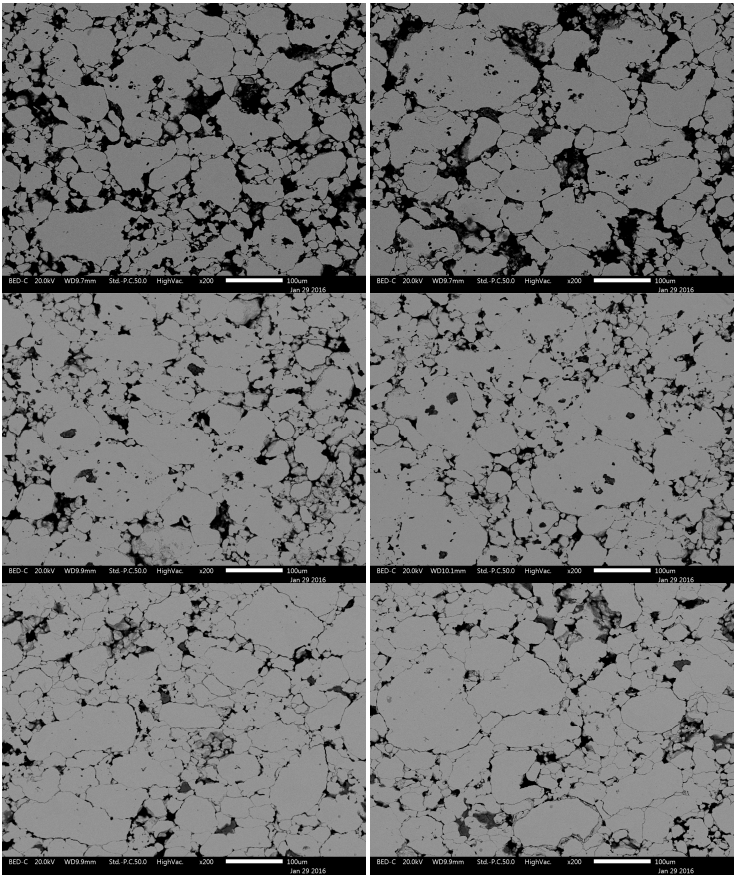

Figure 4.59. SEM images 200 x for the green components at 6.5 g/cm^3 (top), 6.9 g/cm^3(middle) and 7.3 g/cm^3 (bottom).

On increasing green density the powder particles are more increasingly deformed and packed. For the lower density the small particles are located in the porosity with large relative distance, while increasing the green density these appear more compacted and deformed.

In Figure (4.60) the distribution of the length of the contact orthogonal (x) and parallel (y) to the direction of compaction is shown: the total distribution on the left, the distribution around the median values on the right. The median values are listed in Table (5.26).

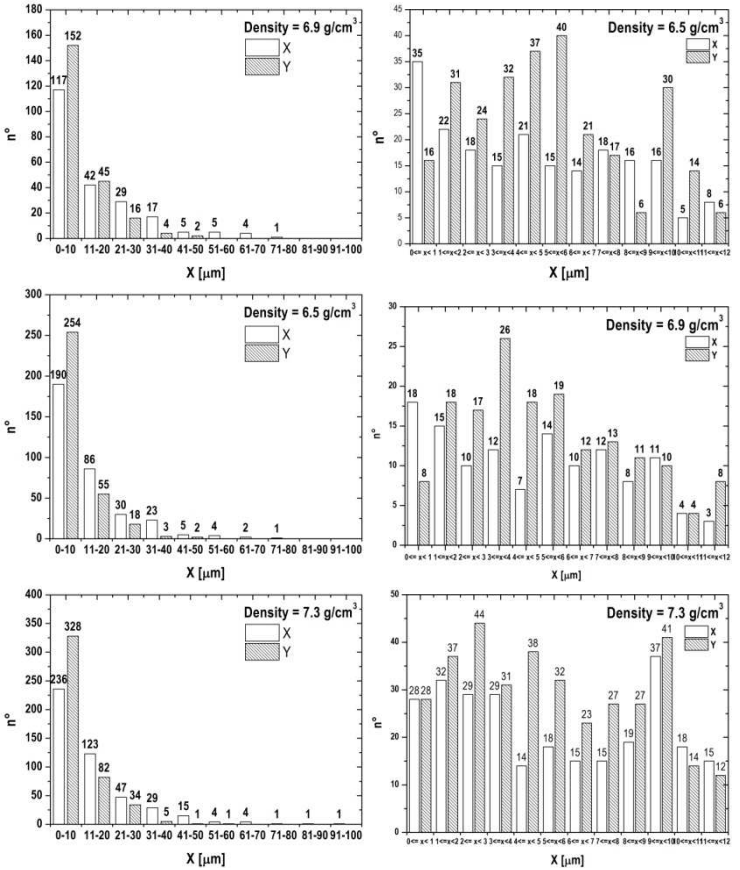

Figure 4.60. Distribution of length for the contacts orthogonal (x) and parallel (y) to the compaction direction.

Density [g/cm^3]	X_L [µm]	X_T [µm]	$\overline{X_L}$ [µm]	$\overline{X_T}$ [µm]]	$\overline{X_L}\backslash\overline{X_T}$
6.5	8.61	5.52	13.09	8.39	1.56
6.9	9.70	6.18	14.74	9.40	1.57
7.3	10.56	6.50	16.05	9.88	1.62

Table 4.26. Median value for the distribution of contacts length (X_L and X_T), median modified using the corrective factors and ratio between the two median.

The contact length is greater for the contacts perpendicular than for those parallel to the compaction direction; they increase with green density, but their ratio does not change remaining around 1.6. The geometrical activity does not have an influence of the effect of green density on anisotropy of shrinkage.

3.5 References

[1] E.A. Brandes, G.B. Brook, C.J. Smithells, Smithells metals reference book, Butterworth-Heinemann, 1998.

[2] A.S. Podder, I. Lonardelli, A. Molinari, H.K.D.H. Bhadeshia, Thermal stability of retained austenite in bainitic steel: an in situ study, Proc R Soc A. 467 (2011) 3141–3156. doi:10.1098/rspa.2011.0212.

[3] Y. Shima, Y. Ishikawa, H. Nitta, Y. Yamazaki, K. Mimura, M. Isshiki, et al., Self-Diffusion along Dislocations in Ultra High Purity Iron, Mater. Trans. 43 (2002) 173–177. doi:10.2320/matertrans.43.173.

[4] R.M. German, Sintering Theory and Practice, Wiley, 1996.

[5] A. Molinari, E. Torresani, C. Menapace, M. Larsson, The Anisotropy of Dimensional Change on Sintering of Iron, J. Am. Ceram. Soc. 98 (2015) 3431–3437.

[6] E. Friedrich, W. Schatt, Sintering of One-Component Model Systems: Nucleation and Movement of Dislocations in Necks, Powder Metall. 23 (1980) 193–197. doi:10.1179/pom.1980.23.4.193.

[7] E. Friedrich, W. Schatt, High Temperature Plasticity on Solid Phase Sintering, Sci Sinter. 15 (1983) 63–71.

[8] W. Schatt, E. Friedrich, Dislocation-Activated Sintering Processes, in: G.C. Kuczynski, D.P. Uskoković, H.P. III, M.M. Ristić (Eds.), Sintering'85, Springer US, 1987: pp. 133–141.

[9] A. Molinari, E. Bisoffi, C. Menapace, J. Torralba, Shrinkage kinetics during early stage sintering of cold isostatically compacted iron powder, Powder Metall. 57 (2014) 61–69. doi:10.1179/1743290113Y.0000000068.

[10] C.R. Brundle, C.A. Evans, S. Wilson, Encyclopedia of Materials Characterization: Surfaces, Interfaces, Thin Films, Gulf Professional Publishing, 1992.

[11] E.A. Olevsky, B. Kushnarev, A. Maximenko, V. Tikare, M. Braginsky, Modelling of anisotropic sintering in crystalline ceramics, Philos. Mag. 85 (2005) 2123–2146. doi:10.1080/14786430412331331989.

[12] D.L. Johnson, New Method of Obtaining Volume, Grain-Boundary, and Surface Diffusion Coefficients from Sintering Data, J. Appl. Phys. 40 (1969) 192–200.

[13] G. Stechauner, E. Kozeschnik, Assessment of substitutional self-diffusion along short-circuit paths in Al, Fe and Ni, Calphad. 47 (2014) 92–99. doi:10.1016/j.calphad.2014.06.008.

Chapter V

Conclusion

The anisotropy of the sintering shrinkage of uniaxially cold compacted iron powders was investigated in the present PhD thesis through an experimental approach based on the measurements of dimensional changes by dilatometry and the structural and geometrical characterization of the green specimens. The considerable influence of cold compaction on the dimensional changes during sintering and their anisotropy has been highlighted.

In the first part, the sintering shrinkage kinetic in the temperature range 640°C-1120°C was widely investigated using samples obtained from Charpy impact bars uniaxially cold compacted to 6.9 g/cm^3 of density. This part of the research has highlighted as the anisotropy in the dimensional changes is mostly developed at temperatures below the austenitic transformation, and in particular below the Curie temperature.

The main cause of anisotropy of shrinkage is the structural activity resulting from plastic deformation occurring during cold compaction. The inhomogeneous deformation of the powder particles (higher in the interparticle contacts perpendicular to the compaction direction than in those parallel to it) can explain the anisotropy of shrinkage. At temperatures below the austenitic transformation the dislocations introduced by the cold compaction represent a high diffusivity path for atoms flowing towards the neck surface, according to the dislocation pipe diffusion mechanism, that enhances the bulk diffusivity. The effective diffusion coefficient resulting from the combination of bulk and pipe diffusion shows an increase with the isothermal holding time resulting from the sum of the pre-existing dislocations and those generated near the growing necks according to the self-activation theory of sintering. Furthermore for temperatures approaching T_C ($\sim$770°C) an enhancement of shrinkage kinetic is observed due to the great influence of the change of magnetic properties on dislocation pipe diffusivity.

In austenitic field the anisotropy of dimensional changes is very small. This is imputed to the effects of the recrystallization occurring during the phase transformation that eliminates most of the dislocations introduced by cold compaction.

An equation correlating the effective diffusion coefficient to time and temperature was proposed, where the structural (dislocation density) and geometrical (extension of the interparticle contact areas) contribution are not explicitly shown. Despite of its empirical meaning, such an equation may be used to predict the isothermal shrinkage.

The dislocation density along the different directions was measured through three different methods; different values were obtained, that is probably due to specific limits of these experimental methods but even to the objective difficulty of the measure. Nevertheless all the methods highlight the anisotropy of the dislocation density. Moreover, in ferromagnetic field the dislocation density is higher than in the other temperature ranges and tend to increase approaching T_C, while in austenitic field the dislocation density is lower. These results support the interpretation of the causes of anisotropy of shrinkage.

A micromechanical model was adapted in order to describe the kinetics of shrinkage taking in to account the different dislocation density along the different directions. The model is based on the geometry of the powder particles and of porosity. An *extensive* work through image analysis was set up in order to measure the different geometrical parameters of particles and pores, highlighting the anisotropy of the contact lengths between the particles (corresponding to the internal neck radius) and the coordination number. These parameters represent the geometrical activity of the green material that, being anisotropic, may be cause of the slight anisotropic dimensional changes measured in austenitic field. Dislocation density calculated from the micromechanical model agrees quite well to those measured experimentally.

In the second part, the effect of green density on anisotropy of shrinkage was investigated, since the increase in green density is obtained by increasing compaction pressure, i.e. the plastic deformation of the particles and, in turn, the dislocation density in the contact regions. Five different densities were considered: 6.5, 6.7, 6.9, 7.1 and 7.3 g/cm^3. Dilatometric tests were carried out at 640°C and 1120°C, respectively the temperature at which shrinkage starts to be appreciable and the sintering temperature used in the industrial production. The results show clearly how increasing green density isothermal shrinkage increases, indicating that the structural activity prevails of the thermodynamic driving force related to the specific surface area. The anisotropy of dimensional changes increases, too. Again, anisotropy of shrinkage is much more pronounced in alpha field, and in particular below Tc, while it is rather small in austenite field. The anisotropy of geometrical activity, calculated as the ratio of extension of the interparticle contact areas along the longitudinal and the transversal directions, does not contribute to the effect of green density on anisotropy, since the ratio does not change with green density.

The work carried out in the present PhD thesis strengthens the interpretation of the role of the structural defectiveness introduced by prior cold compaction on shrinkage and its anisotropy. There are a few open points that should be investigated further.

First, dislocation density was measured on sintered specimens, due to criticism related to the preparation of the specimens that make the measure on the green parts very difficult. An experimental method to measure, either directly or indirectly, dislocation density in green parts should be individuated and applied.

Second, the equation describing the temperature and time dependence of the effective diffusion coefficient and of the dislocation density proposed here does not have a physical meaning. A more realistic model was proposed, based on the kinetics of recrystallization and of the increase in dislocation density claimed by the self-activation theory, with unsatisfactory results. The definition of such a model needs for further work.

The last point deals with the effect on shrinkage of the starting dimension of the contact area. In the classical theory of sintering, particles are assumed in a point contact, differently from what happens in the green parts. Such a details of the microstructure of the green materials was investigated here. The effect on shrinkage kinetic is called geometrical activity. The next step is the proposal of a new shrinkage kinetic equation, accounting for the real extension of the contact area.

Chapter VI

Scientific production

A. Molinari, E. Torresani, C. Menapace, M. Larsson (2015)
"The Anisotropy of Dimensional Change on Sintering of Iron"
Journal of the American Ceramic Society, 98 [11] (2015) 3431–3437, DOI: 10.1111/jace.13852

E. Torresani, I. Cristofolini, A. Molinari (2015)
"Study of the anisotropic microstructure of the uniaxially cold compacted green parts"
Advances in Powder Metallurgy and Particulate Materials (2015) 9-18

A. Molinari, E. Torresani (2015)
"**Preliminary study to determine the sintering stress from microstructural analysis of green parts"**
Powder Metall. 58 [5] (2015) 323–327.

A. Molinari, E. Torresani (2014)
"Preliminary study to determine the sintering stress from microstructural analysis of green parts"
Proceedings EURO PM2014 Congress & Exhibition, Salzburg 21-24 September 2014, ed. EPMA, Shrewsbury (UK), CD room

E. Torresani, G.Ischia, A. Molinari (2014)
"Study of deformation of powders due the cold compaction"
Proceedings EURO PM2014 Congress & Exhibition, Salzburg 21-24 September 2014, ed. EPMA, Shrewsbury (UK), CD room

A. Molinari, E. Torresani, C. Menapace, I. Cristofolini, M. Larsson (2013)
"A study of sintering shrinkage kinetics of cold compacted ferrous green parts "
Advances in Powder Metallurgy and Particulate Materials 5 (2013) 25-32

A. Molinari, C. Menapace, E. Torresani, I. Cristofolini, M.Larsson (2013)
"Working hypothesis for origin of anisotropic sintering shrinkage caused by prior uniaxial cold compaction"
Powder Metallurgy, 56 [3] (2013) 189-195

C.Menapace, M.Larsson, E.Torresani, I.Cristofolini, A.Molinari (2012) ***"Study of Anisotropy during Sintering of Ferrous Alloys***" Proceedings PM2012, 2012 Powder Metallurgy World Congress & Exhibition, Yokohama (Japan) 14-18 October 2012, CD-room, Japan Society of Powder and Powder Metallurgy, ISBN: 978-4-9900214-9-8

Acknowledgments

This thesis represents only the last step of a three years path that has required diligence and perseverance. Luckily has not been a lonely journey, but many people have accompanied me, so I would like to thank all personally.

First and foremost, I wish to thank my advisor Professor Alberto Molinari who has followed this project with passion and always has put his confidence in my work. I would like also to thank him for showing me always his availability to discuss and give me advices and I hope I have never disappointed him.

I would like to thank the group of Metallurgy and Microstructure Laboratory to which it must be added the super secretary of PhD school, a special group of people that I consider more than simple colleagues: Cinzia, Melania, Anna, Giulia, Lorena, Sara, Simone, Nicolò, Marco and Ibrahim. You were always available to help me in my troubles inside and outside of work.

I would also to thank the entire group of the Powder Technology Laboratory: Professor Eugene A. Olevsky, Diletta, Xialu, Geuntak, Jeff and Paramjot. I spend a brief but intense period to work with you, but it made me feel as part of your group and some parts of this work were possible only thanks to you.

To all my friends: I can count on you in any evenience and even when I am far away I feel near you.

For last but not least I wish to express my profound thanks to those who always helped and encourage me: my family, and I need to thank them in Italian now:
Alla mia famiglia e specialmente ai miei genitori Maria e Rosario che mi avete sempre aiutato, non solo durante questi tre anni. Mi avete incoraggiata e supportata in tutte le mie scelte, e anche se alle volte vi posso aver fatto arrabbiare o magari deluso, spero siate fieri di me come io lo sono di voi.
Inoltre voglio ringraziare mio fratello Walter che è sempre corso in mio aiuto quanto ne avevo bisogno e ti ringrazio anche per i nostri confronti/scontri di idee che mi hanno aiutata a pensare attraverso diversi punti di vista.